Quantitative and comprehensive analysis of *Ciona* notochord organogenesis

by

Konner Michael Winkley

B.S., Kansas State University, 2016

AN ABSTRACT OF A DISSERTATION

submitted in partial fulfillment of the requirements for the degree

DOCTOR OF PHILOSOPHY

Division of Biology
College of Arts and Sciences

KANSAS STATE UNIVERSITY
Manhattan, Kansas

2020

Abstract

Technical advances in imaging and genomics are making developmental biology increasingly quantitative. The invertebrate chordate *Ciona* has small embryos, a compact genome, and a simple, yet stereotypically chordate body plan, making it well suited to quantitative, systems-level studies of organogenesis. This is particularly true for the *Ciona* notochord, which is comprised of only 40 cells that form a simple tapered rod. The unifying theme of this dissertation is to comprehensively and quantitatively analyze the development of the *Ciona* notochord in terms of both the cell behaviors driving morphogenesis and the gene regulatory networks controlling notochord cell fate.

Ciona embryos develop rapidly, and, since they are poikilotherms, at a rate proportional to the temperature at which they are incubated. I required precise embryonic staging of the temporally dynamic transcriptional and morphogenetic processes I was studying in order to make accurate conclusions. To facilitate this, we developed a simple yet powerful open source device, the Temperature Adjusted Developmental Timer, which allows researchers to stage embryos accurately with respect to temperature in real time and requires only the estimation of two simple species-specific parameters.

Using quantitative confocal microscopy and computational image analysis, I quantified how a series of subtle but iterative asymmetric divisions give rise to the observed cell volume differences along the AP axis of the post-mitotic notochord which contributes to its tapered shape. I partitioned the contributions of three cellular mechanisms to the observed asymmetric divisions using a modeling framework and uncovered a previously unappreciated role of mother-cell shape in this process.

To characterize the earliest gene-regulatory network (GRN) of the notochord, I collected a single-cell RNA-sequencing (scRNAseq) timecourse of early *Ciona* development during the stages in which notochord and many other distinct cell fates are established. This was performed both with and without a pharmacological inhibitor of a MAPK-dependent signal involved in many early cell fate decisions including notochord. The scRNAseq data revealed that the earliest signatures of the *Ciona* notochord GRN involve transcriptional activation by Ets and Zic family transcription factors in parallel to, and not downstream of the notochord specific transcription factor Brachyury.

These diverse studies of notochord organogenesis are linked in being deeply quantitative and based on assessing cellular properties and behaviors with single-cell resolution on a scale ranging from an entire organ primordium to an entire embryo. Both the asymmetric division study and the scRNAseq study have broad implications beyond the *Ciona* notochord and contribute to a modern understanding of the processes of development at the single-cell level.

Quantitative and comprehensive analysis of *Ciona* notochord organogenesis

by

Konner Michael Winkley

B.S., Kansas State University, 2016

A DISSERTATION

submitted in partial fulfillment of the requirements for the degree

DOCTOR OF PHILOSOPHY

Division of Biology
College of Arts and Sciences

KANSAS STATE UNIVERSITY
Manhattan, Kansas

2020

Approved by:

Major Professor
Dr. Michael Veeman

Copyright

Abstract

Technical advances in imaging and genomics are making developmental biology increasingly quantitative. The invertebrate chordate *Ciona* has small embryos, a compact genome, and a simple, yet stereotypically chordate body plan, making it well suited to quantitative, systems-level studies of organogenesis. This is particularly true for the *Ciona* notochord, which is comprised of only 40 cells that form a simple tapered rod. The unifying theme of this dissertation is to comprehensively and quantitatively analyze the development of the *Ciona* notochord in terms of both the cell behaviors driving morphogenesis and the gene regulatory networks controlling notochord cell fate.

Ciona embryos develop rapidly, and, since they are poikilotherms, at a rate proportional to the temperature at which they are incubated. I required precise embryonic staging of the temporally dynamic transcriptional and morphogenetic processes I was studying in order to make accurate conclusions. To facilitate this, we developed a simple yet powerful open source device, the Temperature Adjusted Developmental Timer, which allows researchers to stage embryos accurately with respect to temperature in real time and requires only the estimation of two simple species-specific parameters.

Using quantitative confocal microscopy and computational image analysis, I quantified how a series of subtle but iterative asymmetric divisions give rise to the observed cell volume differences along the AP axis of the post-mitotic notochord which contributes to its tapered shape. I partitioned the contributions of three cellular mechanisms to the observed asymmetric divisions using a modeling framework and uncovered a previously unappreciated role of mother-cell shape in this process.

To characterize the earliest gene-regulatory network (GRN) of the notochord, I collected a single-cell RNA-sequencing (scRNAseq) timecourse of early *Ciona* development during the stages in which notochord and many other distinct cell fates are established. This was performed both with and without a pharmacological inhibitor of a MAPK-dependent signal involved in many early cell fate decisions including notochord. The scRNAseq data revealed that the earliest signatures of the *Ciona* notochord GRN involve transcriptional activation by Ets and Zic family transcription factors in parallel to, and not downstream of the notochord specific transcription factor Brachyury.

These diverse studies of notochord organogenesis are linked in being deeply quantitative and based on assessing cellular properties and behaviors with single-cell resolution on a scale ranging from an entire organ primordium to an entire embryo. Both the asymmetric division study and the scRNAseq study have broad implications beyond the *Ciona* notochord and contribute to a modern understanding of the processes of development at the single-cell level.

Table of Contents

List of Figures

List of Tables

Acknowledgements

There are several people who need to be recognized for their contributions to this dissertation. To my advisor, Michal Veeman, I am thankful for the opportunity you gave me to enter the field of developmental biology. Thank you for seeing my seeing my competence with quantitative analyses before I even knew that it was something I was capable of, or interested in, myself. You have profoundly shaped the way that I think about and do science. To my supervisory committee; Erika Geisbrecht, Jocelyn McDonald, and Mike Herman, thank you for your guidance and input through out my graduate studies and for your suggestions as I explored my future career path. To those I worked with daily in lab for the past four years; Wendy Reeves, and Matt Harder, your presence in lab and willingness to help have made this experience a joy. Lastly to my family and friends, thank you for your encouragement and support every step of the way during this journey.

The research in this dissertation was funded by the National Science Foundation grant IOS1456555 “Linking Cell Shape and Asymmetric Division in *Ciona* Notochord Tapering” awarded to Michael Veeman.

Dedication

To my wife, Emma. Thank you for all your support and encouragement during this process, it wouldn’t have been possible without you.

Preface

The following contents of this dissertation have been published as follows:

Chapter 2: "Tunicate gastrulation" by Konner M. Winkley, Matthew J. Kourakis, Anthony W. DeTomaso, Michael T. Veeman, and William C. Smith. Published in Current topics in Developmental Biology, Volume 136 (2020).

Chapter 3: "A temperature-adjusted developmental timer for precise embryonic staging" by Konner M. Winkley and Michael T. Veeman. Published in Biology Open Volume 7, Issue 6 (2018)

Chapter 4: "Iterative and Complex Asymmetric Divisions Control Cell Volume Differences in *Ciona* Notochord Tapering" by Konner Winkley, Spencer Ward, Wendy Reeves, and Michael Veeman. Published in Current Biology Volume 29, Issue 20 (2019).

Chapter 1 - Introduction

Dissertation overview

Despite the vast diversity in adult body plans, the starting point for most species of sexually reproducing animals is essentially a totipotent, single-celled zygote. To acquire its distinctive multicellular adult form, this zygote must undergo many rounds of cell division. As the number of cells increases, these cells must undergo finely choreographed patterning events that make them different from one another in terms of both their physical attributes and their transcriptional states.

Waddington first laid out a conceptual framework with his "developmental landscape" metaphor to think about the refinement of cell types during development through recurrent branching decisions that establish alternate trajectories of gene expression (Waddington, 1957). There have been countless developmental biology studies dissecting the mechanisms by which cells become different from one another during these trajectory branching events. They have demonstrated how the presence and activity of specific transcription factors are responsible for the assumption of many cell fates (Davis et al., 1987; Gubelmann et al., 2014; Hemesath et al., 1994), how the subcellular localization of signaling components can pattern cells and tissues across multiple axes (Butler & Wallingford, 2017; Campanale et al., 2017; Goodrich & Strutt, 2011), and how cells are able to sense their physical environment to integrate their response across both genetic and morphogenetic pathways of differentiation (Crews, 1996; Piotrowska & Zernicka-Goetz, 2001).

Even though these seminal studies established the framework we used to think about the process of cellular differentiation, they were often limited by the technology available to researchers at the time. The past two decades have seen dramatic technological advances,

particularly in quantitative imaging and genomics. These advances are allowing researchers to address fundamental developmental biology questions that were previously out of reach due to technological limitations. They also are making studies in developmental biology increasingly quantitative. Scientists can now image entire embryos with remarkable spatial and temporal resolution (Huisken et al., 2004), quantify the subcellular localization of single protein molecules in live cells (Betzig et al., 2006; Hess et al., 2006; Rust et al., 2006; Wombacher et al., 2010), and comprehensively describe the transcriptome of all the individual cells in an embryo at the same time (Farrell et al., 2018; Macosko et al., 2015; Wagner et al., 2018).

I set out to take advantage of new imaging and genomics technologies to quantitatively understand how cells become different from one another, both physically and transcriptionally, during development in a comprehensive, systems-level framework. To do so, I used the invertebrate chordate *Ciona*, which is an emerging model for studies in quantitative developmental biology. *Ciona* embryos are stereotypically chordate, containing a notochord, a hollow dorsal neural tube, and a muscular tail. However, they lack much of the anatomical complexity of vertebrate embryos that can complicate studies of morphogenesis. Their embryos are also small enough to be imaged in entirety, in a single field of view, while still maintaining subcellular detail (M. Veeman & Reeves, 2015). Additionally, *Ciona's* compact, approximately 125 MB, genome makes functional genomic studies more feasible (Satou et al., 2019).

These advantages of *Ciona* for quantitative studies of developmental biology are particularly relevant when considering its notochord. The notochord is a long rod of axial mesoderm with both structural and signaling roles that is a defining feature of the phylum *Chordata*. The *Ciona* notochord is comprised of only 40 cells and forms a simple tapered rod at tailbud stages. Despite this morphological simplicity, it still undergoes dramatic shape changes and large-scale

morphogenetic events such as mediolateral intercalation. This allows transcriptomic (Harder et al., 2018; W. Reeves et al., 2014; W. M. Reeves et al., 2017) and morphological (M. T. Veeman & Smith, 2013) studies of complex processes to be carried out with single-cell resolution on the scale of an entire organ.

With all this in mind, I used the notochord of *Ciona* as a model to quantitatively and comprehensively analyze both specific cell behaviors driving morphogenesis and the gene regulatory networks controlling notochord cell fate. A more detailed discussion of early *Ciona* embryonic development will be presented in Chapter 2.

Dissertation projects

Temperature

The transcriptomic and morphogenetic processes I study are temporally dynamic and require precise embryonic staging. *Ciona* embryos develop rapidly, progressing from fertilized eggs to hatching larva in only about 18 hours at 18˚ C (Hotta et al., 2007). Because of this, the time window for an event of interest can be quite small. Catching distinct developmental landmarks in *Ciona* is also complicated by the fact that the rate of development changes in response to even small changes in the temperature at which embryos are incubated (Hotta et al., 2007). In Chapter 3, I will describe a simple yet powerful open source device we developed, the Temperature Adjusted Developmental Timer, which takes into account the temperature at which embryos are incubated and provides a temperature adjusted embryonic staging metric in real-time. I also demonstrate the biological validity of this device and its ability to reproducibly stage a single cell cycle of a given set of blastomeres across a range of temperatures. This device will be used throughout the rest of my dissertation studies to allow me to make comparisons across experimental replicates about nearly identical time frames

Asymmetric division

The *Ciona* notochord forms a tapered rod at tailbud stages, which in part is shaped by cell volume differences along the anterior-posterior axis of the notochord where cells near the tips are smaller in volume than cells nearer the middle (M. T. Veeman & Smith, 2013). We had two alternative, but not necessarily mutually exclusive, hypotheses of how these cell volume differences arise. One is that they arise early in development from sibling cell volume asymmetries during notochord cell division. The other is that notochord cells shrink and swell in a locally patterned manner to give rise to the cell volume differences. In Chapter 4, I use a large

sample size to test hypotheses by quantifying sibling cell volume asymmetries for all notochord blastomeres across all the relevant rounds of division using quantitative confocal microscopy and computational image analysis. I found that a series of subtle, but iterative asymmetric divisions give rise to the observed cell volume differences along the AP axis of the post-mitotic notochord. I will also show that these divisions are driven by complex contributions of three distinct cellular mechanisms, including a previously unappreciated role of mother-cell shape. This study produced a quantitative understanding of how cells become physically different from one another during development and how these changes contribute to the emergence of shape at the level of an entire chordate organ.

Single-cell RNAseq

The founder cells of the primary and secondary notochord lineages in *Ciona* become fate restricted at the 64-cell, and 110-cell stage respectively (Nishida, 1987; Nishida & Satoh, 1985). Decades of work have elucidated key signals from surrounding tissues that are necessary for inducing notochord (Hudson & Yasuo, 2006; Picco et al., 2007; Yasuo & Hudson, 2007). However, we lack an understanding of what gene products make notochord cells transcriptionally different from their sibling cells immediately after the fate bifurcation event. In Chapter 5, I will explain how I characterized the earliest gene-regulatory network (GRN) of the notochord, by collecting a single-cell RNA-sequencing (scRNAseq) timecourse of early *Ciona* development during the stages that notochord and many other distinct cell fates are established. This set of scRNAseq experiments was performed both with and without a pharmacological inhibitor of a MAPK-dependent signal involved in many early cell fate decisions including notochord. Using this perturbation, I will demonstrate how I inferred the transcriptional effects of Fibroblast Growth Factor (FGF) and Mitogen-activated Protein Kinase (MAPK) signaling in

numerous cell fate bifurcation events. I also discovered that some FGF dependent cell types do not become transfated to their sibling cell type, but instead adopt novel patterns of gene expression not observed in control embryos. Finally, I will show that the earliest signatures of the *Ciona* notochord GRN involve transcriptional activation by Ets and Zic family transcription factors in parallel to, and not downstream of the notochord specific transcription factor Brachyury. An underlying trend in our analysis during this study is that the transcriptional differences between sibling cell types immediately after fate bifurcation events are not limited to only a few "master regulatory" transcription factors, but rather entire suites of transcription factors as well as putative effector genes are differentially expressed. From this, we hypothesize that the "hourglass" shaped model used to describe cell-fate GRNs may be wider than previously understood.

References – Chapter 1

Betzig, E., Patterson, G. H., Sougrat, R., Lindwasser, O. W., Olenych, S., Bonifacino, J. S., Davidson, M. W., Lippincott-Schwartz, J., & Hess, H. F. (2006). Imaging intracellular fluorescent proteins at nanometer resolution. *Science*, *313*(5793), 1642–1645. https://doi.org/10.1126/science.1127344

Butler, M. T., & Wallingford, J. B. (2017). Planar cell polarity in development and disease. *Nature Reviews Molecular Cell Biology*, *18*(6), 375–388. https://doi.org/10.1038/nrm.2017.11

Campanale, J. P., Sun, T. Y., & Montell, D. J. (2017). Development and dynamics of cell polarity at a glance. *Journal of Cell Science*, *130*(7), 1201–1207. https://doi.org/10.1242/jcs.188599

Crews, D. (1996). Temperature-Dependent Sex Determination: The Interplay of Steroid Hormones and Temperature. *Zoological Science*, *13*(1), 1–13. https://doi.org/10.2108/zsj.13.1

Davis, R. L., Weintraub, H., & Lassar, A. B. (1987). Expression of a single transfected cDNA converts fibroblasts to myoblasts. *Cell*, *51*(6), 987–1000. https://doi.org/10.1016/0092-8674(87)90585-X

Farrell, J. A., Wang, Y., Riesenfeld, S. J., Shekhar, K., Regev, A., & Schier, A. F. (2018). Single-cell reconstruction of developmental trajectories during zebrafish embryogenesis. *Science*, *360*(6392). https://doi.org/10.1126/science.aar3131

Goodrich, L. V., & Strutt, D. (2011). Principles of planar polarity in animal development. *Development*, *138*(10), 1877–1892. https://doi.org/10.1242/dev.054080

Gubelmann, C., Schwalie, P. C., Raghav, S. K., Röder, E., Delessa, T., Kiehlmann, E., Waszak, S. M., Corsinotti, A., Udin, G., Holcombe, W., Rudofsky, G., Trono, D., Wolfrum, C., & Deplancke, B. (2014). Identification of the transcription factor ZEB1 as a central component of the adipogenic gene regulatory network. *ELife*, *3*(August2014), 1–30. https://doi.org/10.7554/eLife.03346

Harder, M., Reeves, W., Byers, C., Santiago, M., & Veeman, M. (2018). Multiple inputs into a posterior-specific regulatory network in the Ciona notochord. *Developmental Biology*, *448*(2), 136–146. https://doi.org/10.1016/j.ydbio.2018.09.021

Hemesath, T. J., Steingrímsson, E., McGill, G., Hansen, M. J., Vaught, J., Hodgkinson, C. A., Arnheiter, H., Copeland, N. G., Jenkins, N. A., & Fisher, D. E. (1994). microphthalmia, A critical factor in melanocyte development, defines a discrete transcription factor family. *Genes and Development*, *8*(22), 2770–2780. https://doi.org/10.1101/gad.8.22.2770

Hess, S. T., Girirajan, T. P. K., & Mason, M. D. (2006). Ultra-high resolution imaging by fluorescence photoactivation localization microscopy. *Biophysical Journal*, *91*(11), 4258–

4272. https://doi.org/10.1529/biophysj.106.091116

Hotta, K., Mitsuhara, K., Takahashi, H., Inaba, K., Oka, K., Gojobori, T., & Ikeo, K. (2007). A web-based interactive developmental table for the ascidian Ciona intestinalis, including 3D real-image embryo reconstructions: I. From fertilized egg to hatching larva. *Developmental Dynamics : An Official Publication of the American Association of Anatomists*, *236*(7), 1790–1805. https://doi.org/10.1002/dvdy.21188

Hudson, C., & Yasuo, H. (2006). A signalling relay involving Nodal and Delta ligands acts during secondary notochord induction in Ciona embryos. *Development (Cambridge, England)*, *133*(15), 2855–2864. https://doi.org/10.1242/dev.02466

Huisken, J., Swoger, J., Del Bene, F., Wittbrodt, J., & Stelzer, E. H. K. (2004). Optical sectioning deep inside live embryos by selective plane illumination microscopy. *Science*, *305*(5686), 1007–1009. https://doi.org/10.1126/science.1100035

Macosko, E. Z., Basu, A., Satija, R., Nemesh, J., Shekhar, K., Goldman, M., Tirosh, I., Bialas, A. R., Kamitaki, N., Martersteck, E. M., Trombetta, J. J., Weitz, D. A., Sanes, J. R., Shalek, A. K., Regev, A., & McCarroll, S. A. (2015). Highly Parallel Genome-wide Expression Profiling of Individual Cells Using Nanoliter Droplets. *Cell*, *161*(5), 1202–1214. https://doi.org/10.1016/j.cell.2015.05.002

Nishida, H. (1987). Cell lineage analysis in ascidian embryos by intracellular injection of a tracer enzyme. III. Up to the tissue restricted stage. *Developmental Biology*, *121*(2), 526–541. https://doi.org/10.1126/science.725606

Nishida, H., & Satoh, N. (1985). Cell lineage analysis in ascidian embryos by intracellular injection of a tracer enzyme. II. The 16- and 32-cell stages. *Developmental Biology*, *110*(2), 440–454. https://doi.org/10.1016/0012-1606(87)90188-6

Picco, V., Hudson, C., & Yasuo, H. (2007). Ephrin-Eph signalling drives the asymmetric division of notochord/neural precursors in Ciona embryos. *Development*, *134*(8), 1491–1497. https://doi.org/10.1242/dev.003939

Piotrowska, K., & Zernicka-Goetz, M. (2001). Role for sperm in spatial patterning of the early mouse embryo. *Nature*, *409*(6819), 517–521. https://doi.org/10.1038/35054069

Reeves, W. M., Wu, Y., Harder, M. J., & Veeman, M. T. (2017). Functional and evolutionary insights from the Ciona notochord transcriptome. *Development*, *144*(18), 3375–3387. https://doi.org/10.1242/dev.156174

Reeves, W., Thayer, R., & Veeman, M. (2014). Anterior-posterior regionalized gene expression in the Ciona notochord. *Developmental Dynamics*, *243*(4), 612–620. https://doi.org/10.1002/dvdy.24101

Rust, M. J., Bates, M., & Zhuang, X. (2006). Sub-diffraction-limit imaging by stochastic optical reconstruction microscopy (STORM). *Nature Methods*, *3*(10), 793–796. https://doi.org/10.1038/nmeth929

Satou, Y., Nakamura, R., Yu, D., Yoshida, R., Hamada, M., Fujie, M., Hisata, K., Takeda, H., & Satoh, N. (2019). A Nearly Complete Genome of Ciona intestinalis Type A (C. robusta) Reveals the Contribution of Inversion to Chromosomal Evolution in the Genus Ciona. *Genome Biology and Evolution*, *11*(11), 3144–3157. https://doi.org/10.1093/gbe/evz228

Veeman, M., & Reeves, W. (2015). Quantitative and in toto imaging in ascidians: Working toward an image-centric systems biology of chordate morphogenesis. *Genesis*, *53*(1), 143–159. https://doi.org/10.1002/dvg.22828

Veeman, M. T., & Smith, W. C. (2013). Whole-organ cell shape analysis reveals the developmental basis of ascidian notochord taper. *Developmental Biology*, *373*(2), 281–289. https://doi.org/10.1016/j.ydbio.2012.11.009

Waddington, C. H. (1957). The strategy of the genes; a discussion of some aspects of theoretical biology. In *London: Allen & Unwin*. Allen & Unwin.

Wagner, D. E., Weinreb, C., Collins, Z. M., Briggs, J. A., Megason, S. G., & Klein, A. M. (2018). Single-cell mapping of gene expression landscapes and lineage in the zebrafish embryo. *Science*, *360*(6392), 981–987. https://doi.org/10.1126/science.aar4362

Wombacher, R., Heidbreder, M., van de Linde, S., Sheetz, M. P., Heilemann, M., Cornish, V. W., & Sauer, M. (2010). Live-cell super-resolution imaging with trimethoprim conjugates. *Nature Methods*, *7*(9), 717–719. https://doi.org/10.1038/nmeth.1489

Yasuo, H., & Hudson, C. (2007). FGF8/17/18 functions together with FGF9/16/20 during formation of the notochord in Ciona embryos. *Developmental Biology*, *302*(1), 92–103. https://doi.org/10.1016/j.ydbio.2006.08.075

Chapter 2 - Tunicate gastrulation

Abstract

Tunicates are a diverse group of invertebrate marine chordates that includes the larvaceans, thaliaceans, and ascidians. Because of their unique evolutionary position as the sister group of the vertebrates, tunicates are invaluable as a comparative model and hold the promise of revealing both conserved and derived features of chordate gastrulation. Descriptive studies in a broad range of tunicates have revealed several important unifying traits that make them unique among the chordates, including invariant cell lineages through gastrula stages and an overall morphological simplicity. Gastrulation has only been studied in detail in ascidians such as Ciona and Phallusia, where it involves a simple cup-shaped gastrula driven primarily by endoderm invagination. This appears to differ significantly from vertebrate models, such as Xenopus, in which mesoderm convergent extension and epidermal epiboly are major contributors to involution. These differences may reflect the cellular simplicity of the ascidian embryo.

Introduction: Tunicates-Their place on the evolutionary tree and their contribution to our understanding of embryology

Tunicates were among the earliest experimental models for embryology. Embryologists were attracted to the ascidian embryo, with its regular cleavage program and small, simple embryonic body plan. Chabry performed blastomere separation experiments in early embryos of the ascidian *Ascidiella aspersa* that are regarded as foundational to the discipline of experimental embryology (Chabry, 1887; Fischer, 1992). He found that isolated blastomeres showed predetermined fates, dividing as if they were still in the intact embryo. Although not obvious in their diverse adult forms, tunicates embryos are unmistakably chordate with a notochord and dorsal hollow nerve cord. The close evolutionary relationship of ascidians to vertebrates was well appreciated by this time (Darwin, 1871; Haeckel, 1895; Kovalevskij, 1866). Conklin (Edwin Grant Conklin, 1905) built on Chabry's work and mapped the complete lineage of cells through and beyond gastrulation, with illustrations by embryonic stage and a nomenclature still in use. Conklin's work included descriptions of cleavage planes, cell-cell contacts, nuclear positions, distribution of cytoplasmic determinants, cell fates, polar body location, and spindle dynamics, as well as comparisons of gastrulation and other aspects of embryogenesis between ascidians and other animals. Satoh's SEM studies of *Halocynthia roretzi* confirmed and expanded on these early descriptions of ascidian development, bolstering inferences concerning the coordination of cell movements during gastrulation and neurulation and revealing additional surface features, such as the presence of filopodia from interior membranes over the blastocoel (Satoh, 1978).

Since that time, molecular approaches in *Halocynthia*, *Ciona* and *Phallusia* have revealed much about the mechanisms driving ascidian patterning and morphogenesis, but little is known

about tunicate gastrulation and other developmental processes outside these ascidian models. The tunicates are thought to have diverged from their last common ancestor with the vertebrates more than 500 million years ago, and are a large and diverse group. They are usually regarded as a chordate sub-phylum, but some authors have argued that they should be elevated to phylum status (Satoh, Rokhsar, & Nishikawa, 2014). The ascidians (class *Ascidiacea*) are sessile as adults and are the most speciose group of tunicates, represented by nearly 3000 separate types (WoRMS, 2019) across three orders, Phlebobranchia, Stolidobranchia and Aplousobranchia, each characterized by differences in gill-slit morphology. Many of these are solitary, but colonialism has evolved independently in multiple ascidian lineages (Brown & Swalla, 2012), with varying degrees of physiological integration. The thaliaceans (class *Thaliacea*), with about 80 known species, are pelagic as adults and move through the water column by pulsating muscular contractions, using incurrent and excurrent siphons at opposite ends of the body. Thaliaceans, including pyrosomes, salps and doliolids, can be seen singly, or as chains of asexually budding animals. They can show alternation of sexual and asexual generations, and can reproduce asexually at an explosive rate during plankton blooms (Holland, 2016). The larvaceans (class *Appendicularia*) are also pelagic and represented by about 70 species (WoRMS, 2019). Larvaceans are so-called because they never lose their tails and resemble larvae into adulthood. They live inside buoyant glycoprotein ‘houses’ that aid in filter feeding and are secreted by specialized epidermal organs.

Molecular phylogenies using concatenated sequence datasets reveal that tunicates, and not cephalochordates, are the sister taxon to the vertebrates (Figure 2.1) (Bourlat, Rota-Stabelli, Lanfear, & Telford, 2009; Delsuc, Brinkmann, Chourrout, & Philippe, 2006). Two recent phylogenies, largely congruent, go further to resolve relations among the tunicates (Delsuc et al.,

2018; Kocot, Tassia, Halanych, & Swalla, 2018) as summarized in Figure 2.1. Larvaceans are the basal lineage, pointing to a possible pelagic ancestor for the tunicates as a whole. The ascidian order Stolidobranchia is sister to a group that includes the Thaliacea plus an Aplousiobranchia/Phlebobranchia pairing (the phlebobranch ascidians may themselves be paraphyletic, however). The placement of thaliaceans *within* the Ascidiacea is contrary to most older classification schemes of the last century (see, e.g., (Brusca & Brusca, 1990)) but is well-supported and suggests this free-swimming group evolved from a benthic ascidian ancestor, underscoring the potential for extensive morphological innovation in these lesser-studied tunicates (Kocot et al., 2018).

Events Leading Up to Gastrulation

Cleavage patterns

Only minor differences in embryonic cleavage patterns have been described between different ascidian species. *Ciona* cell lineages were first described in detail by Conklin (Edwin Grant Conklin, 1905), who also took advantage of the highly pigmented *Styela* egg to identify a cytoplasmic component he called the 'myoplasm' that segregates with muscle fate (Edwin G Conklin, 1905b). This was arguably the first cytoplasmic determinant of cell fate to be identified, and provided the foundation for the mosaic theory of development (Edwin G Conklin, 1905a). Conklin's cell lineages were refined and extended by Nishida who performed blastomere labeling experiments in *Halocynthia*, which has a larger embryo better suited to single-cell microinjection than *Ciona* (Hiroki Nishida, 1987; Hiroki Nishida & Satoh, 1983, 1985). Most cells are restricted to a single tissue fate by the start of gastrulation at the 112-cell stage (Hiroki Nishida, 1987), though there is extensive subsequent refinement of cell identity in the neural lineages in particular (Hudson, Lotito, & Yasuo, 2007; Racioppi et al., 2014; Stolfi, Wagner, Taliaferro, Chou, & Levine, 2011). The fate map has not been deciphered with single cell resolution all the way to the hatched larval stage, but several specific lineages have been traced well past gastrulation (Carlson, Reeves, & Veeman, 2015; Nicol & Meinertzhagen, 1988; Stolfi & Levine, 2011; Stolfi, Ryan, Meinertzhagen, & Christiaen, 2015; Tokuoka, Imai, Satou, & Satoh, 2004; Wang et al., 2019). Many markers of tissue differentiation are expressed normally even in embryos that have been cleavage arrested prior to gastrulation (T Nishikata, Mita-Miyazawa, Deno, & Satoh, 1987; Okado & Takahashi, 1988; Whittaker, 1973).

The first two rounds of division are at right angles and give rise to four similarly sized daughter cells. The first division splits the left and right halves of the embryo, and the second

division nominally separates anterior from posterior (Edwin Grant Conklin, 1905). The third round of division is again orthogonal to the prior two and separates the animal and vegetal hemispheres of the embryo. These cleavages are slightly asymmetric in volume, with the animal daughters all somewhat smaller than their vegetal siblings (Edwin Grant Conklin, 1905). Cell divisions remain synchronous through the fourth and fifth cell cycles, but many of the vegetal cell divisions are highly asymmetric with major differences in size and fate between anterior and posterior daughters (Edwin Grant Conklin, 1905; Dumollard et al., 2017; Hibino, Nishikata, & Nishida, 1998; Iseto & Nishida, 1999; Takahito Nishikata, Hibino, & Nishida, 1999; Patalano et al., 2006; Tassy, Daian, Hudson, Bertrand, & Lemaire, 2006). After the 32-cell stage, cell cycle times slow in the vegetal hemisphere to give distinct 44 and 76-cell stages (Dumollard, Hebras, Besnardeau, & McDougall, 2013). Animal cells continue to divide relatively symmetrically to give rise to most of the ectoderm, whereas many of the vegetal divisions are asymmetric in fate and/or size to give rise to a variety of largely mesodermal and endodermal cell types (Edwin Grant Conklin, 1905; Hiroki Nishida, 1987).

Ooplasmic segregation/PEM

Early embryonic patterning depends on two successive cytoplasmic reorganizations in the first cell cycle known as the first and second ooplasmic segregations. Ascidian oocytes are polarized along the animal-vegetal axis prior to fertilization (Sardet, Speksnijder, Terasaki, & Chang, 1992), and the first ooplasmic segregation helps to reinforce this polarity. The second ooplasmic segregation breaks the radial symmetry of the egg and establishes the future anterior-posterior axis. Both phases involve the movement of a class of maternally deposited RNAs collectively known as the postplasmic/PEM (posterior end mark) RNAs (reviewed in (Prodon, Yamada, Shirae-Kurabayashi, Nakamura, & Sasakura, 2007)) along with mitochondria rich

myoplasm and cortical endoplasmic reticulum (ER). The first phase of ooplasmic segregation is influenced by both the animal-vegetal polarization of the oocyte prior to fertilization as well as the site of sperm entry. Sperm entry triggers first a calcium wave and a subsequent contraction wave that concentrates the postplasmic/PEM RNAs and associated factors at the vegetal pole (McDougall & Sardet, 1995; Speksnijder, Sardet, & Jaffe, 1990).

The second phase of ooplasmic segregation is driven by sperm aster microtubules and cortical microfilaments (Chiba et al., 1999). It relocates the vegetal PEM components to a more equatorial position that defines what is widely referred to as the future posterior side of the embryo (Sardet, Speksnijder, & Jaffe, 1989). As in many species, however, this new axis of organization orthogonal to the AV axis is not perfectly congruent with any Cartesian axis of the hatched larva. The cortical ER, postplasmic/PEM RNAs, and myoplasm are inherited by the left and right posterior vegetal blastomeres at the eight-cell stage, and aggregate to form a structure called the centrosome attracting body (CAB) (Hibino et al., 1998). The CAB is continuously partitioned into the posterior-most vegetal cells during the subsequent rounds of division and is responsible for the unequal cleavages characteristic of these lineages (Patalano et al., 2006). Much of the anterior-posterior patterning of the embryo is thought to result directly or indirectly from the asymmetric inheritance of the CAB and the PEM RNAs. This includes a Zic family transcription factor variously known as Macho1 or Zic-r.a that has been identified as one of the key components of Conklin's myoplasm (H. Nishida & Sawada, 2001).

Origin of germ layers

As seen in diverse metazoans (Logan, Miller, Ferkowicz, & McClay, 1999; Miyawaki et al., 2003; Onai, 2019; Wikramanayake et al., 2003), maternal nuclear β-catenin plays a key role in ascidian germ layer specification. β-Catenin signaling is required for endodermal cell fate in

the most vegetal cells as well as mesodermal cell fates in the more marginal vegetal cells. In *Ciona* and other ascidians, this involves two successive β-catenin dependent fate specification events. Nuclear β-catenin is observed in all the mesendodermal precursors at the 16-cell stage and is required for mesendodermal fate (K. Imai, Takada, Satoh, & Satou, 2000). In the next cell cycle, β-catenin becomes restricted to only the most vegetal daughters and is required for the segregation of endoderm from marginal fates including mesoderm and some neural ectoderm (Hudson, Kawai, Negishi, & Yasuo, 2013). In the first specification event, nuclear localization of β-catenin in the vegetal cells is antagonistic to the ubiquitous expression of the maternal transcription factor Gata.a. Gata.a promotes the transcription of ectodermal specific genes in the animal cells (Rothbächer, Bertrand, Lamy, & Lemaire, 2007), while the nuclear localization of β-catenin both prevents the expression of ectodermal genes and promotes expression of mesendodermal genes in the vegetal cells (Kaoru S. Imai, Hudson, Oda-Ishii, Yasuo, & Satou, 2016). The second specification event in the following cell cycle also involves antagonism between vegetal β-catenin signaling and more broadly expressed Gata.a (Kaoru S. Imai et al., 2016), where β-catenin promotes endodermal fate. The precise mechanisms linking preexisting oocyte AV polarity and ooplasmic segregation to β-catenin stabilization and nuclear entry remain unclear. Several downstream targets of β-catenin have been identified, including vegetally-expressed FGFs that are involved in a broad range of cell fate decisions at the margin of the embryo (Hudson, Sirour, & Yasuo, 2016; K. S. Imai, 2003).

Mechanisms of Gastrulation

Most ascidians initiate gastrulation after the seventh cell cycle. For *Ciona* this is ~ 5 h after fertilization at 18 °C (Hotta et al., 2007). The embryo rapidly flattens along the animal-vegetal axis and invaginates to form a cup-shaped early gastrula (Figure 2.2, left). The blastopore constricts over ~ 2 h to bring not just the endoderm but also the notochord, muscle and mesenchyme precursors into the interior of the embryo (Figure 2.2, right).

Endoderm-intrinsic forces in gastrulation

The most detailed mechanistic description of forces driving the morphogenetic events of early tunicate gastrulation used a combination of fixed and live imaging in four different ascidian species (*Ciona intestinalis* type A [now known as *Ciona robusta*], *Ciona savignyi*, *Phallusia mammilata*, and *Boltenia villosa*), all of which show essentially superimposable cleavage patterns and cell-shape changes during gastrulation (Sherrard, Robin, Lemaire, & Munro, 2010). This study generated a comprehensive model of invagination through observation, experimental manipulation and computer simulation. One surprising finding was that force-generating myosin II dynamics intrinsic to the endoderm cells is sufficient to account for invagination. Equally surprising was the finding that the concomitant cell-shape changes such as epiboly outside the endoderm not only do not contribute to invagination but actually oppose it. This is unlike Xenopus (Keller, Davidson, & Shook, 2003), where ectodermal epiboly is thought to help drive endodermal internalization.

Endoderm invagination is the product of two distinct and sequential steps, both driven by myosin II. In the first step the apical (vegetal-most) surfaces of the endoderm cells contract between the late 64-cell and early 112-cell stages (Apical Constriction, Figure 2.3). This step is characterized by the accumulation of activated dynamic myosin II complexes at the contracting

apical surfaces, as seen from immunostaining for ser19-phosphorylated myosin II regulatory light chain (1P-myosin; (Sherrard et al., 2010)). This apical constriction is regulated by the well-described RhoA/ Rho-kinase pathway (Beane, Gross, & McClay, 2006; van Eekelen, Runtuwene, Overvoorde, & den Hertog, 2010) and can be blocked by either dominant negative RhoA or pharmacological inhibition of Rho-kinase.

The second step involves embryonic morphology shifting from a flattened disk to a cup-like shape (Collared Rounding, Figure 2.3). This involves the endoderm cells contracting in the apical-basal dimension to become shorter, while at the same time expanding their basal surfaces contacting the overlying ectoderm. This change in contractility is observed as a redistribution of 1P-myosin staining to the basal and lateral surfaces. Interestingly, this second step is not RhoA dependent. The mechanism that regulates the transition from step 1 to step 2 and that directs the assembly of activated myosin II in the apico-basal axis remains to be determined, but a recent preprint suggests that Nodal and Ephrin signaling may be important (Fiuza, Negishi, Rouan, Yasuo, & Lemaire, 2018).

Importantly, during step 2 the apical surfaces remain constricted, although no further constriction is observed. Immunostaining shows that at the apical surfaces the more dynamic 1P-myosin is replaced with the more stable 2P-myosin which is phosphorylated on both ser19 and thr18 of the regulatory light chain. Pharmacological inhibition of RhoA at later steps of gastrulation causes the apical constrictions to relax, indicating a persistent requirement for this pathway. Collared rounding can occur even if the cell division from 64 to 112 cells is inhibited, indicating that this mechanism is robust.

Endoderm invagination in ascidian gastrulation involves changes in cell shape but no changes in cell-cell contacts. This is unlike many metazoans, where involution, ingression,

intercalation, migration and other large scale tissue rearrangements lead to major changes in cell-cell neighbor relationships. Even in sea urchins, which have a relatively simple gastrulation, the mesenchyme cells delaminate and migrate, and the invaginating endoderm cells also undergo radial intercalation (Ettensohn, 1985, 1999). We speculate that the morphological simplicity of tunicate gastrulation reflects both the small size of the embryo and its very rapid development.

The Sherrard study dived deep into the molecular and biophysical mechanisms of early ascidian gastrulation as the embryo changes from ball-shaped to cup-shaped. Later aspects of gastrulation have not been studied in any detail. It is unknown whether notochord, muscle and mesenchyme are participating more actively later in gastrulation, and the mechanisms driving blastopore closure have not been investigated.

Gastrulation in other Tunicates

As detailed in the Section 1, tunicates are a diverse group of animals with dramatically different larval and adult morphologies. Given this diversity, it is reasonable to assume that the cellular and molecular mechanisms of gastrulation may also vary. Embryos of the ascidian *Halocynthia roretzi*, for example, are much larger than *Ciona* embryos, and have minor differences in early cleavage patterns. *Halocynthia* gastrulation begins at the 110-cell stage (Hiroki Nishida, 1986) instead of the 112-cell stage as seen in *Ciona*. By contrast, the larvacean *Oikopleura dioica*, begins gastrulation at the 32-cell stage < 2 h after fertilization. *Oikopleura* has exceptionally rapid development, with the tadpole larvae hatching in as little as 3 h following fertilization (Fujii, Nishio, & Nishida, 2008; Hiroki Nishida, 2008). Gastrulation in *O. dioica* progresses in two phases. In the first phase, the vegetal-most eight cells invaginate, with the lateral four cells proceeding the central four endoderm cells. In the second phase, cells lateral and posterior cells invaginate. Interestingly, no change to the overall spherical shape of the embryos is evident during gastrulation. Moreover, because of the small number of invaginating cells in the gastrula, there is no obvious blastopore or archenteron. Cellular mechanisms driving invagination in *O. dioica* are not known, but it has been speculated that myosin II-driven apical constriction is important (Fujii et al., 2008).

Colonial tunicates

A subset of ascidian species are colonial and grow by repeated rounds of asexual reproduction (budding) that eventually give rise to a colony of genetically identical individuals, called zooids, arranged within a common tunic. Each zooid can be sexually mature, but colonial reproduction has several notable differences when compared to solitary species, and these have hampered embryological studies. First, all colonial ascidians are brooders, and fertilization and

development occur inside the adult zooids, often with maternal contributions, such as a brood pouch, which can be difficult to replicate in vitro. Development is also significantly slower, on the order of days to a week or more. Finally, the eggs and developing embryos are opaque, hindering high-resolution studies of cell movement. Thus little is known about gastrulation in these species, and there are no recently published studies.

More germane to this review is the potential role of a gastrulation-like process during asexual development. During the budding process, colonial ascidians are regenerating all tissues and organs from a population of pluripotent stem cells. An important question is whether asexual development is controlled by novel genes and gene regulatory networks, or if embryonic pathways and networks are redeployed (Tiozzo, Brown, & De Tomaso, 2008). Interestingly, there are many colonial species scattered throughout the class Ascidiacea, including different monophyletic orders, suggesting that coloniality has arisen independently multiple times. Comparison of these species reveals a diversity of budding modes, including the source of the new body, and the timing of various developmental landmarks (Tiozzo et al., 2008). However, in all species studied to date, asexually developing zooids go through an initial blastula-like stage. This is followed by invaginations and evaginations of the epithelium to form various tissues and organs. While in a sense this resembles gastrulation, these movements do not result in segregation of cells into presumptive germ layers, as they do in embryogenesis. The only species in which asexual budding has been studied at a molecular level is *Botryllus schlosseri* (Manni et al., 2019). In an elegant study by Ricci, Cabrera, Lotito, and Tiozzo (Ricci, Cabrera, Lotito, & Tiozzo, 2016), it was found that there is regionalization of germ layer specific transcription factors in the blastula-like stage and during these epithelial folding events, but they do not correspond to the regions that are folding (i.e., it does not appear that the movement is correlated

to germ layer specification). In this study, it was found that germ layer restricted transcription factors, such as Otx (ectoderm), Fox-A1 (endoderm) and Gsc (mesoderm) are expressed in distinct regions of the blastula-like structure and could be followed through organogenesis. Importantly, the expression of each of these germ layer markers corresponded to the source of mature organs during embryogenesis. For example, the endoderm marker Fox-A1 was initially expressed in a region of the blastula-like vesicle that eventually became the gut, and results were equivalent for ectodermal and mesodermal markers.

Given that coloniality has arisen multiple times, it would hardly be feasible that completely novel mechanisms for regeneration of every tissue and organ also evolved multiple times, and a more parsimonious explanation is that this is due to the ability to coopt embryonic pathways at different times during regeneration. Interestingly though, this does not appear to include a clear recapitulation of embryonic gastrulation.

The thaliaceans: Salps, doliods and pyrosomes

The thaliaceans include three orders of pelagic tunicates: the Pyrosomida, Salpida, and Doliolida. The thaliaceans are more closely related to the ascidians than to the appendicularians (see Section 1), and a conserved anatomy is evident between these two groups, particularly the large pharyngeal basket used for filter feeding in both adult ascidians and thaliaceans. Although the anatomy and reproductive cycles of thaliaceans have been described in reports dating back to the 19th century (see review Piette & Lemaire (Piette & Lemaire, 2015)), much remains unknown about this group of animals. Thaliaceans are more difficult to collect and culture than ascidians, and they do not readily lend themselves to modern experimental methods. Despite their similarities to ascidians, the thaliaceans have diverged extensively and have evolved complex reproductive strategies involving alternating sexual and asexual generations (Holland,

2016; Piette & Lemaire, 2015). Like some ascidian species, salps and pyrosomes can form large colonies comprised of individual zooids produced by asexual budding. While asexual budding and coloniality appear to have evolved independently several times in the ascidians (Brown & Swalla, 2012), the evolutionary history of thaliacean budding is less clear and it is uncertain whether it arose before or after the split with ascidians (see discussion in Piette & Lemaire (Piette & Lemaire, 2015)).

Embryonic development of salps appears to be particularly unusual. The salp lifecycle starts with the sexually produced embryo that goes on to form a single 'oozooid.' The adult oozoid then buds asexually to produce connected chains of 'blastozooids' known as 'aggregates.' Each blastozooid has germ cells that produce first eggs and later sperm. Depending on the species, only a single egg may be produced per blastozooid. Fertilized eggs attach to the adult body wall and develop viviparously. The salp zygote is called the 'blastophore' and its development remains poorly described, particularly with modern molecular tools. A 1960s-era description of blastophore development in *Salpa fusiformis* shows a developing embryo largely unrecognizable to those familiar with ascidian or larvacean embryos ((Sutton, 1960); Figure 2.4). It lacks an obvious notochord or neural tube, and does not produce a tadpole larva. Remarkably, it does not obviously gastrulate. Sutton identified a mass of blastophore cells that he terms 'neuro-chordal,' but these fail to form an identifiable notochord or neural plate and molecular markers of cell identity have not been examined in these cells. The only morphogenic event that might be conflated with gastrulation is the formation of the neuro-chordal invagination (N-C.I. in Figure 2.4). Sutton described the neuro-chordal invagination as the result of infolding caused by the differential growth of adjacent epithelia, but it is unclear whether it bears any relationship to gastrulation or neurulation. Finally, although description of embryonic development of doliolids

and pyrosomes is still incomplete, neither are viviparous, and both reproduce sexually as well as asexually by budding (Holland, 2016; Lemaire, 2011; Lemaire & Piette, 2015). Although neither is thought to show the extreme derivation of development observed in salps, various species within both groups show high, but variable, degrees of degeneration of the tadpole larva morphology. For example, *Doliolum* larvae are reported to make a rudimentary notochord flanked by tail muscle, but no obvious nervous system (Holland, 2016). How these altered larval morphologies may be reflected in earlier gastrula morphologies is currently unknown.

Peri-gastrulation Events

Notochord development

As in vertebrate embryos, early ascidian notochord morphogenesis overlaps with gastrulation. The notochord is divided into two separate developmental lineages. The primary notochord is derived from anterior vegetal (A-line) blastomeres while the secondary notochord is derived from posterior vegetal (B-line) blastomeres (Hiroki Nishida, 1987). Primary notochord fate is induced at the 64-cell stage and secondary notochord at the 112-cell stage via distinct but overlapping mechanisms (Hudson & Yasuo, 2006; Picco, Hudson, & Yasuo, 2007; Yasuo & Hudson, 2007). At the onset of gastrulation, the four primary notochord cells have divided once to form an arc of eight cells that are not yet contiguous with the two secondary notochord precursors (Figure 2.2, yellow asterisks). The two final notochord cell divisions take place during gastrulation. The primary notochord cells are effectively on the anterior lip of the blastopore during the second-last division, and invert during gastrulation so that their previously vegetal surfaces become animal. The final primary notochord division takes place while the blastopore is closing, and is immediately followed by the onset of mediolateral intercalation behaviors that cause the notochord to converge and extend into a single-file column (Munro & Odell, 2002a, 2002b). This is in striking contrast to organisms such as *Drosophila* where the cell cycle pauses in cells that are actively gastrulating (Grosshans & Wieschaus, 2000).

Perhaps the most surprising conclusion from Sherrard et al. (Sherrard et al., 2010) is the apparent absence of a contribution from the axial mesoderm (notochord and tail muscle precursors) to the forces that drive invagination during ascidian gastrulation—at least up through the formation of the cup-shaped gastrula. Although it is possible that the developing axial mesoderm could play a role in later steps, such as blastopore closure, observations of mutant

Ciona, as well as tailless variants of the *Molgulid* species of ascidians, suggest otherwise. As detailed above, ascidians notochord morphogenesis initiates at gastrulation, although extensive convergent extension and elongation of the ascidian notochord is observed most prominently in the neurula embryo (i.e., following the completion of gastrulation) (Smith, 2018). Consistent with the absence of a role for axial mesoderm in invagination, *Ciona* embryos homozygous for the mutation *chobi* have a severe defect in notochord specification due to a mutation in the gene *brachyury* (Chiba, Jiang, Satoh, & Smith, 2009), but nevertheless successfully complete gastrulation and properly close the blastopore. In fact, presumptive notochord cells in *chobi* are transfated to endoderm, further evidencing the robustness of the endoderm invagination mechanisms to perturbations (Sherrard et al., 2010), in this case to increased cell number. Likewise, a number of species of ascidians have been described that differ from the conventional body plan in having no tail, and reduced numbers of notochord and tail muscle cells—the best described of these being *Molgula occulta* (B. J. Swalla, Makabe, Satoh, & Jeffery, 1993; Billie J. Swalla & Jeffery, 1990). Nevertheless, these tailless species gastrulate and close their blastopores. In *M. occulta*, as well as the congeneric tailless species *Molgula tectiformi*, the notochord lineage is present in the blastula embryo, as apparent by the expression of *brachyury*, but these cells fail to follow the full mitotic sequence observed in the tailed *Molgula occulta*, nor do they undergo convergent extension (Takada et al., 2002). Finally, *Ciona* mutant *aimless* carries a null mutation in the gene encoding the essential planar cell polarity (PCP) component Prickle (Jiang, Munro, & Smith, 2005). In the *Ciona* embryo *prickle* expression is limited to the notochord, and homozygous *aimless* embryos have defects in the intercalation of notochord cells, although markers of notochord differentiation are expressed normally. Despite these defects in notochord morphogenesis, *aimless* embryos gastrulate with no obvious defects, although they

have greatly shortened anterior/posterior axes. Thus, the PCP pathway is not required for the basic steps of involution and blastopore closure in *Ciona*. Whether this differs significantly from the role of the PCP pathway in vertebrate gastrulation is unclear. *Xenopus* embryos in which Prickle was knocked down with morpholinos have been described as having severe defects in mesoderm involution (Takeuchi et al., 2003). However, PCP loss of function results in zebrafish appear to be more similar to *Ciona*, with a loss of mediolateral intercalation in axial mesoderm and a resulting shortened axes, but complete involution (Jessen et al., 2002; M. T. Veeman, Axelrod, & Moon, 2003).

After the notochord has intercalated into a single file column of 40 cells, it undergoes considerable further morphogenesis, including cell shape changes and concomitant protein localization (and relocalization) to generate constricted apical domains at the interfaces between the stacked cells (see reviews Denker & Jiang (Denker & Jiang, 2012); Smith (Smith, 2018)). Each notochord cell develops separate anterior and posterior apical domains (Denker, Bocina, & Jiang, 2013). Extracellular lumens then form between the cells, centered at the apical domains. As these lumens expand they fuse to form a continuous inflated, hollow lumen running the length of the notochord and surrounded by the now epithelium-like notochord cells. Moreover, unlike many vertebrates, there is no fate distinction between separate notochord sheath and core cell types. At the same time that the apical domains are forming there is a repolarization of the PCP machinery. Early in notochord development PCP activity drives mediolateral intercalation (Jiang et al., 2005). However, at the completion of intercalation the polarity of PCP activity is repositioned to the anterior/posterior axis (Newman-Smith, Kourakis, Reeves, Veeman, & Smith, 2015). The most obvious manifestation of the PCP-dependent anterior/posterior polarity of the

notochord is the posterior localization of the nucleus, and the anterior localization of the PCP components Prickle and Strabismus, as well as myosin II (reviewed in Smith (Smith, 2018)).

Neural induction and neurulation

In vertebrates, induction of the central nervous system initiates late in the blastula stage and continues through gastrulation. The vertebrate neural-inducing molecules are products of the dorsal lip of the blastopore, a tissue which is variously termed the organizer in amphibians, the shield in teleosts, Hensen's node in chicks and the node in mammals. These inducers act on neighboring ectoderm to initiate the formation of the neural plate. A number of secreted factors have neural-inducing activity, including FGF, and BMP inhibitors such as Noggin and Chordin (see review Stern (Stern, 2005)). The evolutionary similarities with the vertebrates are most evident in the morphology and morphogenesis of the ascidian larval nervous system (see review Hudson (Hudson, 2016)). While there are some parallels between ascidian and vertebrate neural induction, significant departures are also evident.

The *Ciona* neural plate has a remarkably simple structure with a grid-like arrangement of six rows and eight columns of cells that have distinct row and column identities (Hudson et al., 2007). The cells forming the plate come from 3 of the 4 quadrants of the 8-cell embryo and are induced in quite different ways. These include the *a*-lineage which gives rise to the anterior neural plate and goes on to make the anterior brain, palps and presumptive mouth (M. T. Veeman, Newman-Smith, El-Nachef, & Smith, 2010), the *A*-lineage which gives rise to posterior brain and the posterior nerve cord, and the *b*-lineage which gives rise to the dorsal-most row of cells in the posterior brain and posterior nerve chord (neural lineages reviewed in Hudson (Hudson, 2016)). Neural induction in *Ciona* starts at the 32-cell stage with the specification of the *a*-lineage (Bertrand, Hudson, Caillol, Popovici, & Lemaire, 2003) via vegetally expressed

FGF9/16/20 (i.e., the ortholog of vertebrate FGFs 9, 16 and 20). During *a*-lineage neural specification, not only does contact between the inducer cells and the induced ectodermal cells appear to be important, but the area of contact appears to be essential in distinguishing between induced cells and neighboring non-induced cells (Tassy et al., 2006). Neural induction in the *b*-lineage is not well characterized, and the induction of *A*-lineage neural cells is very different than the *a*-lineage. The *A*-lineage of the neural plate becomes fate restricted at the 64-cell stage as the result of asymmetric cell divisions in which *suppression* of FGF signaling is required to suppress notochord fate (Yasuo & Hudson, 2007). While the *Ciona* embryo does express some secreted BMP inhibitors, none have been found to share the critical role in early neural induction seen in vertebrate embryos.

Ciona neurulation is stereotypically chordate, with a neural plate that forms a distinctive midline groove and rolls up to form a hollow, dorsal neural tube (Edwin Grant Conklin, 1905; Nicol & Meinertzhagen, 1988; Satoh, 1978). The onset of neurulation is continuous with the end of gastrulation, with the neural folds first appearing at the posterior of the embryo on either side of the closing blastopore (Nicol & Meinertzhagen, 1988). It is unclear whether this is simply a consequence of rapid early development or whether blastopore closure might be mechanistically important for early neurulation. Neural tube closure progresses from posterior to anterior (Hiroki Nishida, 1986). A transient chordoneural hinge can be seen in phalloidin-stained confocal stacks connecting the forming neural tube lumen to the remnant of the archenteron via the nearly-closed blastopore.

Neurulation first involves the furrowing and formation of a hinge point in the midline of the neural plate around which neural cells will bend as the midline cells constrict apically (Nicol & Meinertzhagen, 1988). Convergence and extension movements narrow the mediolateral axis

and lengthen the anterior-posterior axis of the neural plate as it rolls up (Nicol & Meinertzhagen, 1988). Previously lateral and now dorsal cells meet at the midline and ‘zipper’ together to form a closed neural tube. The posterior to anterior zippering involves contraction of the apical domain of bilateral pairs of neural cells. These contractions are sequential and are punctuated by apical junction exchange and release from one pair of midline cells to another in a posterior to anterior direction (Hashimoto, Robin, Sherrard, & Munro, 2015).

Conclusion

The presence of a number of traits in the tunicates, such as simple and stereotyped lineages, the extreme transparency of some ascidian species such as *Phallusia*, making them ideal for live imaging (Robin et al., 2011), their evolutionary affinity to vertebrates, and the development of a suite of genomic and imaging methods (Stolfi & Christiaen, 2012; M. Veeman & Reeves, 2015), has allowed them to make ongoing contributions to our understanding of gastrulation. Many questions remain, some specific to tunicate gastrulation, and others to chordate gastrulation in general. The apparent differences in the relative importance of endoderm involution in ascidian gastrulation in comparison to vertebrate models in which mesoderm and ectoderm are thought to play more prominent roles, raises the question of whether this is a derived feature of the ascidians. Has a complex gastrulation involving coordinated morphogenetic processes in different germ layers been lost in the ascidians, perhaps as a consequence of embryo simplification, or was a simple gastrulation driven predominantly by endoderm invagination a feature of the last common ancestor of the chordates? We have emphasized in this review the diversity of tunicate morphologies and apparent developmental strategies, although our detailed knowledge is limited to just a few species. Renewed investigation of lesser-studied tunicate clades, such as the salps, with modern methods may reveal new insights into the diversity of chordate developmental strategies, including those for gastrulation.

Acknowledgements

We thank Hiroki Nishida for his helpful discussion of Oikopleura gastrulation. This work support by NIH grant HD038701 to W.C.S., and NIH grant HD085909 and NSF grant IOS 1456555 to M.V.

References – Chapter 2

Beane, W. S., Gross, J. M., & McClay, D. R. (2006). RhoA regulates initiation of invagination, but not convergent extension, during sea urchin gastrulation. *Developmental Biology*, *292*(1), 213–225. https://doi.org/10.1016/j.ydbio.2005.12.031

Bertrand, V., Hudson, C., Caillol, D., Popovici, C., & Lemaire, P. (2003). Neural Tissue in Ascidian Embryos Is Induced by FGF9/16/20, Acting via a Combination of Maternal GATA and Ets Transcription Factors. *Cell*, *115*(5), 615–627. https://doi.org/10.1016/S0092-8674(03)00928-0

Bourlat, S. J., Rota-Stabelli, O., Lanfear, R., & Telford, M. J. (2009). The mitochondrial genome structure of Xenoturbella bocki (phylum Xenoturbellida) is ancestral within the deuterostomes. *BMC Evolutionary Biology*, *9*(1), 1–14. https://doi.org/10.1186/1471-2148-9-107

Brown, F. D., & Swalla, B. J. (2012). Evolution and development of budding by stem cells: Ascidian coloniality as a case study. *Developmental Biology*, *369*(2), 151–162. https://doi.org/10.1016/j.ydbio.2012.05.038

Brusca, R. C., & Brusca, G. J. (1990). *Invertebrates* (1st ed.). Suderland, MA: Sinauer.

Carlson, M., Reeves, W., & Veeman, M. (2015). Stochasticity and stereotypy in the Ciona notochord. *Developmental Biology*, *397*(2), 248–256. https://doi.org/10.1016/j.ydbio.2014.11.016

Chabry, L. (1887). Contribution a l'embryologie normale et teratologique des Ascidies simples. *J. Anat. Physiol.*, *23*, 167–319. Retrieved from http://ci.nii.ac.jp/naid/10008759046/en/

Chiba, S., Jiang, D., Satoh, N., & Smith, W. C. (2009). Brachyury null mutant-induced defects in juvenile ascidian endodermal organs. *Development*, *136*(1), 35–39. https://doi.org/10.1242/dev.030981

Chiba, S., Miki, Y., Ashida, K., Wada, M. R., Tanaka, K. J., Shibata, Y., … Nishikata, T. (1999). Interactions between cytoskeletal components during myoplasm rearrangement in ascidian eggs. *Development, Growth & Differentiation*, *41*(3), 265–272. Retrieved from http://www.ncbi.nlm.nih.gov/pubmed/10400388

Conklin, Edwin G. (1905a). Mosaic development in ascidian eggs. *Journal of Experimental Zoology*, *2*(2), 145–223.

Conklin, Edwin G. (1905b). Organ-forming stubstances in the eggs of ascidians. *Biological Bulletin*, *VIII*(4), 205–230.

Conklin, Edwin Grant. (1905). *The organization and cell-lineage of the ascidian egg* (Vol. 13).

Darwin, C. (1871). *The descent of man, and Selection in relation to sex, Vol 1*. London: John Murray. https://doi.org/10.1037/12293-000

Delsuc, F., Brinkmann, H., Chourrout, D., & Philippe, H. (2006). Tunicates and not cephalochordates are the closest living relatives of vertebrates. *Nature*, *439*(7079), 965–968. https://doi.org/10.1038/nature04336

Delsuc, F., Philippe, H., Tsagkogeorga, G., Simion, P., Tilak, M. K., Turon, X., … Douzery, E. J. P. (2018). A phylogenomic framework and timescale for comparative studies of tunicates. *BMC Biology*, *16*(1), 1–14. https://doi.org/10.1186/s12915-018-0499-2

Denker, E., Bocina, I., & Jiang, D. (2013). Tubulogenesis in a simple cell cord requires the formation of bi-apical cells through two discrete Par domains. *Development*, *140*(14), 2985–2996. https://doi.org/10.1242/dev.092387

Denker, E., & Jiang, D. (2012). Ciona intestinalis notochord as a new model to investigate the cellular and molecular mechanisms of tubulogenesis. *Seminars in Cell and Developmental Biology*, *23*(3), 308–319. https://doi.org/10.1016/j.semcdb.2012.03.004

Dumollard, R., Hebras, C., Besnardeau, L., & McDougall, A. (2013). Beta-catenin patterns the cell cycle during maternal-to-zygotic transition in urochordate embryos. *Developmental Biology*, *384*(2), 331–342. https://doi.org/10.1016/j.ydbio.2013.10.007

Dumollard, R., Minc, N., Salez, G., Aicha, S. Ben, Bekkouche, F., Hebras, C., … McDougall, A. (2017). The invariant cleavage pattern displayed by ascidian embryos depends on spindle positioning along the cell's longest axis in the apical plane and relies on asynchronous cell divisions. *ELife*, *6*, 1–23. https://doi.org/10.7554/eLife.19290

Ettensohn, C. A. (1985). Gastrulation in the sea urchin embryo is accompanied by the rearrangement of invaginating epithelial cells. *Developmental Biology*, *112*(2), 383–390. https://doi.org/10.1016/0012-1606(85)90410-5

Ettensohn, C. A. (1999). Cell movements in the sea urchin embryo. *Current Opinion in Genetics & Development*, *9*(4), 461–465. https://doi.org/10.1016/S0959-437X(99)80070-7

Fischer, J.-L. (1992). The embryological œuvre of Laurent Chabry. *Roux's Archives of Developmental Biology*, *201*(3), 125–127. https://doi.org/10.1007/BF00188709

Fiuza, U., Negishi, T., Rouan, A., Yasuo, H., & Lemaire, P. (2018). Nodal and Eph signalling relay drives the transition between apical constriction and apico-basal shortening during ascidian endoderm invagination. *BioRxiv*, 1–21. https://doi.org/10.1101/418988

Fujii, S., Nishio, T., & Nishida, H. (2008). Cleavage pattern, gastrulation, and neurulation in the appendicularian, Oikopleura dioica. *Development Genes and Evolution*, *218*(2), 69–79. https://doi.org/10.1007/s00427-008-0205-4

Grosshans, J., & Wieschaus, E. (2000). A genetic link between morphogenesis and cell division during formation of the ventral furrow in Drosophila. *Cell*, *101*(5), 523–531. Retrieved from http://www.ncbi.nlm.nih.gov/pubmed/10850494

Haeckel, E. H. P. A. (1895). *Anthropogenie oder Entwicklungsgeschichte des Menschen*.

Hashimoto, H., Robin, F. B., Sherrard, K. M., & Munro, E. M. (2015). Sequential Contraction and Exchange of Apical Junctions Drives Zippering and Neural Tube Closure in a Simple Chordate. *Developmental Cell*, *32*(2), 241–255. https://doi.org/10.1016/j.devcel.2014.12.017

Hibino, T., Nishikata, T., & Nishida, H. (1998). Centrosome-attracting body: a novel structure closely related to unequal cleavages in the ascidian embryo. *Development, Growth & Differentiation*, *40*(1), 85–95. https://doi.org/10.1046/j.1440

Holland, L. Z. (2016). Tunicates. *Current Biology*, *26*(4), R146–R152. https://doi.org/10.1016/j.cub.2015.12.024

Hotta, K., Mitsuhara, K., Takahashi, H., Inaba, K., Oka, K., Gojobori, T., & Ikeo, K. (2007). A web-based interactive developmental table for the ascidian Ciona intestinalis, including 3D real-image embryo reconstructions: I. From fertilized egg to hatching larva. *Developmental Dynamics : An Official Publication of the American Association of Anatomists*, *236*(7), 1790–1805. https://doi.org/10.1002/dvdy.21188

Hudson, C. (2016). The central nervous system of ascidian larvae. *Wiley Interdisciplinary Reviews: Developmental Biology*, *5*(5), 538–561. https://doi.org/10.1002/wdev.239

Hudson, C., Kawai, N., Negishi, T., & Yasuo, H. (2013). β-Catenin-driven binary fate specification segregates germ layers in ascidian embryos. *Current Biology : CB*, *23*(6), 491–495. https://doi.org/10.1016/j.cub.2013.02.005

Hudson, C., Lotito, S., & Yasuo, H. (2007). Sequential and combinatorial inputs from Nodal, Delta2/Notch and FGF/MEK/ERK signalling pathways establish a grid-like organisation of distinct cell identities in the ascidian neural plate. *Development (Cambridge, England)*, *134*(19), 3527–3537. https://doi.org/10.1242/dev.002352

Hudson, C., Sirour, C., & Yasuo, H. (2016). Co-expression of Foxa.a, Foxd and Fgf9/16/20 defines a transient mesendoderm regulatory state in ascidian embryos. *ELife*, *5*, 1–17. https://doi.org/10.7554/eLife.14692

Hudson, C., & Yasuo, H. (2006). A signalling relay involving Nodal and Delta ligands acts during secondary notochord induction in Ciona embryos. *Development (Cambridge, England)*, *133*(15), 2855–2864. https://doi.org/10.1242/dev.02466

Imai, K. S. (2003). A Twist-like bHLH gene is a downstream factor of an endogenous FGF and determines mesenchymal fate in the ascidian embryos. *Development*, *130*(18), 4461–4472. https://doi.org/10.1242/dev.00652

Imai, K., Takada, N., Satoh, N., & Satou, Y. (2000). (Beta)-Catenin Mediates the Specification of Endoderm Cells in Ascidian Embryos. *Development (Cambridge, England)*, *127*(14), 3009–3020. Retrieved from http://www.ncbi.nlm.nih.gov/pubmed/10862739

Imai, Kaoru S., Hudson, C., Oda-Ishii, I., Yasuo, H., & Satou, Y. (2016). Antagonism between β-catenin and Gata.a sequentially segregates the germ layers of ascidian embryos.

Development (Cambridge, England), *143*(22), 4167–4172. https://doi.org/10.1242/dev.141481

Iseto, T., & Nishida, H. (1999). Ultrastructural studies on the centrosome-attracting body: electron-dense matrix and its role in unequal cleavages in ascidian embryos. *Development, Growth & Differentiation*, *41*(5), 601–609. https://doi.org/10.1046/j.1440-169x.1999.00457.x

Jessen, J. R., Topczewski, J., Bingham, S., Sepich, D. S., Marlow, F., Chandrasekhar, A., & Solnica-Krezel, L. (2002). Zebrafish trilobite identifies new roles for Strabismus in gastrulation and neuronal movements. *Nature Cell Biology*, *4*(8), 610–615. https://doi.org/10.1038/ncb828

Jiang, D., Munro, E. M., & Smith, W. C. (2005). Ascidian prickle regulates both mediolateral and anterior-posterior cell polarity of notochord cells. *Current Biology : CB*, *15*(1), 79–85. https://doi.org/10.1016/j.cub.2004.12.041

Keller, R., Davidson, L. A., & Shook, D. R. (2003). How we are shaped: the biomechanics of gastrulation. *Differentiation; Research in Biological Diversity*, *71*(3), 171–205. https://doi.org/10.1046/j.1432-0436.2003.710301.x

Kocot, K. M., Tassia, M. G., Halanych, K. M., & Swalla, B. J. (2018). Phylogenomics offers resolution of major tunicate relationships. *Molecular Phylogenetics and Evolution*, *121*(October 2017), 166–173. https://doi.org/10.1016/j.ympev.2018.01.005

Kovalevskij, A. O. (1866). *Entwickelungsgeschichte der einfachen Ascidien*. Mémoires l'Académie Impériale des Sciences St.Pétersbourg.

Lemaire, P. (2011). Evolutionary crossroads in developmental biology: The tunicates. *Development*, *138*(11), 2143–2152. https://doi.org/10.1242/dev.048975

Lemaire, P., & Piette, J. (2015). Tunicates: Exploring the sea shores and roaming the open ocean. A tribute to Thomas Huxley. *Open Biology*, *5*(6). https://doi.org/10.1098/rsob.150053

Logan, C. Y., Miller, J. R., Ferkowicz, M. J., & McClay, D. R. (1999). Nuclear beta-catenin is required to specify vegetal cell fates in the sea urchin embryo. *Development (Cambridge, England)*, *126*(2), 345–357. Retrieved from http://www.ncbi.nlm.nih.gov/pubmed/9847248

Manni, L., Anselmi, C., Cima, F., Gasparini, F., Voskoboynik, A., Martini, M., … Ballarin, L. (2019). Sixty years of experimental studies on the blastogenesis of the colonial tunicate Botryllus schlosseri. *Developmental Biology*, *448*(2), 293–308. https://doi.org/10.1016/j.ydbio.2018.09.009

McDougall, A., & Sardet, C. (1995). Function and characteristics of repetitive calcium waves associated with meiosis. *Current Biology*, *5*(3), 318–328. Retrieved from http://www.ncbi.nlm.nih.gov/pubmed/7780742

Miyawaki, K., Yamamoto, M., Saito, K., Saito, S., Kobayashi, N., & Matsuda, S. (2003).

Nuclear localization of beta-catenin in vegetal pole cells during early embryogenesis of the starfish Asterina pectinifera. *Development, Growth & Differentiation*, *45*(2), 121–128. Retrieved from http://www.ncbi.nlm.nih.gov/pubmed/12752500

Munro, E. M., & Odell, G. (2002a). Morphogenetic pattern formation during ascidian notochord formation is regulative and highly robust. *Development (Cambridge, England)*, *129*(1), 1–12. Retrieved from http://www.ncbi.nlm.nih.gov/pubmed/11782396

Munro, E. M., & Odell, G. M. (2002b). Polarized basolateral cell motility underlies invagination and convergent extension of the ascidian notochord. *Development (Cambridge, England)*, *129*(1), 13–24. Retrieved from http://www.ncbi.nlm.nih.gov/pubmed/11782397

Newman-Smith, E., Kourakis, M. J., Reeves, W., Veeman, M., & Smith, W. C. (2015). Reciprocal and dynamic polarization of planar cell polarity core components and myosin. *ELife*, *2015*(4), 1–17. https://doi.org/10.7554/eLife.05361

Nicol, D., & Meinertzhagen, I. A. (1988). Development of the central nervous system of the larva of the ascidian, Ciona intestinalis L. II. Neural plate morphogenesis and cell lineages during neurulation. *Developmental Biology*, *130*(2), 737–766. https://doi.org/10.1016/0012-1606(88)90364-8

Nishida, H., & Sawada, K. (2001). macho-1 encodes a localized mRNA in ascidian eggs that specifies muscle fate during embryogenesis. *Nature*, *409*(6821), 724–729. https://doi.org/10.1038/35055568

Nishida, Hiroki. (1986). Cell Division Pattern during Gastrulation of the Ascidian, Halocynthia roretzi. *Development, Growth and Differentiation*, *28*(2), 191–201. https://doi.org/10.1111/j.1440-169X.1986.00191.x

Nishida, Hiroki. (1987). Cell lineage analysis in ascidian embryos by intracellular injection of a tracer enzyme. III. Up to the tissue restricted stage. *Developmental Biology*, *121*(2), 526–541. https://doi.org/10.1126/science.725606

Nishida, Hiroki. (2008). Development of the appendicularian Oikopleura dioica: Culture, genome, and cell lineages. *Development Growth and Differentiation*, *50*(SUPPL. 1). https://doi.org/10.1111/j.1440-169X.2008.01035.x

Nishida, Hiroki, & Satoh, N. (1983). Cell lineage analysis in ascidian embryos by intracellular injection of a tracer enzyme. I. Up to the eight-cell stage. *Developmental Biology*, *99*(2), 382–394. https://doi.org/10.1016/0012-1606(87)90188-6

Nishida, Hiroki, & Satoh, N. (1985). Cell lineage analysis in ascidian embryos by intracellular injection of a tracer enzyme. II. The 16- and 32-cell stages. *Developmental Biology*, *110*(2), 440–454. https://doi.org/10.1016/0012-1606(87)90188-6

Nishikata, T, Mita-Miyazawa, I., Deno, T., & Satoh, N. (1987). Muscle cell differentiation in ascidian embryos analysed with a tissue-specific monoclonal antibody. *Development (Cambridge, England)*, *99*(2), 163–171. Retrieved from

http://www.ncbi.nlm.nih.gov/entrez/query.fcgi?cmd=Retrieve&db=PubMed&dopt=Citation&list_uids=2443339

Nishikata, Takahito, Hibino, T., & Nishida, H. (1999). The centrosome-attracting body, microtubule system, and posterior egg cytoplasm are involved in positioning of cleavage planes in the ascidian embryo. *Developmental Biology*, *209*(1), 72–85. https://doi.org/10.1006/dbio.1999.9244

Okado, H., & Takahashi, K. (1988). A simple "neural induction" model with two interacting cleavage-arrested ascidian blastomeres. *Proceedings of the National Academy of Sciences of the United States of America*, *85*(16), 6197–6201. https://doi.org/10.1073/pnas.85.16.6197

Onai, T. (2019). Canonical Wnt/β-catenin and Notch signaling regulate animal/vegetal axial patterning in the cephalochordate amphioxus. *Evolution & Development*, *21*(1), 31–43. https://doi.org/10.1111/ede.12273

Patalano, S., Prulière, G., Prodon, F., Paix, A., Dru, P., Sardet, C., & Chenevert, J. (2006). The aPKC-PAR-6-PAR-3 cell polarity complex localizes to the centrosome attracting body, a macroscopic cortical structure responsible for asymmetric divisions in the early ascidian embryo. *Journal of Cell Science*, *119*(Pt 8), 1592–1603. https://doi.org/10.1242/jcs.02873

Picco, V., Hudson, C., & Yasuo, H. (2007). Ephrin-Eph signalling drives the asymmetric division of notochord/neural precursors in Ciona embryos. *Development*, *134*(8), 1491–1497. https://doi.org/10.1242/dev.003939

Piette, J., & Lemaire, P. (2015). Thaliaceans, The Neglected Pelagic Relatives of Ascidians: A Developmental and Evolutionary Enigma. *The Quarterly Review of Biology*, *90*(2), 117–145. https://doi.org/10.1086/681440

Prodon, F., Yamada, L., Shirae-Kurabayashi, M., Nakamura, Y., & Sasakura, Y. (2007). Postplasmic/PEM RNAs: a class of localized maternal mRNAs with multiple roles in cell polarity and development in ascidian embryos. *Developmental Dynamics : An Official Publication of the American Association of Anatomists*, *236*(7), 1698–1715. https://doi.org/10.1002/dvdy.21109

Racioppi, C., Kamal, A. K., Razy-Krajka, F., Gambardella, G., Zanetti, L., Di Bernardo, D., … Ristoratore, F. (2014). Fibroblast growth factor signalling controls nervous system patterning and pigment cell formation in Ciona intestinalis. *Nature Communications*, *5*, 1–17. https://doi.org/10.1038/ncomms5830

Ricci, L., Cabrera, F., Lotito, S., & Tiozzo, S. (2016). Redeployment of germ layers related TFs shows regionalized expression during two non-embryonic developments. *Developmental Biology*, *416*(1), 235–248. https://doi.org/10.1016/j.ydbio.2016.05.016

Robin, F. B., Dauga, D., Tassy, O., Sobral, D., Daian, F., & Lemaire, P. (2011). Time-Lapse Imaging of Live Phallusia Embryos for Creating 3D Digital Replicas. *Cold Spring Harbor Protocols*, *2011*(10), pdb.prot065847-pdb.prot065847. https://doi.org/10.1101/pdb.prot065847

Rothbächer, U., Bertrand, V., Lamy, C., & Lemaire, P. (2007). A combinatorial code of maternal GATA, Ets and beta-catenin-TCF transcription factors specifies and patterns the early ascidian ectoderm. *Development (Cambridge, England)*, *134*(22), 4023–4032. https://doi.org/10.1242/dev.010850

Sardet, C., Speksnijder, J., & Jaffe, L. (1989). Fertilization and ooplasmic movements in the ascidian egg. *Development*, *249*, 237–249.

Sardet, C., Speksnijder, J., Terasaki, M., & Chang, P. (1992). Polarity of the ascidian egg cortex before fertilization. *Development (Cambridge, England)*, *115*(1), 221–237. Retrieved from http://www.ncbi.nlm.nih.gov/pubmed/1638982

Satoh, N. (1978). Cellular Morphology and Architecture during Early Morphogenesis of the Ascidian Egg: An Sem Study. *The Biological Bulletin*, *155*(3), 608–614. https://doi.org/10.2307/1540794

Satoh, N., Rokhsar, D., & Nishikawa, T. (2014). Chordate evolution and the three-phylum system. *Proceedings of the Royal Society B: Biological Sciences*, *281*(1794), 20141729. https://doi.org/10.1098/rspb.2014.1729

Sherrard, K., Robin, F., Lemaire, P., & Munro, E. (2010). Sequential activation of apical and basolateral contractility drives ascidian endoderm invagination. *Current Biology*, *20*(17), 1499–1510. https://doi.org/10.1016/j.cub.2010.06.075

Smith, W. C. (2018). Cellular Processes of Notochord Formation. In Y. Sasakura (Ed.), *Transgenic Ascidians* (pp. 165–177). Springer Singapore. https://doi.org/10.1007/978-981-10-7545-2_15

Speksnijder, J. E., Sardet, C., & Jaffe, L. F. (1990). The activation wave of calcium in the ascidian egg and its role in ooplasmic segregation. *The Journal of Cell Biology*, *110*(5), 1589–1598. https://doi.org/10.1083/jcb.110.5.1589

Stern, C. D. (2005). Neural induction: Old problem, new findings, yet more questions. *Development*, *132*(9), 2007–2021. https://doi.org/10.1242/dev.01794

Stolfi, A., & Christiaen, L. (2012). Genetic and genomic toolbox of the Chordate Ciona intestinalis. *Genetics*, *192*(1), 55–66. https://doi.org/10.1534/genetics.112.140590

Stolfi, A., & Levine, M. (2011). Neuronal subtype specification in the spinal cord of a protovertebrate. *Development (Cambridge, England)*, *138*(5), 995–1004. https://doi.org/10.1242/dev.061507

Stolfi, A., Ryan, K., Meinertzhagen, I. A., & Christiaen, L. (2015). Migratory neuronal progenitors arise from the neural plate borders in tunicates. *Nature*, *527*(7578), 371–374. https://doi.org/10.1038/nature15758

Stolfi, A., Wagner, E., Taliaferro, J. M., Chou, S., & Levine, M. (2011). Neural tube patterning by Ephrin, FGF and Notch signaling relays. *Development (Cambridge, England)*, *138*(24),

5429–5439. https://doi.org/10.1242/dev.072108

Sutton, M. F. (1960). The Sexual Development of Salpa fusiformis (Cuvier): Part I. *Development*, *8*(3), 268–290.

Swalla, B. J., Makabe, K. W., Satoh, N., & Jeffery, W. R. (1993). Novel genes expressed differentially in ascidians with alternate modes of development. *Development*, *119*(2), 307–318.

Swalla, Billie J., & Jeffery, W. R. (1990). Interspecific hybridization between an anural and urodele ascidian: Differential expression of urodele features suggests multiple mechanisms control anural development. *Developmental Biology*, *142*(2), 319–334. https://doi.org/10.1016/0012-1606(90)90353-K

Takada, N., York, J., Davis, J. M., Schumpert, B., Yasuo, H., Satoh, N., & Swalla, B. J. (2002). Brachyury expression in tailless Molgulid ascidian embryos. *Evolution and Development*, *4*(3), 205–211. https://doi.org/10.1046/j.1525-142X.2002.02004.x

Tassy, O., Daian, F., Hudson, C., Bertrand, V., & Lemaire, P. (2006). A quantitative approach to the study of cell shapes and interactions during early chordate embryogenesis. *Current Biology : CB*, *16*(4), 345–358. https://doi.org/10.1016/j.cub.2005.12.044

Tiozzo, S., Brown, F. D., & De Tomaso, A. W. (2008). Regeneration and Stem Cells in Ascidians. In *Stem Cells: From Hydra to Man* (pp. 95–112). https://doi.org/10.1007/978-1-4020-8274-0

Tokuoka, M., Imai, K. S., Satou, Y., & Satoh, N. (2004). Three distinct lineages of mesenchymal cells in Ciona intestinalis embryos demonstrated by specific gene expression. *Developmental Biology*, *274*(1), 211–224. https://doi.org/10.1016/j.ydbio.2004.07.007

van Eekelen, M., Runtuwene, V., Overvoorde, J., & den Hertog, J. (2010). RPTPα and PTPε signaling via Fyn/Yes and RhoA is essential for zebrafish convergence and extension cell movements during gastrulation. *Developmental Biology*, *340*(2), 626–639. https://doi.org/10.1016/j.ydbio.2010.02.026

Veeman, M., & Reeves, W. (2015). Quantitative and in toto imaging in ascidians: Working toward an image-centric systems biology of chordate morphogenesis. *Genesis*, *53*(1), 143–159. https://doi.org/10.1002/dvg.22828

Veeman, M. T., Axelrod, J. D., & Moon, R. T. (2003). A Second CanonFunctions and Mechanisms of β-Catenin-Independent Wnt Signaling. *Developmental Cell*, *5*(3), 367–377. https://doi.org/10.1016/S1534-5807(03)00266-1

Veeman, M. T., Newman-Smith, E., El-Nachef, D., & Smith, W. C. (2010). The ascidian mouth opening is derived from the anterior neuropore: Reassessing the mouth/neural tube relationship in chordate evolution. *Developmental Biology*, *344*(1), 138–149. https://doi.org/10.1016/j.ydbio.2010.04.028

Wang, W., Niu, X., Stuart, T., Jullian, E., Mauck, W. M., Kelly, R. G., … Christiaen, L. (2019). A single-cell transcriptional roadmap for cardiopharyngeal fate diversification. *Nature Cell Biology*, *21*(6), 674–686. https://doi.org/10.1038/s41556-019-0336-z

Whittaker, J. R. (1973). Segregation during ascidian embryogenesis of egg cytoplasmic information for tissue-specific enzyme development. *Proceedings of the National Academy of Sciences of the United States of America*, *70*(7), 2096–2100. https://doi.org/10.1073/pnas.70.7.2096

Wikramanayake, A. H., Hong, M., Lee, P. N., Pang, K., Byrum, C. A., Bince, J. M., … Martindale, M. Q. (2003). An ancient role for nuclear beta-catenin in the evolution of axial polarity and germ layer segregation. *Nature*, *426*(6965), 446–450. https://doi.org/10.1038/nature02113

WoRMS. (2019). WoRMS - World register of marine species. Retrieved from http://www.marinespecies.org

Yasuo, H., & Hudson, C. (2007). FGF8/17/18 functions together with FGF9/16/20 during formation of the notochord in Ciona embryos. *Developmental Biology*, *302*(1), 92–103. https://doi.org/10.1016/j.ydbio.2006.08.075

Figures – Chapter 2

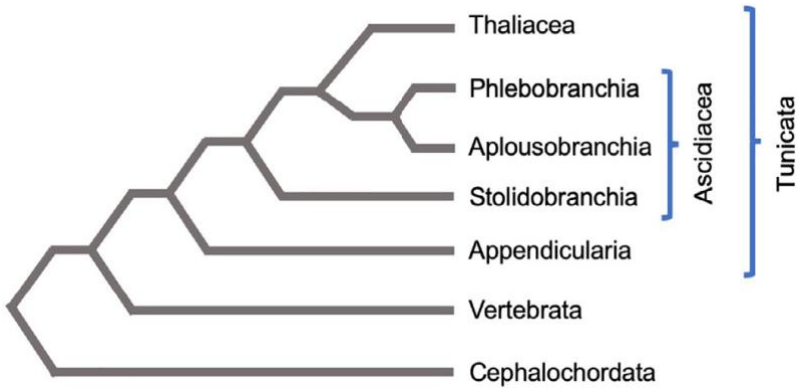

Figure 2.1 Phylogenetic relationships between the chordates, with emphasis on the tunicate clade

Tunicates and vertebrates share a more recent common ancestor than either do with cephalochordates. Because larvaceans (Appendicularia) are basal in the Tunicata, the ancestral tunicate may have been pelagic. The Ascidiacea are revealed to be paraphyletic due to the placement of the Thaliacea as sister to Phlebobranchia/Aplousiobranchia. Branch lengths are not to scale. Based on Kocot, K. M., Tassia, M. G., Halanych, K. M., & Swalla, B. J. (2018). Phylogenomics offers resolution of major tunicate relationships. Molecular Phylogenetics and Evolution, 121, 166–173 doi:10.1016/j.ympev.2018.01.005; Delsuc, F., Philippe, H., Tsagkogeorga, G., Simion, P., Tilak, M.K., Turon, X., et al. A phylogenomic framework and timescale for comparative studies of tunicates. BMC Biology doi:10.1186/ s12915-018-0499-2.

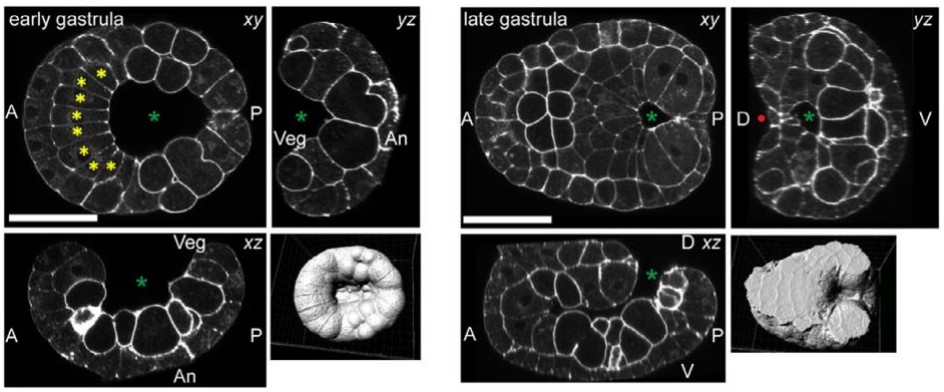

Figure 2.2 Ciona gastrulation.

Confocal images of gastrulating *Ciona robusta* embryos at the stages indicated. The panels on the left are derived from confocal stacks of a phalloidin stained embryo early in gastrulation, with orthogonal xy, xz and yz sections shown. The surface-rendered view of the stack is from the vegetal side. The green asterisk marks the open blastopore/archenteron. Yellow asterisks mark notochord precursor cells. The panels on the right show an older embryo near the end of gastrulation/beginning of neurulation. The red dot indicates the neural groove just starting to form on the posterior dorsal side. Scale bars=50μm.

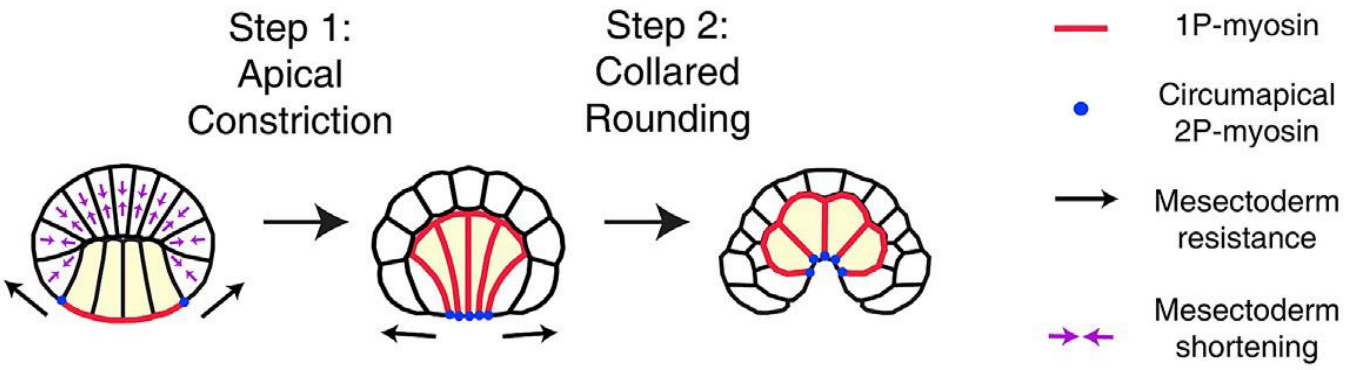

Figure 2.3 Two-step model for endoderm invagination in ascidian development.

Figure from Sherrard, K., Robin, F., Lemaire, P., & Munro, E. (2010). Sequential activation of apical and basolateral contractility drives ascidian endoderm invagination. Current Biology, 20, 1499–1510. doi:https://doi.org/10.1016/j.cub.2010.06.075 (web archive link).

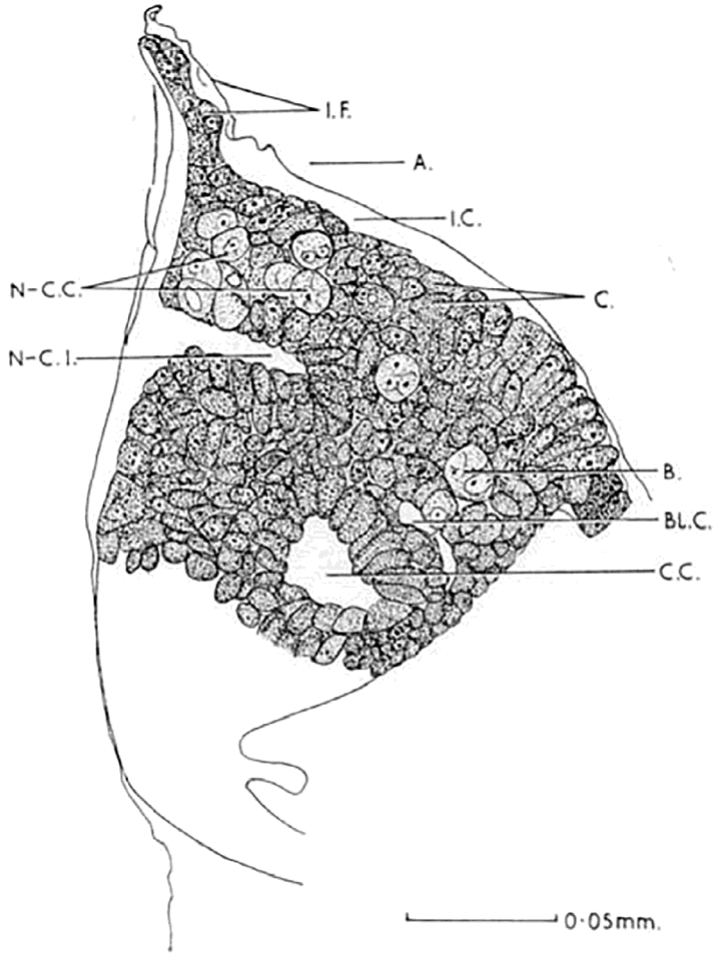

Figure 2.4 Blastophore of *Salpa fusiformis*.

The precise developmental age of the blastophore is not known. Abbreviations: I.F., Incubation fold; A., atrium; I.C., incubation cavity; C., calymnocyte; B., blastomere; C.C., central cavity; N-C.I., neuro-chordal invagination; N-C.C. Neuro-chordal cells. Image from Sutton, M. F. (1960). The sexual development of Salpa fusiformis (Cuvier): Part I. Journal of Embryology and Experimental Morphology, 8, 268–290.

Chapter 3 - A temperature-adjusted developmental timer for precise embryonic staging

Abstract

Developmental biology research depends on careful staging of developing embryos, but the rate of development is extremely sensitive to the temperature at which embryos are raised. It is not always practical to grow embryos at a precisely controlled temperature, so here we describe a simple, inexpensive device based on an Arduino-compatible microprocessor and temperature sensor that provides a metric of developmental time that compensates for changes in temperature. The underlying assumption is that the rate of development will be linear with respect to temperature over an organism's thermal tolerance range. The device measures the ambient temperature and integrates effective degree-minutes over time. For convenience, this is displayed to the user as a temperature-adjusted standard developmental time. In initial testing we have found the device to be extremely helpful for fixing Ciona embryos during precise developmental windows.

Introduction and Results

Developmental biologists depend upon staging series to provide a common nomenclature and set of reference points to describe the progression of embryonic development. For poikilotherms (animals that do not regulate their own body temperature), staging series are usually referenced to a standard temperature. The zebrafish staging series, for example, describes the stages of embryonic development at a standard temperature of 28.5°C (Kimmel, Ballard, Kimmel, Ullmann, & Schilling, 1995), whereas the staging series for the ascidian Ciona describes development at 18°C (Hotta et al., 2007). Development typically occurs normally, however, over a broader thermal tolerance range. Experimenters will sometimes exploit this to speed up or slow down development for experimental convenience. Growing embryos at precisely controlled temperatures can be surprisingly challenging. Room temperatures fluctuate considerably in most buildings. Temperature controlled incubators are often imperfectly adjusted or calibrated, and are subject to fluctuations from the heater or cooler cycling on and off, or the door being opened and shut. Experiments also frequently require embryos to be removed from incubators periodically for various manipulations.

The inspiration for the device developed here came from our lab's ongoing research on notochord morphogenesis in the simple ascidian chordate Ciona (Carlson, Reeves, & Veeman, 2015; W. M. Reeves, Wu, Harder, & Veeman, 2017; W. Reeves, Thayer, & Veeman, 2014). We frequently found ourselves collecting closely spaced time series of embryos so as to be able to fix, stain and image embryos at very specific points in development such as precise stages of cell cycles in specific blastomeres. These precise stages can only be distinguished after embryos have been fixed and imaged by confocal microscopy. Ciona development is highly stereotyped, but we found that we were often missing the desired stages because our embryology room was

slightly cooler or warmer than usual. Rearing embryos in temperature controlled incubators is helpful, but even there the eggs/embryos have to be out of the incubator for varying amounts of time to fertilize and dechorionate them, sort out embryos with normal development, fix time-points and other experimental manipulations.

We hypothesized that constant temperature monitoring would allow much more accurate staging of developing embryos. For most poikilothermic model organisms, the rate of development is thought to vary approximately linearly with respect to temperature within the organism's thermal tolerance range (Damos & Savopoulou-Soultani, 2012; Trudgill, Honek, Li, & Straalen, 2005). Various temperature loggers are commercially available that allow temperature to be recorded over time and retrospectively analyzed, but we were not able to identify any that could be configured or programed to show a running measure of temperature integrated over time or any related metric that would be useful in staging embryos grown under fluctuating temperatures. It occurred to us, however, that such a device could be easily built and programed using an Arduino-compatible microcontroller connected to a temperature probe and a small display.

Relationship between temperature and developmental rate

The influence of temperature upon the rate of development has been widely investigated in both plant and animal systems. Experimenters have generally found that, within an organism's thermal tolerance range, there is a linear relationship between the rate of development (the reciprocal of the length of time it takes to achieve some developmental landmark) and temperature (reviewed by Trudgill et al., 2005; Damos and Savopoulou-Soultani, 2012). This linear relationship can be represented by an equation in the form $r=aT+b$ where T is temperature, a gives the slope and b the y-intercept. The x-intercept of this line is $-b/a$ and it represents the

theoretical temperature at which the velocity of development drops to 0. The length of time (D) it takes to reach a given developmental landmark can then be represented as D=K/(T-T0) where T is the actual temperature, T0 is the developmental zero temperature and K is a thermal time constant (degree-minutes above T0 needed to reach the landmark). The relationship between developmental time at temperature T and a reference temperature Tref can thus be represented as Dref=D(T-T0)/(Tref-T0).

It follows that the only species-specific parameter needed to relate developmental time to a reference temperature is the species' developmental zero temperature T0. This can be estimated by growing embryos at multiple temperatures, plotting the rate of development as a function of temperature, and then finding the x-intercept of the linear regression line. T0 values have been published for many species, but not for Ciona. The Ciona staging series paper, however, contains information on the time it takes to reach key stages at several different temperatures (Hotta et al., 2007). We were able to use this data to estimate that the T0 for the Japanese population of Ciona studied in that paper is ~1°C. We made this estimate based on a linear regression of the reciprocal of the time it took for embryos grown at four different temperatures to reach Stage 19, using data extracted from Supplemental Fig. 1 in Hotta et al.'s paper. Our lab uses Ciona from the much warmer San Diego bay area and we have found that their T0 seems to be considerably higher at ~7.5°C (data not shown). This parameter may need to be optimized for different populations, especially if they are wild-caught populations from different climates. The thermal biology of Ciona embryonic development is underexplored, but wild populations are known to span a broad range of temperatures (Bouchemousse, Lévêque, Dubois, & Viard, 2016).

Design and construction

The Arduino platform and integrated development environment allows scientists such as ourselves with minimal electronics experience to build and program simple microcontroller-based devices (Pearce, 2012). Our guiding principle in designing the Temperature-Adjusted Developmental Timer (TADT) device was that it should require a minimum of soldering and be straightforward to build, making it as easy as possible for both ourselves and other developmental biology labs to build their own instruments.

We chose the Arduino-compatible Feather board from Adafruit (New York, USA) as the heart of the device because it is smaller than a standard Arduino UNO but has an integrated lithium-polymer (LiPo) battery controller and a good ecosystem of commercially available add-on boards ('FeatherWings') including an excellent OLED display. We used a DS18B20 digital temperature sensor because it is relatively precise and accurate, inexpensive, and easy to connect to an Arduino. We also chose the Adafruit Terminal Block Wing because it provides a straightforward way to connect the temperature sensor wiring and incorporate a needed pull-up resistor with a minimum of soldering.

The bill of materials is shown in Table 2.1, and the entire device can be built for only US$80 as of June 2017. Step by step assembly instructions are as follows:

1) Solder stacking headers onto the Feather board (they can be easily held in place for soldering by using a pair of non-stacking headers inserted into a solderless breadboard) (Figure 3.1 A,B).
2) Insert the long sides of the headers from the OLED display into the female side of the stacking headers now soldered onto the Feather (one set will need to be trimmed to the

correct length). Place the OLED display on top of these and solder the headers into place (Figure 3.1 C-E).

3) Solder a short piece of 22AWG hook-up wire and a 4.7K ohm resistor onto the Terminal Block Wing as shown in Figure 3.2 A,B. This acts as a pull-up resistor between the 3.3v power source and general purpose input/output pin 5 (GPIO5).

4) Connect the wires from the temperature sensor to the terminal blocks as shown in Figure 3.2 B,C. The red wire connects to 3v power, the blue wire to ground and the yellow wire to GPIO5.

5) Stack the Feather board on top of the Terminal Block Wing and the OLED wing on top of the Feather (Figure 3.2 and Figure 3.3).

6) Connect the LiPo battery to the JST connector on the Feather board. (The battery is optional. The device will work well without it as long as it is connected to a USB power source. The battery provides a measure of convenience in case of a power outage or accidental disconnection, or if it has to be moved farther than the USB cable can reach. The battery and charging circuit have extensive safety features, but there are fire hazards associated with lithium batteries and builders should make their own decisions as to whether battery power is appropriate.)

Enclosure

The device can be used as is, but it is desirable to house it in an enclosure to protect it and give it a more finished appearance. We designed a two-piece enclosure suitable for 3D printing (Figure 3.4). The enclosure consisted of a lower base piece (base.stl, downloadable from https://github.com/chordmorph/TADT) and an upper lid (lid.stl, downloadable from https://github.com/chordmorph/TADT) and can be printed using inexpensive polylactic

acid (PLA) filament in a hobby-style 3D printer; in our case a Makerbot 5 at the KSU Hale library. The base piece has mounting points which align to the mounting holes on the breakout board, allowing it to be screwed solidly in place. There are holes in the case for the temperature probe cable and to allow access to the power switch, the micro-USB port, and the display. Alternatively, the TADT can be made to fit relatively easily in an inexpensive model 7593K26 enclosure from McMaster-Carr. We cut an opening in the top to fit the OLED display and openings in the side to pass the temperature and USB cables into the enclosure and allow access to the on/off switch. A scrap piece of ¼″ (5 mm) acrylic was cut to use as a spacer to raise the top of the display close to flush with the opening. The spacer and protowing were then mounted semi-permanently into the case bottom with hot melt glue (not shown).

Software

The program (‘sketch’ in Arduino terminology) we have written to control the device is conceptually very simple (TADT.ino, downloadable from https://github.com/chordmorph/TADT). Every second, it polls the temperature probe to determine the current temperature. It then keeps a cumulative tally of degree-minutes above T0 (for implementation reasons it is actually degree-milliseconds since the sketch started running). This cumulative effective temperature can be converted back into a measure of time corrected to a reference temperature by dividing by Tref-T0. The sketch then uses the OLED display to show four different experimental values of interest including the current temperature, the mean temperature over the course of the experiment, the time elapsed since the sketch started and the temperature-adjusted time elapsed. As a convenience, it also displays the battery voltage as an indication of charge status, as well as the T0 and Tref values and an optional offset value used to calibrate the temperature sensor (Figure 3.3 B).

The sketch depends on several libraries, including the Onewire library to connect to the DS18B20 temperature sensor using the Dallas/Maxim 1-wire protocol, the Adafruit_GFX base library for displaying text and graphics on various small displays and the Adafruit_SSD1306 library that adds specific support for the 128×32 OLED display and driver chip used in the OLED FeatherWing. The Onewire library only provides very basic support for communicating with 1-wire devices, and additional code is needed to actually power the sensor and obtain temperature readings. We used a function obtained online from bildr.org that is simple and well documented (https://github.com/bildr-org/DS18B20, http://bildr.org/2011/07/ds18b20-arduino/). Excellent instructions for configuring and using the Feather board are available from Adafruit (https://learn.adafruit.com/adafruit-feather-32u4-basic-proto/arduino-ide-setup).

1) Download the Arduino IDE from www.arduino.cc.

2) Open it, go to File>Preferences>Additional Boards Manager URLs and add https://adafruit.github.io/arduino-board-index/package_adafruit_index.json to the dialog box.

3) Tools>Boards>Board Manager select 'Adafruit AVR Boards' to add support for the Feather 32u4.

4) Close and reopen the IDE and go to Tools>Boards>Feather 32u4.

5) Go to Sketch>Include Library>Manage Library.

6) Use the library manager to install the following libraries:

Onewire (used for communicating with the DS18B20 temperature sensor)

Adafruit_GFX (base library for displaying text and graphics)

Adafruit_SSD1306 (adds specific support for the 128×32 OLED)

7) Copy the TADT sketch (https://github.com/chordmorph/TADT/blob/master/TADT.ino) into your Arduino sketchbook folder (likely/Documents/Arduino).

8) Open the TADT sketch in the IDE.

9) Connect the device to the computer with a suitable USB cable.

10) Once the Feather board has been recognized by the IDE, it should become visible and can be selected under Tools>Port.

11) Upload the sketch to the board by clicking the upload button in the sketch window.

Configuring the device

There are three parameters that can be changed in the sketch. Two of these are constants for the linear degree minute model, including the developmental zero temperature T0 and the reference temperature Tref. These are set by default to 7.5°C and 18.0°C for Ciona, but can be changed in the sketch and then re-uploaded to the device. There is also an offset value that can be adjusted to calibrate the DS18B20 temperature sensor (set to 0°C by default). An easy test can be performed by swirling the temperature sensor in an ice/water bath. If the sensor reads above 0°C, then a negative offset can be used to correct it and vice-versa. The DS18B20 is specified as being accurate to within±0.5°C, but of the five sensors we have tested, we have found three of them to be within ~0.1°C of 0 in an ice/water bath. The other two were both more than half a degree off and behaved unpredictably across changing temperatures. The temperature sensor is inexpensive (US$10) so we suggest buying a few more than needed and discarding any defective ones.

Using the device

The TADT device will begin measuring the temperature and calculating temperature-adjusted minutes as soon as it is powered up using the switch on the terminal block wing. The

temperature probe should be kept as near as possible to the embryos of interest (Figure 3.3 C). The device can be reset using the reset button on the top left of the display. We usually turn the device on and let the temperature probe equilibrate with the surroundings prior to fertilizing embryos, and then hit the reset button immediately after adding sperm to the eggs. The other three buttons on the display board are not used in the current implementation. For long-term use, it is best to keep it attached to a USB power source, but the LiPo battery (if used) will power it for several hours. The battery voltage will read ~4.2v when fully charged and drop to ~3.4v when nearly discharged.

Biological validation

In initial trials we estimated that the T0 of our Ciona collected from San Diego area marinas was ~7.5°C, and that the final cell division in the primary notochord lineage takes place at approximately 400 min post-fertilization at the reference temperature of 18°C. To test the TADT, we grew dechorionated sibling embryos from a single fertilization in two different incubators set to approximately 18°C and 20°C, as well as on the benchtop at approximately 21°C. We used three different TADTs to simultaneously monitor each group of embryos and found that the actual mean temperature of each condition was approximately 18.0°C, 20.1°C and 21.1°C. We repeated the experiment, this time with mean temperatures of 18.2°C, 19.5°C and 21.2°C. For each temperature/replicate, we fixed embryos at 390, 400 and 410 adjusted minutes (for some replicates we also collected a 420 adjusted minute time-point). For each batch of fixed embryos, we also recorded the time elapsed in actual minutes. We stained the embryos and imaged four each at each time-point/temperature/replicate by confocal microscopy. We then scored each of the 16 primary notochord precursor cells per embryo for whether it was premitotic, mitotic or postmitotic with respect to the final notochord cell division. As shown

in Figure 3.5, the timing of this cell division is closely aligned between the different temperatures when measured in temperature-adjusted minutes despite being widely separated in real time.

Discussion

We initially built a prototype device using an Arduino with an LCD display, and have since built three ‘production’ devices using Feather 32u4 boards. The hardware and software are both very simple, and it would be easy to implement a similar concept using many different processor boards, temperature sensors and displays. Only two parameters in the code need to be changed to adjust the reference temperature and developmental zero temperature. We also include a software calibration parameter that can be used to adjust for slight differences between different DS18B20 temperature sensors. The software can easily be customized to display different measurements of interest. One could, for example, directly display integrated degree-minutes, convert the data into a percentile score (e.g. 17% of normal development) or provide a continuous estimate mapped onto a discrete staging series (e.g. Stage 3.35).

The TADT works well in our hands, but we anticipate several potential improvements. The DSB18B20 digital temperature sensor could be replaced with a more accurate and precise platinum thermocouple. It would also be relatively straightforward to integrate a data logging capability to record a detailed temperature trajectory for each experiment. Adafruit sells a version of the Feather with an integrated SD card holder that would work well for this. Another potential improvement would be to incorporate a more sophisticated model of the relationship between temperature and the rate of development. The linear degree-minute model used here was effective for Ciona over the timeframe tested, but more sophisticated non-linear models have been developed in other contexts (Schoolfield, Sharpe, & Magnuson, 1981; Shi, Ikemoto, Egami, Sun, & Ge, 2011).

Our use case here was to help fix embryos during very precise developmental windows, but there are many contexts in which thermal time would provide a fine-grained and inherently

temperature-compensated staging metric for developmental biology research. More work will be needed to determine the variation in T0 across different populations of Ciona and to test whether a linear model is appropriate across a broader range of stages and temperatures, but the concept appears broadly valid and the device is easily configurable for other model organisms. A potential complication for wild-caught animals as used by most Ciona labs is that there is considerable seasonal variation in ocean temperature and there may be seasonal plasticity in thermal biology. We have not yet addressed this issue, but the TADT provides a framework for doing so. Modern hobbyist 'maker-movement' microcontrollers make custom instrumentation of this sort increasingly accessible.

Materials and Methods

Adult Ciona intestinalis Type A (recently renamed Ciona robusta) (Bouchemousse, Liautard-Haag, Bierne, & Viard, 2016; Pennati et al., 2015) were obtained from Marine Research and Educational Products (San Diego, USA). Fertilizations and dechorionations used standard methods (Veeman, Chiba, & Smith, 2011). Embryos were fixed in 2% paraformaldehyde in seawater and stained with Alexa488 phalloidin (Invitrogen). Confocal z-stacks were collected on a Zeiss 880 LSCM using a 40× 1.3NA objective. Primary notochord cells were manually scored for cell cycle stage based on tissue morphology and the presence/absence of a distinct nucleus.

Acknowledgements

We gratefully acknowledge support from the Kansas State University College of Veterinary Medicine Confocal Core.

References – Chapter 3

Bouchemousse, S., Lévêque, L., Dubois, G., & Viard, F. (2016). Co-occurrence and reproductive synchrony do not ensure hybridization between an alien tunicate and its interfertile native congener. *Evolutionary Ecology*, *30*(1), 69–87. https://doi.org/10.1007/s10682-015-9788-1

Bouchemousse, S., Liautard-Haag, C., Bierne, N., & Viard, F. (2016). Distinguishing contemporary hybridization from past introgression with postgenomic ancestry-informative SNPs in strongly differentiated Ciona species. *Molecular Ecology*, *25*(21), 5527–5542. https://doi.org/10.1111/mec.13854

Carlson, M., Reeves, W., & Veeman, M. (2015). Stochasticity and stereotypy in the Ciona notochord. *Developmental Biology*, *397*(2), 248–256. https://doi.org/10.1016/j.ydbio.2014.11.016

Damos, P., & Savopoulou-Soultani, M. (2012). Temperature-Driven Models for Insect Development and Vital Thermal Requirements. *Psyche: A Journal of Entomology*, *2012*, 1–13. https://doi.org/10.1155/2012/123405

Hotta, K., Mitsuhara, K., Takahashi, H., Inaba, K., Oka, K., Gojobori, T., & Ikeo, K. (2007). A web-based interactive developmental table for the ascidian Ciona intestinalis, including 3D real-image embryo reconstructions: I. From fertilized egg to hatching larva. *Developmental Dynamics : An Official Publication of the American Association of Anatomists*, *236*(7), 1790–1805. https://doi.org/10.1002/dvdy.21188

Kimmel, C. B., Ballard, W. W., Kimmel, S. R., Ullmann, B., & Schilling, T. F. (1995). Stages of embryonic development of the zebrafish. *Developmental Dynamics*, *203*(3), 253–310. https://doi.org/10.1002/aja.1002030302

Pearce, J. M. (2012). Building Research Equipment with Free, Open-Source Hardware. *Science*, *337*(6100), 1303–1304. https://doi.org/10.1126/science.1228183

Pennati, R., Ficetola, G. F., Brunetti, R., Caicci, F., Gasparini, F., Griggio, F., … Manni, L. (2015). Morphological Differences between Larvae of the Ciona intestinalis Species Complex: Hints for a Valid Taxonomic Definition of Distinct Species. *PLOS ONE*, *10*(5), e0122879. https://doi.org/10.1371/journal.pone.0122879

Reeves, W. M., Wu, Y., Harder, M. J., & Veeman, M. T. (2017). Functional and evolutionary insights from the Ciona notochord transcriptome. *Development*, *144*(18), 3375–3387. https://doi.org/10.1242/dev.156174

Reeves, W., Thayer, R., & Veeman, M. (2014). Anterior-posterior regionalized gene expression in the Ciona notochord. *Developmental Dynamics*, *243*(4), 612–620. https://doi.org/10.1002/dvdy.24101

Schoolfield, R. M., Sharpe, P. J. H., & Magnuson, C. E. (1981). Non-linear regression of biological temperature-dependent rate models based on absolute reaction-rate theory.

Journal of Theoretical Biology, *88*(4), 719–731. https://doi.org/https://doi.org/10.1016/0022-5193(81)90246-0

Shi, P., Ikemoto, T., Egami, C., Sun, Y., & Ge, F. (2011). A Modified Program for Estimating the Parameters of the SSI Model. *Environmental Entomology*, *40*(2), 462–469. https://doi.org/10.1603/EN10265

Trudgill, D. L., Honek, A., Li, D., & Straalen, N. M. (2005). Thermal time - concepts and utility. *Annals of Applied Biology*, *146*(1), 1–14. https://doi.org/10.1111/j.1744-7348.2005.04088.x

Veeman, M. T., Chiba, S., & Smith, W. C. (2011). Ciona Genetics. In F. J. Pelegri (Ed.), *Methods in molecular biology (Clifton, N.J.)* (Vol. 770, pp. 401–422). Totowa, NJ: Humana Press. https://doi.org/10.1007/978-1-61779-210-6_15

Tables and Figures – Chapter 3

Item	Supplier	Catalog number	Number Required	Price in US$ (each)
DS18B20 Waterproof Digital Temperature Sensor (includes pull-up resistor)	Adafruit	381	1	9.95
Terminal Block Breakout FeatherWing	Adafruit	2926	1	14.95
Feather Stacking Headers	Adafruit	2830	1	1.25
3.7V 500nAh LiPo battery	Adafruit	1578	1	7.95
Feather 32u4 Basic Proto Board	Adafruit	2771	1	19.95
FeatherWing 128x32 OLED Display	Adafruit	2900	1	14.95
USB A/Micro Cable	Adafruit	2185	1	4.95
5V 1A USB Power Supply	Adafruit	501	1	5.95

Table 3.1 Bill of materials for the Temperature-Adjusted Developmental Timer

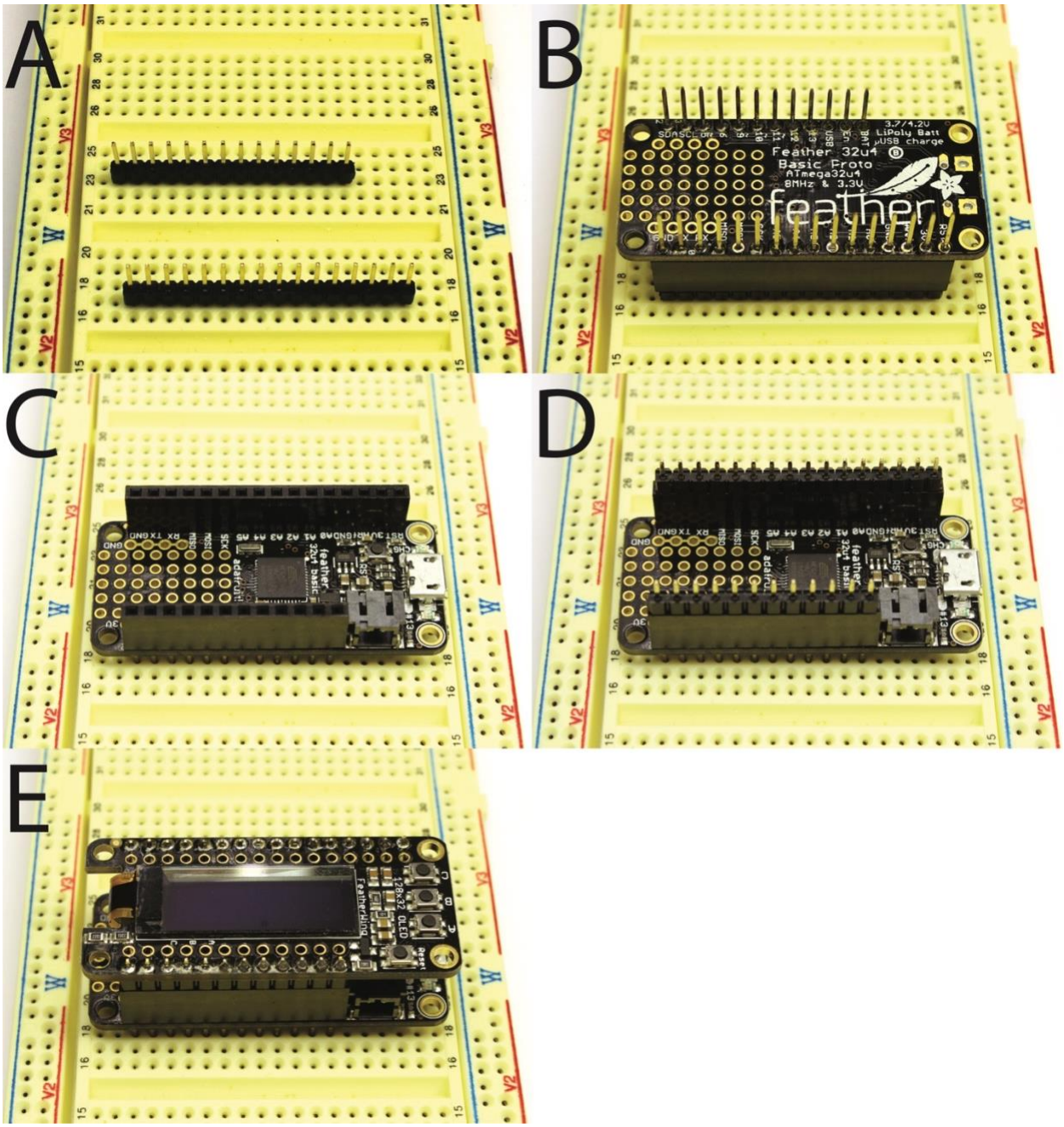

Figure 3.1 Soldering header strips.

(A) Nonstacking headers inserted into a solderless breadboard serving as a base for soldering. (B) Stacking headers soldered into place on the Feather board. (C) Stacking headers and Feather board flipped so that the male ends of the stacking headers can be placed into the solderless breadboard. (D) Long ends of the headers from OLED display placed into female ends of stacking headers attached to the feather board. (E) OLED display placed onto headers and soldered into place.

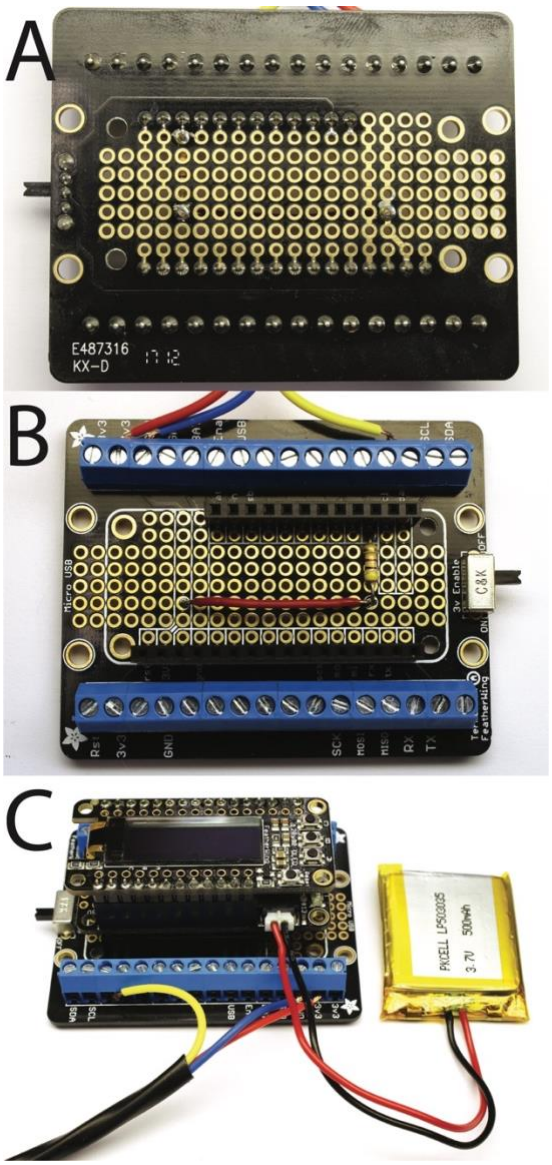

Figure 3.2 Assembling the TADT.

(A,B) Top (A) and bottom (B) view of terminal breakout board with stacking headers and pull-up resistor soldered into place. (C) Completed device with Feather board attached to terminal breakout board and LiPo battery.

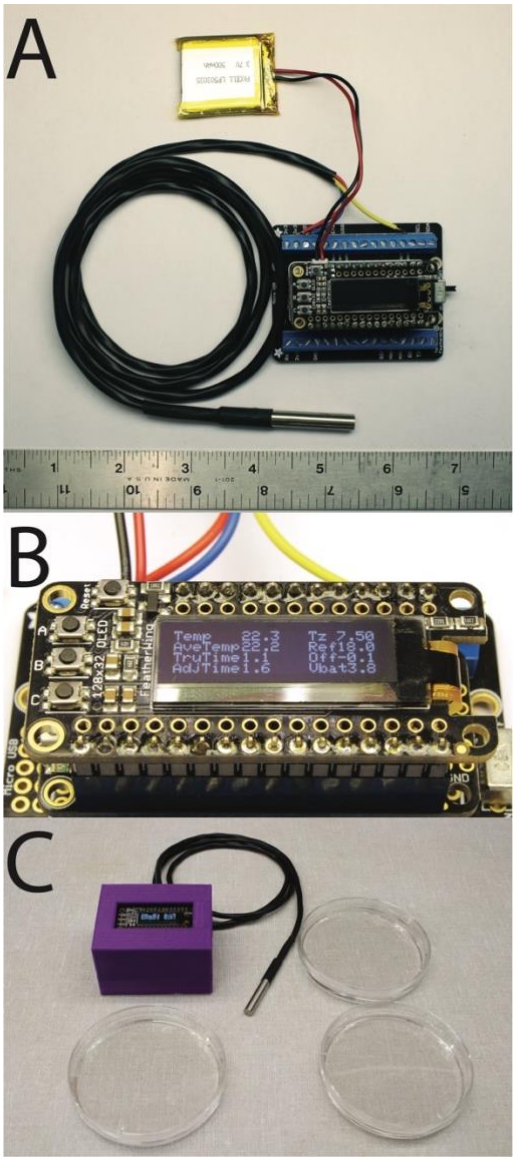

Figure 3.3 Assembled TADT device.

(A) TADT device with temperature probe and LiPo battery connected. Ruler for scale is in inches. (B) Device display when powered on. (C) TADT in use with temperature probe in close proximity to 90 mm embryo culture dishes.

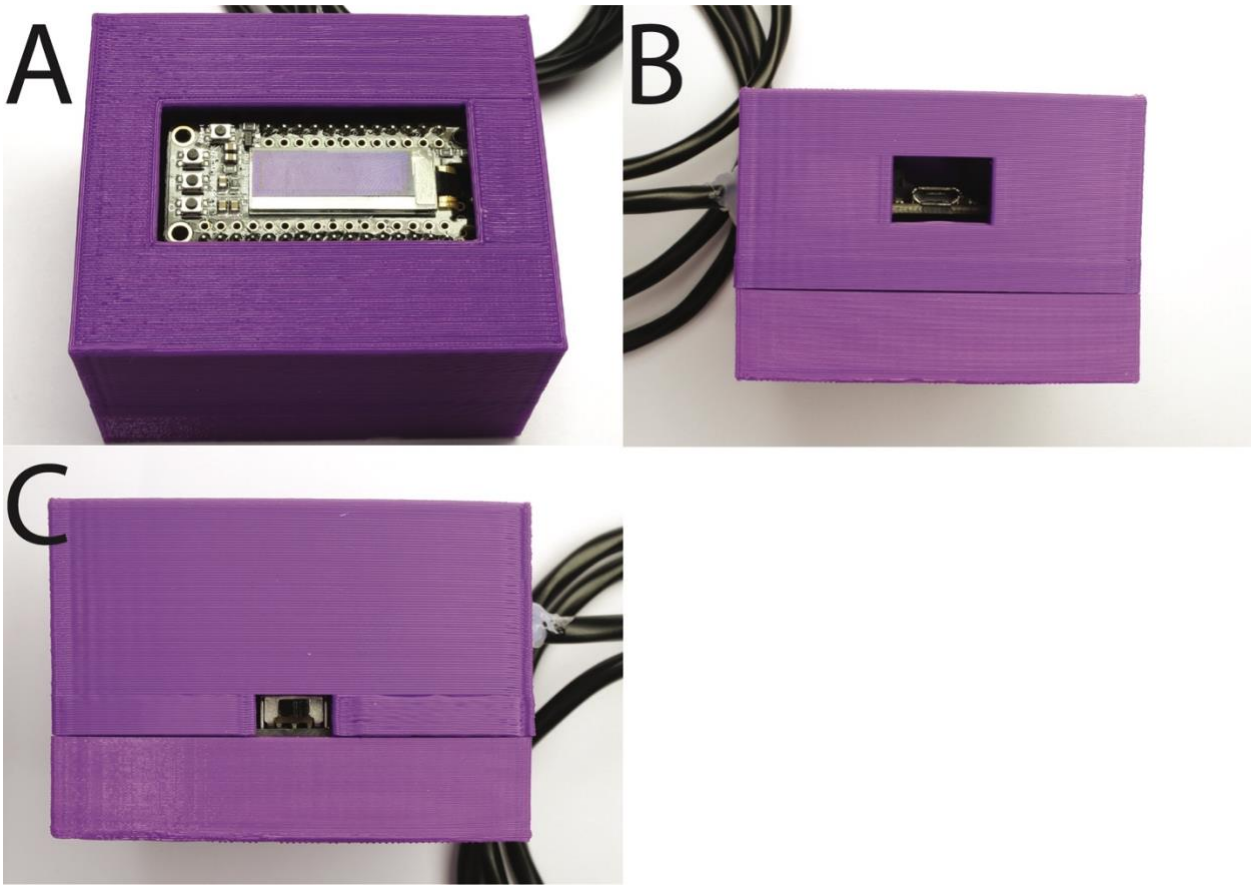

Figure 3.4 3D printed enclosure.

(A) Display opening. (B) Micro-USB port opening. Temperature probe pass-through can be seen on the left side. (C) Power switch opening. Temperature probe pass-through can be seen on the right side.

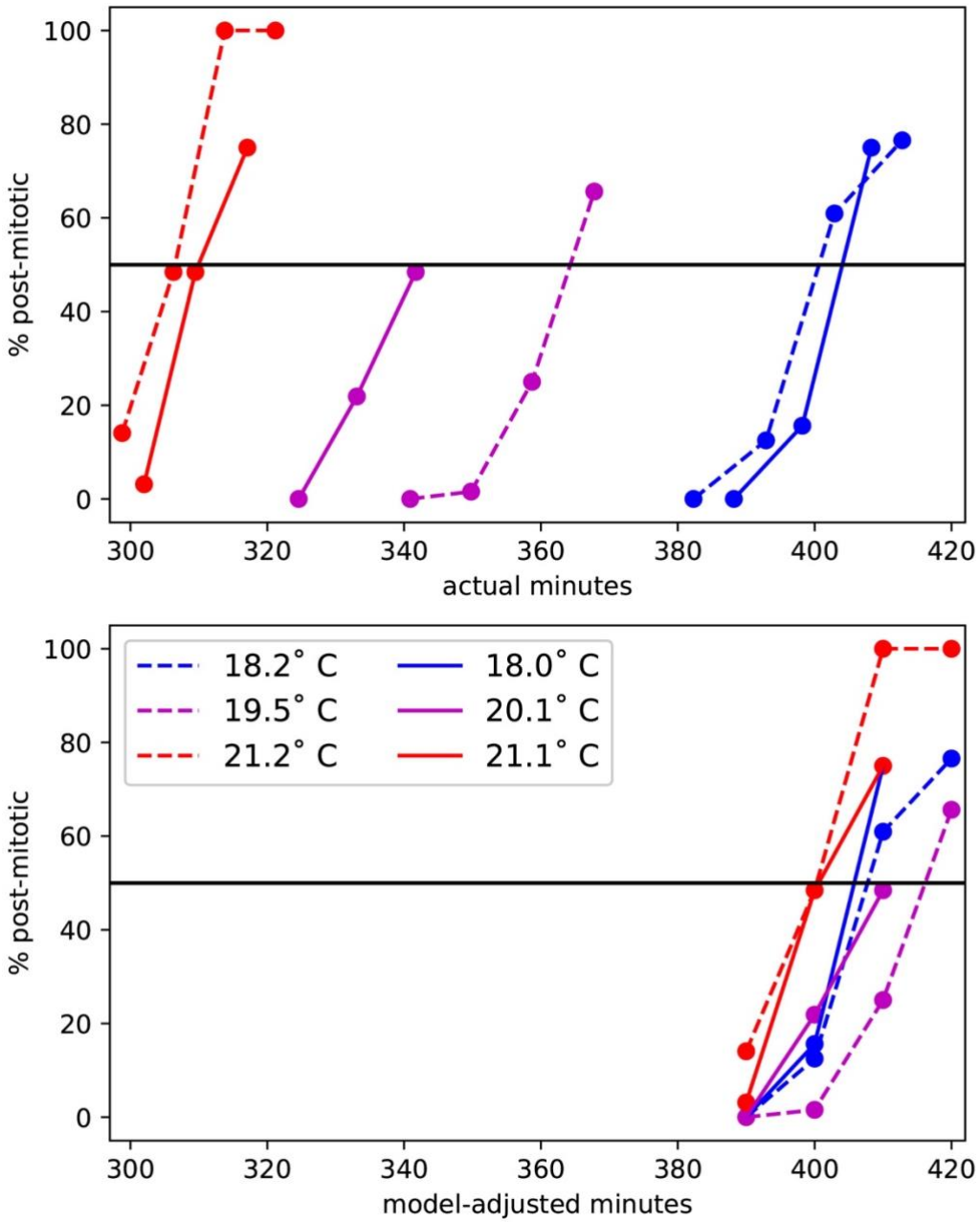

Figure 3.5 Biological validation.

Timing of the final primary notochord cell division (percent of cells that have completed mitosis) for Ciona embryos grown at different temperatures. The top panel shows actual time. The bottom panel shows model-adjusted time using TADT devices with parameters T0=7.5°C and Tref=18°C. The two separate biological replicates are represented with solid versus dashed lines. The legend applies to both panels.

Chapter 4 - Iterative and Complex Asymmetric Divisions Control Cell Volume Differences in Ciona Notochord Tapering

Abstract

The notochord of the invertebrate chordate *Ciona* forms a tapered rod at tailbud stages consisting of only 40 cylindrical cells in a single-file column. This tapered shape involves differences in notochord cell volume along the anterior-posterior axis. Here, we quantify sibling cell volume asymmetry throughout the developing notochord and find that there are distinctive patterns of unequal cleavage in all 4 bilateral pairs of A-line primary notochord founder cells and also in the B-line-derived secondary notochord founder cells. A quantitative model confirms that the observed patterns of unequal cleavage are sufficient to explain all the anterior-posterior variation in notochord cell volume. Many examples are known of cells that divide asymmetrically to give daughter cells of different size and fate. Here, by contrast, a series of subtle but iterative and finely patterned asymmetric divisions controls the shape of an entire organ. Quantitative 3D analysis of cell shape and spindle positioning allows us to infer multiple cellular mechanisms driving these unequal cleavages, including polarized displacements of the mitotic spindle, contributions from the shape of the mother cell, and late changes occurring between anaphase and abscission that potentially involve differential cortical contractility. We infer differential use of these mechanisms between different notochord blastomeres and also between different rounds of cell division. These results demonstrate a new role for asymmetric division in directly shaping a developing organ and point toward complex underlying mechanisms.

Introduction

The invertebrate chordate *Ciona* has unique advantages as a model organism for developing a quantitative understanding of organogenesis. The *Ciona* embryo has a simple but stereotypically chordate body plan that is small enough for in toto quantitative confocal microscopy (M. Veeman & Reeves, 2015). The *Ciona* notochord forms a tapered rod at tailbud stages consisting of only 40 cylindrical cells in a single-file column. This tapered shape involves differences in notochord cell volume along the anterior-posterior axis (M. T. Veeman & Smith, 2013). At the initial gastrula stage, the *Ciona* notochord primordium consists of an arc of 8 bilateral pairs of primary notochord cells (A8.5, A8.6, A8.13, and A8.14) and a discontiguous pair of secondary notochord cells (B8.6). The primary cells undergo a second-last division early in gastrulation and then a final division late in gastrulation. The secondary cell on each side comes into contact with the primary cells during gastrulation as the intervening cell moves out of the way. The secondary cells also go through two rounds of division that are slightly delayed compared to the primary cells (Figures 1A and S1A). In the *Ciona* blastomere naming system originated by Conklin (Conklin, 1905), the letter indicates the quadrant of origin in the 8-cell embryo (A, anterior vegetal; B, posterior vegetal), the first number indicates the cell cycle since fertilization, and the second number provides a unique code for each blastomere that indicates its mother cell. A8.5, for example, divides to give A9.10 and A9.9, whereas B8.6 divides to give B9.12 and B9.11. At early stages, the more vegetal daughter receives the lower number (Conklin, 1905), and at later stages, the more posterior daughter receives the lower number (Cole & Meinertzhagen, 2004). The embryo is bilaterally symmetrical, with each blastomere having left and right equivalents.

The post-mitotic notochord forms a flat plate of cells that converge and extend into a single-file column by mediolateral intercalation (Munro & Odell, 2002) (Figures 4.1A and A.1A). There is considerable stochasticity in the precise order of cell intercalation, but AP position in the intercalated notochord broadly reflects AP position in the early notochord plate (Carlson, Reeves, & Veeman, 2015). The secondary cells are more stereotyped in their intercalation patterns and give rise to the posterior-most 8 cells at the tip of the tail.

We previously showed that cell volume differences existing prior to intercalation help to establish the notochord's tapered shape and that there are characteristic volume differences between specific pairs of sibling cells, suggesting a potential role for unequal cell division (M. T. Veeman & Smith, 2013). At the time, however, we could only identify sibling relationships for a modest subset of notochord cells, and we only examined a single round of division. We also did not test the alternate, but not mutually exclusive, hypothesis that differences in cell volume might involve locally patterned cell shrinking or swelling. Here, we quantify the role of unequal cell division for all notochord cells in their two final cell cycles and also compare cell volumes over time to test for alternate mechanisms. We find that the cell volume differences along the anterior-posterior axis of the *Ciona* notochord can be fully explained by relatively subtle patterns of asymmetric division that act iteratively over multiple cell cycles to have a cumulatively important effect on organ shape. These subtle and iterative unequal cleavages that occur without obvious segregation of cell fate appear quite different than the canonical models of asymmetric division, such as *Drosophila* neuroblasts and *C. elegans* first cleavage (Homem & Knoblich, 2012; Pacquelet, 2017).

A detailed 3D analysis of mid-to-late anaphase spindle positioning in the context of 3D cell shape supports the idea that these unequal cleavages involve multiple underlying

mechanisms that vary from blastomere to blastomere. These inferred mechanisms include the polarized displacement of the mitotic spindle, which has been observed in many asymmetrically dividing cells. We also find evidence, however, for a role of mother cell shape when it is wedge-like perpendicular to the cleavage plane and for changes in sibling cell volumes very late in division that potentially involve differential cortical contractility.

Results

Iterative Unequal Cleavages Control Notochord Cell Volume Differences

Our previous study of notochord tapering used *Ciona savignyi* and not the more widely studied *Ciona robusta* that we use here. To confirm that notochord tapering is similar between the two species and better understand cell volume as a function of anterior-posterior (AP) position in the intercalated notochord, we imaged a large number of *Ciona robusta* embryos expressing a notochord-specific membrane-targeted GFP transgene by 3D confocal microscopy and quantified notochord cell volumes (Figures A.1B and A.1C). Although there is considerable embryo-to-embryo variation in the precise sequence of cell volumes, it is clear that notochord cell volumes become progressively smaller toward the anterior and posterior tips in both the primary and secondary notochord lineages (Figures 4.1B and 4.1C).

To map asymmetric division across the entire notochord primordium, we used the mosaic expression of electroporated transgenes to identify clonal groups of cells (Figures 4.2A and 4.2C) and directly compared sibling cell volumes. *Ciona* development is sufficiently stereotyped that we could reliably fix embryos for imaging within 5 min or less of each division. In the second-last division, the medial primary cells A8.5 and A8.6 have a statistically significant tendency to divide to give smaller anterior daughters, whereas the lateral primary cells A8.13 and A8.14 and the secondary notochord cells tend to divide to give smaller posterior daughters (Figure 4.2B). The notochord cells flip over during gastrulation as they are dividing, with the originally vegetal-posterior side becoming anterior and the originally animal-anterior side becoming posterior. For simplicity, we define anterior and posterior daughter cells at this time point and assign blastomere names with respect to the position at the end of gastrulation. In the final division, the anterior daughters of A8.5 and A8.6 again tend to divide asymmetrically to

give smaller anterior daughters, whereas the posterior daughters of A8.13 and A8.14 tend to give smaller posterior daughters (Figure 4.2D). The secondary cell divisions are particularly asymmetric. In the second-last division, the posterior daughter is roughly half the size of the anterior daughter (Figure 4.2B). In the final division, both secondary cells divide asymmetrically again to give smaller posterior daughters (Figure 4.2D). The cumulative effect of these successive rounds of unequal cleavage is to make cells near the anterior and posterior ends of the notochord primordium progressively smaller in volume (Figure 4.2E). We previously mapped the statistical tendency for the different notochord blastomeres to intercalate to specific anterior-posterior positions (Carlson et al., 2015) and have extended those observations here with a larger sample size. Despite considerable embryo-to-embryo variation in the precise order of mediolateral intercalation, the spatial relationships between notochord cells are largely preserved as the notochord converges and extends (Figure 4.2F). The result is that cells nearer the anterior and posterior tips of the intercalated notochord are increasingly more likely to have been the smaller daughter in multiple rounds of division (Figure 4.2G).

Asymmetric Division Is Sufficient to Explain Notochord Taper

To test whether regionalized cell volume changes were potentially contributing in parallel, we also compared sibling cell volume ratios for equivalent cells both immediately after each division and much later after intercalation. Immediately after division, we can unambiguously identify all notochord cells. For the late, post-intercalation time point, we can identify primary notochord cells within two-cell equivalence groups based on our previous observation that embryos with mosaic expression in just 4 cells represent two distinct clonal populations: an anterior-biased population derived from A8.5 and A8.6 and a posterior-biased population derived from A8.13 and A8.14 (Figures A.2A and A.2B). We cannot reliably

distinguish between clones derived from A8.5 versus A8.6 or A8.13 versus A8.14, so the primary notochord volume ratio over time comparisons were made within these 2-cell equivalence groups. Secondary notochord intercalation is more stereotyped (Carlson et al., 2015) such that blastomere identity is unambiguous in 4-cell clones after intercalation. We found that sibling cell volume ratios generally do not change over time. For the few instances that we did find a significant change in sibling cell volume ratios over time, these were typically small in magnitude or the change was in the opposite direction of notochord taper (Figures 4.3A–4.3C). This led us to conclude that patterned cell volume changes are not a major driver of tapering.

To confirm whether the observed patterns of unequal cell division are sufficient to explain the full diversity of cell volumes along the AP axis, we developed a statistical model. We first predicted the mean volume of each of the post-mitotic notochord cells by taking the mean volume of each notochord founder cell (Figure A.2C) and multiplying them out by the mean asymmetry coefficients of each round of division (Figures 4.2B and 4.2D). We then predicted the mean volume of each AP position in the intercalated notochord by summing the product of the average volume for each cell calculated above with its probability of contributing to that AP position (Figure A.2D; complete details in Methods). The computationally predicted volume-AP position curves are closely matched to the experimental data, indicating that our current understanding of notochord cell asymmetric division tendencies and intercalation patterns is sufficient to explain all of the cell volume differences along the AP axis of the intercalated notochord, at least at the level of population means (Figure 4.3D).

Distinct Modes of Mitotic Spindle Orientation

To understand how the volume asymmetries in notochord cell divisions are generated, we first analyzed the orientation and position of the mitotic spindle. Hertwig's rule suggests that cells typically orient their spindle along their longest spatial dimension (Hertwig, 1884). A common exception to this involves epithelial cells, which often orient their spindle parallel to apical junctional complexes. Within that plane, however, epithelial cells often orient the spindle parallel to the long axis and perpendicular to the short axis of the apical surface (Ragkousi & Gibson, 2014). Other tissues will orient the spindle with respect to an anatomical axis in the embryo as a manifestation of planar polarity (Gho & Schweisguth, 1998; Gong, Mo, & Fraser, 2004; Schlesinger, Shelton, Maloof, Meneghini, & Bowerman, 1999).

To quantify spindle orientation in the *Ciona* notochord, we imaged notochord cells in mid-to-late anaphase, segmented the cell membranes, and marked the two spindle poles for each dividing cell. We used principal-component analysis (PCA) to identify the three orthogonal vectors representing the major (longest), semimajor, and minor (shortest) axis of each cell. We also manually defined the AP axis of each embryo.

Principal components help to characterize cell shape but do not incorporate any information about tissue architecture. Before gastrulation, the notochord cells have a distinct apical surface on the surface of the embryo. The apical plane of each cell was defined by computationally extracting an apical belt at the intersection of lateral and apical cell surfaces and finding the plane of best fit to that belt. We defined a new coordinate system consisting of three orthogonal vectors, C1 through C3, that incorporates aspects of both cell and tissue geometry. C1 is the normal vector of the apical plane and thus approximates the apical-basal axis. C2

represents the cell's longest axis orthogonal to C1, whereas C3 is the short axis orthogonal to C1 and C2 (Figures 4.4A–4.4D).

The primary notochord cells form a curved row around the archenteron during the second-last division, with neural plate cells to the anterior and endoderm to the posterior (Figures 4.4A and 4.4B). For medial primary notochord cells, C2 is roughly aligned with the AP axis and C3 with the mediolateral axis, but progressively more lateral notochord cells are progressively more angled with respect to the AP axis. For primary notochord cells at this stage, C2 can also be thought of as representing an axis based on notochord cell contacts, with neural plate on one side and endoderm on the other.

To better assess stereotypy and variation in *Ciona* notochord cell shape, we transformed our segmented cell outlines and spindle pole coordinates into the C1,C2,C3 coordinate system; aligned them at the centroid of the cell; and overlaid the data from each cell analyzed. We found that the shape of each blastomere is sufficiently stereotyped that these eigen-cell visualizations provide a consistent and realistic view of typical notochord cell shape (Figures 4.4E, 4.4F, and A.3). A characteristic feature of notochord cells in the second-last division is that many are narrower on the end in contact with the invaginating endoderm cells. These mid-late anaphase cells also show relatively little mitotic rounding.

In the primary notochord second-last division, we find that the spindle tends to be well aligned with the apical surface, but not well aligned with the AP axis (Figure 4.4G). It is particularly well aligned with C2 (Figure A.4A), which represents the longest dimension of the cell parallel to the apical surface. The small deviations seen from C2 are almost entirely in the apical-basal dimension, with the lateral deviation from C2 being very small (Figure 4G; see

STAR Methods for full details). Of note, C2 is also strongly aligned with the longest axis of the apical surface (Figure A.4B).

This orientation of the spindle in the primary notochord cells during the second-last division is akin to the common epithelial modification of Hertwig's rule. In the final division, however, the primary notochord cell spindles are still aligned parallel to the apical surface but are now more aligned with respect to the embryo's AP axis and less aligned to the C2 long axis (Figures 4.4H and A.4C). This is most apparent in the cells where C2 is not parallel to the AP axis (Figures 4.4C and 4.4C'; note red asterisk in Figure 4.4C), which occurs most often in the daughters of A8.13 and A8.14 (Figure A.3B).

The secondary notochord cells differ from the primary notochord cells in the second-last division. Here, the secondary cells tend to align their spindles perpendicular to both C2 (Figure A.4A) and the apical surface (Figure 4.4G). Because the spindle is perpendicular to the apical surface, its lateral deviation from C2 does not meaningfully represent its orientation and therefore is not shown. In contrast, secondary cells respond similarly to primary cells in the final division and orient their spindles parallel to both the apical surface and to the embryo's AP axis (Figures 4.4H and A.4C). In summary, we find that notochord cells orient their spindles differently both between divisions within a lineage and between lineages within a round of division.

Spindle Displacement

The best-characterized mechanism for unequal cleavage involves a displacement of the mitotic spindle away from the cell's center of mass, typically via cortical polarity cues that lead to an imbalance of force generators acting on the astral microtubules of the two spindle poles (Kotak & Gönczy, 2013; Sallé et al., 2019). Having identified several distinct modes of spindle

orientation in the notochord, we next quantified whether the spindle was consistently displaced in any of these divisions. Biophysical models of spindle position suggest that length-dependent astral forces center the spindle at the cell centroid (Grill & Hyman, 2005; Minc, Burgess, & Chang, 2011; Wühr, Tan, Parker, Detrich, & Mitchison, 2010). Cortical force generators enriched at apical junctional complexes are thought to be important in orienting the spindle in many epithelia, but spindle positioning is generally believed to involve both cortical and cytoplasmic force generators (De Simone, Spahr, Busso, & Gönczy, 2018; Lacroix et al., 2018; Wühr et al., 2010). Dumollard and colleagues found that the mitotic spindle is displaced toward the apical surface in early cleavage-stage ascidian embryos (Dumollard et al., 2017) and that the spindle is well aligned with the long axis of a 2D representation of the apical surface. Most of what is known about spindle positioning involves 2D approximations of an inherently 3D process, so the ‘‘default’’ position in 3D of a centered spindle is not clear. The details are likely to be highly context dependent, given differences in cell size, spindle size, and graded epithelial-mesenchymal status.

If notochord cell spindle positioning is predominantly guided by the shape of the cell overall, we would expect the spindle midpoint to be near the cell centroid. If spindle positioning is predominantly guided by apical junctional complexes, we would expect it to be near the centroid of those complexes. We measured the distance of the spindle midpoint from both the cell centroid and the centroid of an apical belt extracted at the intersection of lateral and apical surfaces. We found that the spindle is much closer to the cell centroid than the apical belt centroid (Figures 4.4I and A.4D) and not consistently apically or basally displaced (Figures 4.4J and A.4E). This is also apparent in the eigen-cell projections (Figure A.3).

Accordingly, we used the cell centroid as the default position to identify potential spindle displacement. We projected the cell centroid onto the observed spindle orientation vector to specifically measure the displacement along the spindle orientation axis that would be expected to alter the cleavage plane. We found that many of the cells that divide asymmetrically have spindles that are displaced away from the cell centroid toward the future smaller daughter cell (Figure 4.4K). The main exception was the medial primary cells in the second-last division, which divide to give smaller anterior daughters but show no statistically significant spindle displacement.

Alternate Mechanisms of Unequal Cleavage

Polarized spindle displacement is the best understood mechanism of unequal cleavage, but there are other potential mechanisms. In both *Drosophila* neuroblasts and *C. elegans* Q neurons, polarized differences in cortical tension during cytokinesis contribute to daughter cell volume asymmetry independently of spindle displacement (Ou, Stuurman, D'Ambrosio, & Vale, 2010; Pham et al., 2019). Mother cell shape has important effects on mitotic spindle orientation (Bosveld et al., 2016; Hertwig, 1884; Minc et al., 2011), and an asymmetrically shaped mother cell could also potentially lead to unequal cleavage, even with a normally centered spindle. The simplest example would be a cell shaped like a cone or a triangular prism, where it is wedge-shaped parallel to its longest axis. This would result in it being wedge-shaped perpendicular to the future cleavage plane. Somewhat unintuitively, a plane through the centroid oriented in that way does not cut the shape into two pieces of equal volume (Figure A.5). Wedge-shaped mother cells could thus potentially give rise to daughters of unequal volume without needing to invoke any form of polarized spindle displacement (Figures 4.5A–4.5A'' and A.5). Viewing our

transformed eigen-cells (Figure A.3) perpendicular to the future cleavage plane, it is possible to identify varying degrees of ‘‘wedginess’’ in the different lineages.

To distinguish between these mechanisms, we developed a computational framework based on analyzing the actual position and orientation of the mitotic spindle during mid-to-late anaphase as compared to the predicted position and orientation (Figures 4.5B and 4.5B’; full details in Methods). The contribution from mother cell shape was inferred by computationally splitting the anaphase cell volume perpendicular to the midpoint of a hypothetical spindle positioned at the cell centroid and oriented in the direction of the observed spindle. The contribution from spindle displacement was inferred by subtracting the contribution from mother cell shape from the inequality predicted by the actual position and orientation of the spindle. The contribution from post-anaphase mechanisms was inferred by subtracting the inequality predicted by the actual orientation and position of the spindle from the mean observed inequality of that blastomere as quantified after cytokinesis.

This analysis revealed that these distinct mechanisms are likely to contribute differentially in different blastomeres and across the different divisions (Figures 4.5C–4.5G). Mother cell shape is inferred to be a major driver of the asymmetries observed in A8.5 and B8.6 but appears to contribute in an opposite direction in other blastomeres. Spindle displacement is inferred to be a major driver of volume asymmetries in the lateral primary cells in the second-last division, all primary cells in the final division, and in all secondary divisions. Post-anaphase effects are inferred to be the major driver of asymmetry in A8.6 and enhance asymmetry in A8.14 and most secondary divisions but decrease the asymmetry in A9.25 and A9.27. Although it is possible that our partitioning of distinct mechanisms based on a computational analysis of cell geometry is confounded in some way, these results support the idea that multiple cellular

mechanisms deployed in different ways in different blastomeres contribute to the complex patterns of unequal cleavage observed.

Discussion

Asymmetric Division as a Direct Morphogenetic Mechanism Asymmetric

Asymmetric divisions are common in developing embryos, but the canonical models, such as *C. elegans* first cleavage and fly neuroblasts, all involve highly polarized cells that divide to give daughters of considerably different size and completely different fate (Gönczy, 2008; Homem & Knoblich, 2012; Neumüller & Knoblich, 2009; Ou et al., 2010; Pacquelet, 2017; Pillitteri, Guo, & Dong, 2016; Smith, Azzam, & Hinck, 2017). The asymmetric divisions in the *Ciona* notochord, however, are relatively subtle and do not involve any obvious segregation of cell identity. Instead, they act iteratively over two successive cell cycles to control the shape of an entire chordate organ. This only became apparent here through the quantification of sibling cell volume differences across the entire developing notochord in a large sample of 1,381 sibling cell pairs, so it is likely that similar mechanisms are important in other contexts. We speculate that direct effects of unequal cleavage upon morphogenesis may be particularly important in species, such as *Ciona*, with small embryos and relatively stereotyped development.

The *Ciona* notochord is derived from two distinct lineages that diverge at the 8-cell stage and undergo what appear to be fundamentally different programs of unequal division. That said, the transition between the posterior-most primary cells and anterior-most secondary cells tends to be very smooth, without an obvious discontinuity in cell volumes. That implies that the patterns of unequal cleavage in A-line and B-line notochord have evolved in concert to help provide a smoothly tapering tail tip. Ascidian cell lineages and embryonic architecture are highly conserved across large evolutionary distances (Lemaire, 2009). The potential need for tissues derived from multiple lineages to match in volume could be an important constraint on evolutionary changes in unequal cleavage.

Spindle Orientation

In many notochord blastomeres, the spindle orients in a highly predictable way parallel to the long axis of the apical surface. The long axis of the apical surface is highly congruent with the longest axis of the cell in 3D projected onto the apical surface, and the spindle midpoint is much closer to the cell centroid than to the centroid of the apical junctions, so this is consistent with spindle orientation being guided by force generators throughout the cell and not only at apical junctional complexes.

We observed differences in spindle orientation in the primary notochord cells between the second-last and final divisions. In the second-last division, cells tended to divide according to the epithelial long-axis rule, regardless of their orientation with respect to the embryo's AP axis. In the final division, the spindle showed a new tendency to orient parallel to the AP axis, even in the cells where the AP axis and C2 were not aligned. It remains to be determined whether this plane-polarized phenomenon involves the noncanonical Wnt/PCP pathway activity or some other mechanism. Secondary notochord cells differ even more profoundly in the second-last division, with the spindle typically being aligned orthogonal to the apical surface and not parallel, as seen in the primary notochord. This adds to the list of behavioral and transcriptional differences that have been observed between primary and secondary notochord cells (Cao et al., 2019; Carlson et al., 2015; Harder, Reeves, Byers, Santiago, & Veeman, 2018; Jiang, Munro, & Smith, 2005).

Mother Cell Shape

We find there are polarized displacements of the mitotic spindle in many unequally dividing *Ciona* notochord cells, similar to what is seen in many unequally dividing cell types (Morin & Bellaïche, 2011). Our 3D analysis of spindle position and cell shape in a large sample of 560 dividing notochord cells supports there being important roles, however, for other

mechanisms, including contributions due to the shape of the mother cell as well as very late effects occurring between anaphase and abscission. Mother cell shape has a well-established role in mitotic spindle orientation but has not been widely contemplated as a driver of unequal cleavage. Cell types vary in the extent to which they round up during mitosis, and there is also evidence that interphase cell shape can influence spindle positioning, even in cells with extensive mitotic rounding (Bosveld et al., 2016). Most *Ciona* notochord cells show relatively little mitotic rounding, so a mother cell that is at all wedge-shaped in the direction of spindle orientation should lead to effects on daughter cell volume ratios. In the second-last division, the notochord cells tend to be slightly wedge shaped, with a narrower end facing the archenteron that gives rise to the anterior daughter after the cells invert during gastrulation. Our analysis of cell and spindle geometry implicates cell shape as a major driver of unequal cleavage in the medial A8.5 cells but as a counteracting factor to the asymmetry driven by spindle displacement in the lateral primary notochord cells that divide to give smaller posterior daughters. There are also significant displacements of the spindle in some cells, such as A9.11 and A9.28, that appear to be counterbalanced by other factors to give a relatively symmetric division. It remains to be determined whether the spindle displacements in different notochord blastomeres make use of conventional mechanisms based on biased distributions of cortical force generators acting on astral microtubules or whether novel mechanisms might be involved.

Post-anaphase Effects

We also see significant differences in certain cells between the asymmetry predicted by cell shape and spindle position as compared to the mean asymmetry of that blastomere after it actually divides. This could potentially reflect very late displacement of the spindle, but the distinct trends seen in different cells suggest that it may represent an independent mechanism.

We speculate that this is likely to involve local differences in cortical contractility. Specific notochord blastomeres vary in the contacts they make with other notochord cells, other cell types, and the archenteron lumen. Differential cell contacts are known to influence local cortical tension in many contexts (Chan, Chavadimane Shivakumar, Clément, Laugier, & Lenne, 2017; Priya & Yap, 2015). The cell poles relax during cytokinesis (Kunda, Pelling, Liu, & Baum, 2008), but unless there are unknown mechanisms that perfectly balance polar relaxation, local differences in contractility would be expected to influence daughter cell volume ratios, as has already been observed in some highly polarized cell types (Ou et al., 2010; Pham et al., 2019). Spindle pole-derived signals have been shown to influence polar membrane expansion in cultured cells and help to equilibrate daughter cell volumes (Kiyomitsu & Cheeseman, 2013), but the precision and ubiquity of this mechanism is not clear. An important question for the future is whether there is any feedback or dynamic interplay between the multiple mechanisms influencing volume asymmetry during cell division. Differential cortical tension, for example, could potentially have complex effects on both mother cell shape and differential polar relaxation.

Diversity of Cellular Mechanisms Driving Unequal Cleavage

Differences in gene expression and cell behavior have previously been described between primary and secondary notochord cells (Harder et al., 2018; Hudson & Yasuo, 2006), but the only well-established differences between primary notochord cells involve differences in AP fate after intercalation that can be explained simply by the cells' positions in the early notochord primordium (Carlson et al., 2015). Here, we find that A8.5, A8.6, A8.13, A8.14, and their descendants vary extensively in their patterns of unequal cleavage and the inferred underlying cellular mechanisms. It remains to be determined whether these differences reflect the

architecture of the embryo and the precise contacts made by each cell or whether different primary notochord cells have cryptic but distinct transcriptional identities. More broadly, it will be important to determine to what extent these unequal cleavages involve specific cell-cell signals or cell-intrinsic programs versus emergent properties of the architecture and biomechanics of the entire tissue. The small but surprisingly complex *Ciona* notochord provides a new model for the integrative and quantitative analysis of the cellular mechanisms and developmental functions of unequal cell division.

Acknowledgements

We gratefully acknowledge support from the National Science Foundation (IOS 1456555 to M.V.), the Kansas State University College of Veterinary Medicine Confocal Core, and the Kansas State University Beocat high-performance computing cluster.

Materials and Methods

Experimental Model and Subject Details

Wild caught *Ciona robusta* (formerly *Ciona intestinalis* type A) were purchased from Marine Research and Educational Products (MREP, San Diego). As invertebrate chordates, animal care approval was not needed. Recombinant DNA experiments were approved by the KSU Institutional Biosafety Committee. Animals were housed in a recirculating artificial seawater aquarium at 18˚C under constant light until experimental use.

Dechorionation and electroporation

Dechorionation was performed according to standard protocols (M. T. Veeman, Chiba, & Smith, 2011). Eggs and sperm were collected from 3 adults per experiment. Eggs were washed, inseminated, and left to fertilize for 5 minutes. The fertilized eggs were then placed in a dechorionation solution (0.12 g Sodium Thioglycolate, 9mL Artificial Sea Water (ASW), 32 µL 10M NaOH, 1mL 0.5% Protease E (Strep. griseus)) and agitated gently by pipetting until the follicle cells and chorion were removed. The fertilized, dechorionated eggs were then washed 3 times in 0.1% BSA in ASW and once in ASW before electroporation. 480 µL 0.77M mannitol and 20 µL plasmid DNA were combined in an electroporation cuvette to which 300 µL of fertilized, dechorionated eggs in ASW were added. The cuvette was shocked in a Bio-Rad Gene Pulser XCell using the time constant protocol with settings of 50 mV, a time constant of 17 ms, and a 4mm cuvette gap. Electroporations with a capacitance less than 750 µFd were discarded. Approximately 12.5 µg of the plasmid containing the Bra > GFP-GPI transgene and 12.5 µg of the plasmid containing the Bra > H2B-HA transgene was electroporated for imaging after the final division where 4-cell clones were desired. Electroporations for imaging during or immediately after the second-last division used 30 µg of each plasmid.

Staging, fixing, and staining

Electroporated embryos were placed in an incubator at ~19.5˚C and tracked using the Temperature Adjusted Developmental Timer which allows us to account for temperature fluctuations that affect the rate at which *Ciona* develop and helps in staging embryos identically between experiments (Winkley & Veeman, 2018). We found that the second-last division took place ~330 adjusted minutes for the 1˚ lineage with the 2˚ lineage shortly following. The final division took place ~425 adjusted minutes for the 1˚ lineage and ~480 adjusted minutes for the 2˚ lineage. We fixed a time series of embryos with spacing of 8 adjusted minutes (~5-6 real minutes) centered around the normal time of division for every experiment and imaged the first time point immediately after division was complete to ensure we analyzed cells as soon after cytokinesis as possible. At the time of collection, embryos were collected in ~50 µl of ASW and transferred into 1mL of 4% PFA in ASW. Embryos were fixed overnight at 4˚C. Washes were performed at RT in PBST with gentle agitation on an orbital shaker. Embryos were stained for transgenes using anti-GFP (1:1000) and anti-HA (1:750) primary antibodies for one hour at RT with gentle agitation on an orbital shaker followed by an overnight incubation at 4˚C. Alexa Fluor conjugated secondary antibodies were used at a 1:1000 dilution and were incubated identically to the primary antibodies. Embryos were counterstained using Alexa Fluor conjugated phalloidin at a 1:100 dilution which was included in the secondary antibody solution. Stained embryos were adhered to poly-l-lysine coated coverslips, dehydrated through a rapid isopropanol series and then cleared and mounted in Murray's Clear (BABB).

Imaging

Confocal images were acquired using Zeiss 700 and 880 microscopes. All images were acquired using 40x, 1.3NA oil immersion objectives, 1 Airy unit pinhole size, pixel dimensions of 0.16 microns, and slice spacing of 0.3 microns.

Cloning details

The Bra > GFP-GPI reporter was generated by standard Gateway cloning of pENTR-Kozak-GFP-GPI into pSP72BSSPE-SwaI::RFA (Roure et al., 2007). A 2.2kb Brachyury enhancer was cloned into the plasmid's XhoI/HindIII sites.

Image segmentation

Image segmentation was performed using Python scripts developed in house based on the methods described in Veeman & Smith 2013 (M. T. Veeman & Smith, 2013). Briefly, image volumes were filtered to enhance membrane features using a ''Hessian of the Gaussian last eigenvalue'' filter (Gaussian kernel width of 3 pixels) implemented in the VIGRA package (Kothe, 2000). This filtered image was then segmented in 3D using seeded watershed segmentation from the scikit-image package (van der Walt et al., 2014). We used hand-drawn seeds created interactively in FIJI (Rueden et al., 2017; Schindelin et al., 2012). Seeds were refined until a high-quality segmentation was obtained.

Model of cell volume as a function of AP position

We created a model where the average volume of the cell at position i is predicted by the equation:

$$Volume\ of\ cell\ i$$

$$= \sum_{i} Average\ volume\ of\ founder\ blastomere_{\ i}$$

$$* \ Average\ \%\ of\ total\ volume\ from\ second - last\ division_{\ i}$$

$$* \ Average\ \%\ of\ total\ volume\ from\ final\ division_{\ i}$$

$$* probability\ that\ position\ i\ is\ occupied\ by\ cell\ j$$

Where:

i = {1, 2. 39, 40}

j = {Anterior clones cell 1, Anterior clones cell 2, Anterior clones cell 3, Anterior clones cell 4, Posterior clones cell 1, Posterior clones cell 2, Posterior clones cell 3, Posterior clones cell 4, Secondary clones cell 1, Secondary clones cell 2, Secondary clones cell 3, Secondary clones cell 4}

The average founder blastomere volume was obtained by calculating the volume of each cell in our analysis of spindle position in the second-last division (Figure A.2C). The mean asymmetry of each division was calculated from our analysis of sibling cell volume ratios. The probability of different cells contributing to positions 1-40 in the intercalated notochord is derived from our clonal analysis in (Carlson et al., 2015), expanded here to a larger sample size (Figure A.2D). This used a genetic fate mapping approach based on mosaic transgene expression to identify which blastomeres contribute to what AP positions in the intercalated notochord. However, blastomere identity to position relationships in the primary notochord are resolvable only to a level of two-cell equivalence groups which define distinct anterior and posterior 4-cell clones (Figure A.2A). Anterior clones in the second-last and final division are comprised of A8.5

and A8.6 and their descendants, while the posterior clones in the second-last and final division are comprised of A8.13 and A8.14 and their descendants.

Sibling cell volume ratios over time

To test whether patterned cell shrinking or swelling might be contributing to notochord cell volume differences, we compared sibling cell volume ratios in embryos fixed at multiple time points. We used clonally propagated mosaic transgene expression to identify sibling cells. *Ciona* eggs vary somewhat in size (Gregory & Veeman, 2013) so we compared sibling cell volume ratios and not raw cell volumes to control for batch effects on embryo size. We compared the sibling cell volume ratios resulting from the two rounds of division at three developmental time points: immediately after the second-last division (Hotta stage 12)) (Hotta et al., 2007); immediately after the final division (Hotta stage 13)) (Hotta et al., 2007); and after intercalation was complete (Hotta stage 22)) (Hotta et al., 2007). At the first two time points, the founder blastomere of a given clone is evident from the morphology of the embryo. At the final time point, we can only distinguish for the primary notochord between 'anterior' clones derived from A8.5 and A8.6 and 'posterior' clones derived from A8.13 and A8.14. Accordingly, we aggregated the data from the first two time points to match the equivalence groups resolvable at the final time point. The late post-intercalation stage was based on imaging 4-cell clones in which we know that the first two cells are siblings, the last two cells are siblings, and that these two sibling pairs originated in the second-last division.

To assess the stability over time of the sibling cell volume ratios resulting from the second-last division, we looked for significant differences between three comparison sets for each cell type. The first consisted of the ratio between the anterior and posterior daughters immediately after the second-last division. The second consisted of the ratio between the sum of

the volume of the two most anterior cells and the sum of the volume of the two most posterior cells in a 4-cell clone immediately after the final division, as these two pairs of cells are the descendants of the two daughters produced in the second-last division. The third set was constructed in the same way, but using embryos imaged after the completion of intercalation instead of immediately after the final division.

To assess the stability of the sibling cell volume ratios resulting from the final division, we directly compared sibling cell volume ratios immediately after division and also at the end of intercalation. For 4-cell clones after intercalation, we know that the anteriormost two cells are derived from the anterior daughter in the second-last division and the posteriormost two cells are derived from the posterior daughter in the second-last division. Separate comparisons were made for primary anterior clones (A8.5 and A8.6 derived), primary posterior clones (A8.13 and A8.14 derived) and secondary (B8.6) clones.

Spatial spindle analysis

As our experiments here were all based on fixed and cleared specimens, we restricted our analysis of spindle positioning to cells that were in mid to late anaphase, with well-separated chromosomes, but in which a prominent cleavage furrow had not yet formed. The underlying assumption behind this time window is that polarized displacements of the spindle should already be complete, but effects from differential polar tension or other post-anaphase mechanisms should not yet be apparent. To analyze spindle orientation and position with respect to cell landmarks, the cells were first segmented in 3D using the methods described above. We also segmented the non-notochord cells as a single segment and the outside of the embryo (not-embryo voxels, including the archenteron lumen) to aid in extracting the apical surface of each notochord cell. Spindle poles were marked by hand using the stained chromatin in FIJI. The

major, semimajor, and minor axes of the cell were obtained by principal components analysis (PCA) on the voxel coordinates of each segmented cell using the decomposition module of the scikit-learn package (Pedregosa et al., 2011). The apical belt of each cell was identified in the second-last division by first using mathematical morphology to identify the voxels at the periphery of the apical surface of each cell that were in contact with both the archenteron lumen and the adjacent cells. PCA was then performed on the 3D coordinates of the resulting ring and the first two PCs determined the apical plane. This plane was then translated basally by 4 μm to approximate the depth of apical junctional complexes. We defined the apical belt as the cell membrane voxels between those two planes.

The C1, C2, C3 coordinate system was established by first defining C1 as the normal vector of the apical plane. C2 is the vector orthogonal to C1 that is best aligned with the longest axis of the cell orthogonal to C1. We identified that by first finding the cell principal component most closely aligned to C1. Of the remaining two principal components, we took the one with the largest proportion of variance explained and projected it onto the apical plane to give C2. C3 is then orthogonal to both C1 and C2. In the final division, the blastopore has largely closed and the transient archenteron lumen is no longer distinct. The previously apical side of the notochord plate is now ventral, so we approximated its orientation by segmenting the entire notochord plate and finding the plane described by the first two principal components. We then used this common apical plane to assign the C1, C2, C3 coordinates system in the final division.

To measure the lateral deviation from C2, we projected the spindle vector onto the apical plane, and measured the angle between this projection and the C2 vector.

The AP axis of the embryo was determined by manually defining a midline plane of the embryo and computationally extracting a plane that separated animal and vegetal halves of the

embryo. The intersection of these planes was used as a vector describing the AP axis and measurements between a desired reference vector and the AP vector were obtained by first projecting the reference vector onto the animal/vegetal plane and measuring deviation from this projection and the AP vector.

The cell centroid and apical belt centroid were determined using the center of mass function from the ndimage module of the scipy package (Millman & Aivazis, 2011; Travis E. Oliphant (Brigham Young University), 2007). Angles between the spindle and reference lines/planes were calculated using the geometry module of the sympy package (Meurer et al., 2017).

Eigen-cells

To visualize the shape of late-anaphase notochord cells and understand their spindle orientation in 3-dimensional space, we created eigen-cells for each blastomere during the second-last and final division. For each individual cell analyzed in our measurements the 3D label matrix of that segmented cell was extracted. The label matrix was scaled to create isotropic voxels and the coordinates of all the voxels contained in the cell, the apical membrane (for the second-last division), the cell membrane, the spindle poles, and the spindle midpoint were extracted. All coordinates were shifted so that the cell centroid was at the origin of a 3D coordinate system. The C1 through C3 components were found as described above, and the coordinates were rotated in 3D to align C1,C2 and C3. If necessary, reflections across the x, y, or z axis were performed so that apical surfaces and spindle poles were on the same side of the origin for all cells. Additionally, if necessary, a final reflection across the C3 axis was performed so that all cells were aligned as ‘‘right-sided’’ notochord cells to account for any left-right

chirality in cell shape. All registered volumes for each lineage were then overlaid by sum projection to create 3D eigen-cells for each lineage at each division.

Inferring mechanisms of unequal cleavage

To partition the observed sibling cell volume ratios into distinct effects resulting from mother cell shape, spindle displacement and late post-anaphase mechanisms, we developed a computational approach implemented as Python scripts based on bisecting the mid-late anaphase cell volume with artificial division planes. To assess the role of mother cell shape, we defined an artificial division plane based on a hypothetical spindle positioned at the cell's center of mass and oriented in the same direction as the observed spindle. We calculated the cell volume on either side of this plane to infer the cleavage asymmetry predicted by the shape of the cell even with a spindle perfectly centered at the cell centroid.

To infer the contribution from spindle displacement, we first split each mid-anaphase cell volume with a plane passing through the spindle midpoint and perpendicular to the spindle vector, which gives a predicted cleavage asymmetry based on both the shape of the mother cell and the actual position of the spindle. We inferred the contribution from spindle displacement by subtracting the previously estimated effect of mother cell shape. The effects of spindle displacement and cell shape cannot be perfectly separated from one another, but this provides a reasonable approximation given that the actual displacements observed are quite small.

For each cell, we also calculated the difference between the cleavage asymmetry predicted by the position and orientation of the spindle at mid-late anaphase and the actual mean asymmetry of that particular division as measured shortly after cytokinesis in our sibling cell volume ratio experiments. This gives an estimate of the contribution due to mechanisms at work during very late anaphase/cytokinesis.

Statistical tests and results

All tests for significance were performed as Student's t tests.

Data and code availability

Statistical analyses, scripts, and data are available on the Veeman lab GitHub page (https://github.com/chordmorph) and Mendeley Data. The accession number for the tools and data reported in this paper is Mendeley Data: [https://doi.org/10.17632/2ftgx8whrx.1].

References – Chapter 4

Bosveld, F., Markova, O., Guirao, B., Martin, C., Wang, Z., Pierre, A., … Bellaïche, Y. (2016). Epithelial tricellular junctions act as interphase cell shape sensors to orient mitosis. *Nature*, *530*(7591), 495–498. https://doi.org/10.1038/nature16970

Cao, C., Lemaire, L. A., Wang, W., Yoon, P. H., Choi, Y. A., Parsons, L. R., … Chen, K. (2019). Comprehensive single-cell transcriptome lineages of a proto-vertebrate. *Nature*, *571*(7765), 349–354. https://doi.org/10.1038/s41586-019-1385-y

Carlson, M., Reeves, W., & Veeman, M. (2015). Stochasticity and stereotypy in the Ciona notochord. *Developmental Biology*, *397*(2), 248–256. https://doi.org/10.1016/j.ydbio.2014.11.016

Chan, E. H., Chavadimane Shivakumar, P., Clément, R., Laugier, E., & Lenne, P.-F. (2017). Patterned cortical tension mediated by N-cadherin controls cell geometric order in the Drosophila eye. *ELife*, *6*, 1–27. https://doi.org/10.7554/eLife.22796

Cole, A. G., & Meinertzhagen, I. A. (2004). The central nervous system of the ascidian larva: mitotic history of cells forming the neural tube in late embryonic Ciona intestinalis. *Developmental Biology*, *271*(2), 239–262. https://doi.org/10.1016/j.ydbio.2004.04.001

Conklin, E. G. (1905). *The organization and cell-lineage of the ascidian egg* (Vol. 13).

De Simone, A., Spahr, A., Busso, C., & Gönczy, P. (2018). Uncovering the balance of forces driving microtubule aster migration in C. elegans zygotes. *Nature Communications*, *9*(1), 938. https://doi.org/10.1038/s41467-018-03118-x

Dumollard, R., Minc, N., Salez, G., Aicha, S. Ben, Bekkouche, F., Hebras, C., … McDougall, A. (2017). The invariant cleavage pattern displayed by ascidian embryos depends on spindle positioning along the cell's longest axis in the apical plane and relies on asynchronous cell divisions. *ELife*, *6*, 1–23. https://doi.org/10.7554/eLife.19290

Gho, M., & Schweisguth, F. (1998). Frizzled signalling controls orientation of asymmetric sense organ precursor cell divisions in Drosophila. *Nature*, *393*(6681), 178–181. https://doi.org/10.1038/30265

Gönczy, P. (2008). Mechanisms of asymmetric cell division: flies and worms pave the way. *Nature Reviews. Molecular Cell Biology*, *9*(5), 355–366. https://doi.org/10.1038/nrm2388

Gong, Y., Mo, C., & Fraser, S. E. (2004). Planar cell polarity signalling controls cell division orientation during zebrafish gastrulation. *Nature*, *430*(7000), 689–693. https://doi.org/10.1038/nature02796

Gregory, C., & Veeman, M. (2013). 3D-printed microwell arrays for Ciona microinjection and timelapse imaging. *PloS One*, *8*(12), e82307. https://doi.org/10.1371/journal.pone.0082307

Grill, S. W., & Hyman, A. A. (2005). Spindle positioning by cortical pulling forces. *Developmental*

Cell, *8*(4), 461–465. https://doi.org/10.1016/j.devcel.2005.03.014

Harder, M., Reeves, W., Byers, C., Santiago, M., & Veeman, M. (2018). Multiple inputs into a posterior-specific regulatory network in the Ciona notochord. *Developmental Biology*, *448*(2), 136–146. https://doi.org/10.1016/j.ydbio.2018.09.021

Hertwig, O. (1884). *Das Problem der Befruchtung und der Isotropie des Eies: eine Theorie der Vererbung*. G. Fisher.

Homem, C. C. F., & Knoblich, J. A. (2012). Drosophila neuroblasts: a model for stem cell biology. *Development (Cambridge, England)*, *139*(23), 4297–4310. https://doi.org/10.1242/dev.080515

Hotta, K., Mitsuhara, K., Takahashi, H., Inaba, K., Oka, K., Gojobori, T., & Ikeo, K. (2007). A web-based interactive developmental table for the ascidian Ciona intestinalis, including 3D real-image embryo reconstructions: I. From fertilized egg to hatching larva. *Developmental Dynamics : An Official Publication of the American Association of Anatomists*, *236*(7), 1790–1805. https://doi.org/10.1002/dvdy.21188

Hudson, C., & Yasuo, H. (2006). A signalling relay involving Nodal and Delta ligands acts during secondary notochord induction in Ciona embryos. *Development (Cambridge, England)*, *133*(15), 2855–2864. https://doi.org/10.1242/dev.02466

Jiang, D., Munro, E. M., & Smith, W. C. (2005). Ascidian prickle regulates both mediolateral and anterior-posterior cell polarity of notochord cells. *Current Biology : CB*, *15*(1), 79–85. https://doi.org/10.1016/j.cub.2004.12.041

Kiyomitsu, T., & Cheeseman, I. M. (2013). Cortical dynein and asymmetric membrane elongation coordinately position the spindle in anaphase. *Cell*, *154*(2), 391–402. https://doi.org/10.1016/j.cell.2013.06.010

Kotak, S., & Gönczy, P. (2013). Mechanisms of spindle positioning: cortical force generators in the limelight. *Current Opinion in Cell Biology*, *25*(6), 741–748. https://doi.org/10.1016/j.ceb.2013.07.008

Kothe, U. (2000). *Generische Programmierung fur die Bildverarbeitung*. Books On Demand.

Kunda, P., Pelling, A. E., Liu, T., & Baum, B. (2008). Moesin controls cortical rigidity, cell rounding, and spindle morphogenesis during mitosis. *Current Biology : CB*, *18*(2), 91–101. https://doi.org/10.1016/j.cub.2007.12.051

Lacroix, B., Letort, G., Pitayu, L., Sallé, J., Stefanutti, M., Maton, G., … Dumont, J. (2018). Microtubule Dynamics Scale with Cell Size to Set Spindle Length and Assembly Timing. *Developmental Cell*, *45*(4), 496-511.e6. https://doi.org/10.1016/j.devcel.2018.04.022

Lemaire, P. (2009). Unfolding a chordate developmental program, one cell at a time: invariant cell lineages, short-range inductions and evolutionary plasticity in ascidians. *Developmental Biology*, *332*(1), 48–60. https://doi.org/10.1016/j.ydbio.2009.05.540

Meurer, A., Smith, C. P., Paprocki, M., Čertík, O., Kirpichev, S. B., Rocklin, M., … Scopatz, A. (2017). SymPy: symbolic computing in Python. *PeerJ Computer Science*, *3*, e103. https://doi.org/10.7717/peerj-cs.103

Millman, K. J., & Aivazis, M. (2011). Python for scientists and engineers. *Computing in Science and Engineering*, *13*(2), 9–12. https://doi.org/10.1109/MCSE.2011.36

Minc, N., Burgess, D., & Chang, F. (2011). Influence of cell geometry on division-plane positioning. *Cell*, *144*(3), 414–426. https://doi.org/10.1016/j.cell.2011.01.016

Morin, X., & Bellaïche, Y. (2011). Mitotic spindle orientation in asymmetric and symmetric cell divisions during animal development. *Developmental Cell*, *21*(1), 102–119. https://doi.org/10.1016/j.devcel.2011.06.012

Munro, E. M., & Odell, G. M. (2002). Polarized basolateral cell motility underlies invagination and convergent extension of the ascidian notochord. *Development (Cambridge, England)*, *129*(1), 13–24. Retrieved from http://www.ncbi.nlm.nih.gov/pubmed/11782397

Neumüller, R. A., & Knoblich, J. A. (2009). Dividing cellular asymmetry: asymmetric cell division and its implications for stem cells and cancer. *Genes & Development*, *23*(23), 2675–2699. https://doi.org/10.1101/gad.1850809

Ou, G., Stuurman, N., D'Ambrosio, M., & Vale, R. D. (2010). Polarized myosin produces unequal-size daughters during asymmetric cell division. *Science (New York, N.Y.)*, *330*(6004), 677–680. https://doi.org/10.1126/science.1196112

Pacquelet, A. (2017). Asymmetric Cell Division in the One-Cell C. elegans Embryo: Multiple Steps to Generate Cell Size Asymmetry. *Results and Problems in Cell Differentiation*, *61*, 115–140. https://doi.org/10.1007/978-3-319-53150-2_5

Pedregosa, F., Varoquaux, G., Gramfort, A., Michel, V., Thirion, B., Grisel, O., … Duchesnay, E. (2011). Scikit-learn: Machine Learning in Python. *Journal of Machine Learning Research*, *12*, 2825–2830.

Pham, T. T., Monnard, A., Helenius, J., Lund, E., Lee, N., Müller, D. J., & Cabernard, C. (2019). Spatiotemporally Controlled Myosin Relocalization and Internal Pressure Generate Sibling Cell Size Asymmetry. *IScience*, *13*, 9–19. https://doi.org/10.1016/j.isci.2019.02.002

Pillitteri, L. J., Guo, X., & Dong, J. (2016). Asymmetric cell division in plants: mechanisms of symmetry breaking and cell fate determination. *Cellular and Molecular Life Sciences : CMLS*, *73*(22), 4213–4229. https://doi.org/10.1007/s00018-016-2290-2

Priya, R., & Yap, A. S. (2015). Active tension: the role of cadherin adhesion and signaling in generating junctional contractility. *Current Topics in Developmental Biology*, *112*, 65–102. https://doi.org/10.1016/bs.ctdb.2014.11.016

Ragkousi, K., & Gibson, M. C. (2014). Cell division and the maintenance of epithelial order. *The Journal of Cell Biology*, *207*(2), 181–188. https://doi.org/10.1083/jcb.201408044

Roure, A., Rothbächer, U., Robin, F., Kalmar, E., Ferone, G., Lamy, C., … Lemaire, P. (2007). A multicassette Gateway vector set for high throughput and comparative analyses in ciona and vertebrate embryos. *PloS One*, *2*(9), e916. https://doi.org/10.1371/journal.pone.0000916

Rueden, C. T., Schindelin, J., Hiner, M. C., DeZonia, B. E., Walter, A. E., Arena, E. T., & Eliceiri, K. W. (2017). ImageJ2: ImageJ for the next generation of scientific image data. *BMC Bioinformatics*, *18*(1), 529. https://doi.org/10.1186/s12859-017-1934-z

Sallé, J., Xie, J., Ershov, D., Lacassin, M., Dmitrieff, S., & Minc, N. (2019). Asymmetric division through a reduction of microtubule centering forces. *The Journal of Cell Biology*, *218*(3), 771–782. https://doi.org/10.1083/jcb.201807102

Schindelin, J., Arganda-Carreras, I., Frise, E., Kaynig, V., Longair, M., Pietzsch, T., … Cardona, A. (2012). Fiji: an open-source platform for biological-image analysis. *Nature Methods*, *9*(7), 676–682. https://doi.org/10.1038/nmeth.2019

Schlesinger, A., Shelton, C. A., Maloof, J. N., Meneghini, M., & Bowerman, B. (1999). Wnt pathway components orient a mitotic spindle in the early Caenorhabditis elegans embryo without requiring gene transcription in the responding cell. *Genes & Development*, *13*(15), 2028–2038. https://doi.org/10.1101/gad.13.15.2028

Smith, P., Azzam, M., & Hinck, L. (2017). Extracellular Regulation of the Mitotic Spindle and Fate Determinants Driving Asymmetric Cell Division. *Results and Problems in Cell Differentiation*, *61*, 351–373. https://doi.org/10.1007/978-3-319-53150-2_16

Travis E. Oliphant (Brigham Young University). (2007). Python for Scientific Computing Python Overview. *Computing in Science and Engineering*, 10–20.

van der Walt, S., Schönberger, J. L., Nunez-Iglesias, J., Boulogne, F., Warner, J. D., Yager, N., … scikit-image contributors. (2014). scikit-image: image processing in Python. *PeerJ*, *2*, e453. https://doi.org/10.7717/peerj.453

Veeman, M., & Reeves, W. (2015). Quantitative and in toto imaging in ascidians: Working toward an image-centric systems biology of chordate morphogenesis. *Genesis*, *53*(1), 143–159. https://doi.org/10.1002/dvg.22828

Veeman, M. T., Chiba, S., & Smith, W. C. (2011). Ciona Genetics. In F. J. Pelegri (Ed.), *Methods in molecular biology (Clifton, N.J.)* (Vol. 770, pp. 401–422). Totowa, NJ: Humana Press. https://doi.org/10.1007/978-1-61779-210-6_15

Veeman, M. T., & Smith, W. C. (2013). Whole-organ cell shape analysis reveals the developmental basis of ascidian notochord taper. *Developmental Biology*, *373*(2), 281–289. https://doi.org/10.1016/j.ydbio.2012.11.009

Winkley, K., & Veeman, M. (2018). A temperature-adjusted developmental timer for precise embryonic staging. *Biology Open*, *7*(6). https://doi.org/10.1242/bio.032110

Wühr, M., Tan, E. S., Parker, S. K., Detrich, H. W., & Mitchison, T. J. (2010). A model for

cleavage plane determination in early amphibian and fish embryos. *Current Biology : CB*, *20*(22), 2040–2045. https://doi.org/10.1016/j.cub.2010.10.024

Figures – Chapter 4

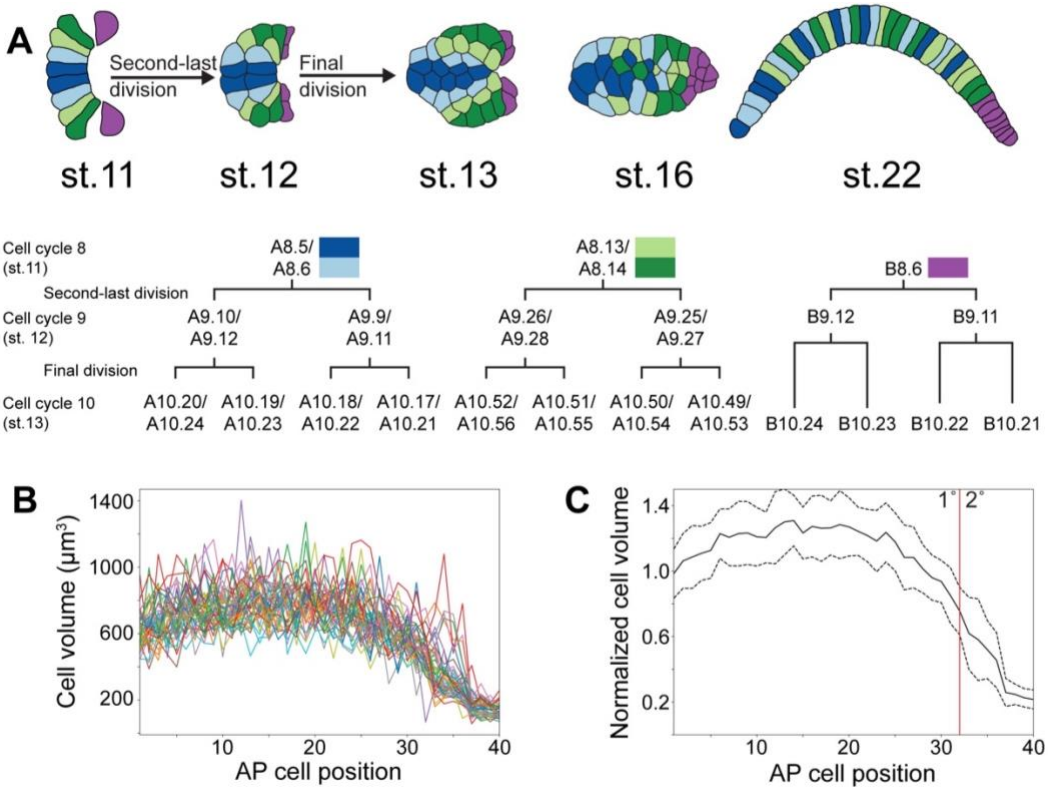

Figure 4.1 Notochord Development and Tapering

A) Top: cartoon representation of notochord morphogenesis using Hotta's staging series [3]. Colors represent various founder lineages (dark blue, A8.5; light blue, A8.6; light green, A8.13; dark green, A8.14; purple, B8.6). Bottom: lineage tree for notochord cells starting at the 112-cell stage. (B) Notochord cell volumes after intercalation as a function of AP position from cell 1 (anterior) to cell 40 (posterior). Each colored line represents a different embryo. (C) Mean notochord cell volume after intercalation as a function of AP position. Volumes are normalized to the average notochord cell volume per embryo to control for variation in egg or embryo size. Vertical red line indicates the division between the primary (A-line) and secondary (B-line) notochord. Mean (solid line) ± 1 SD (dotted lines).

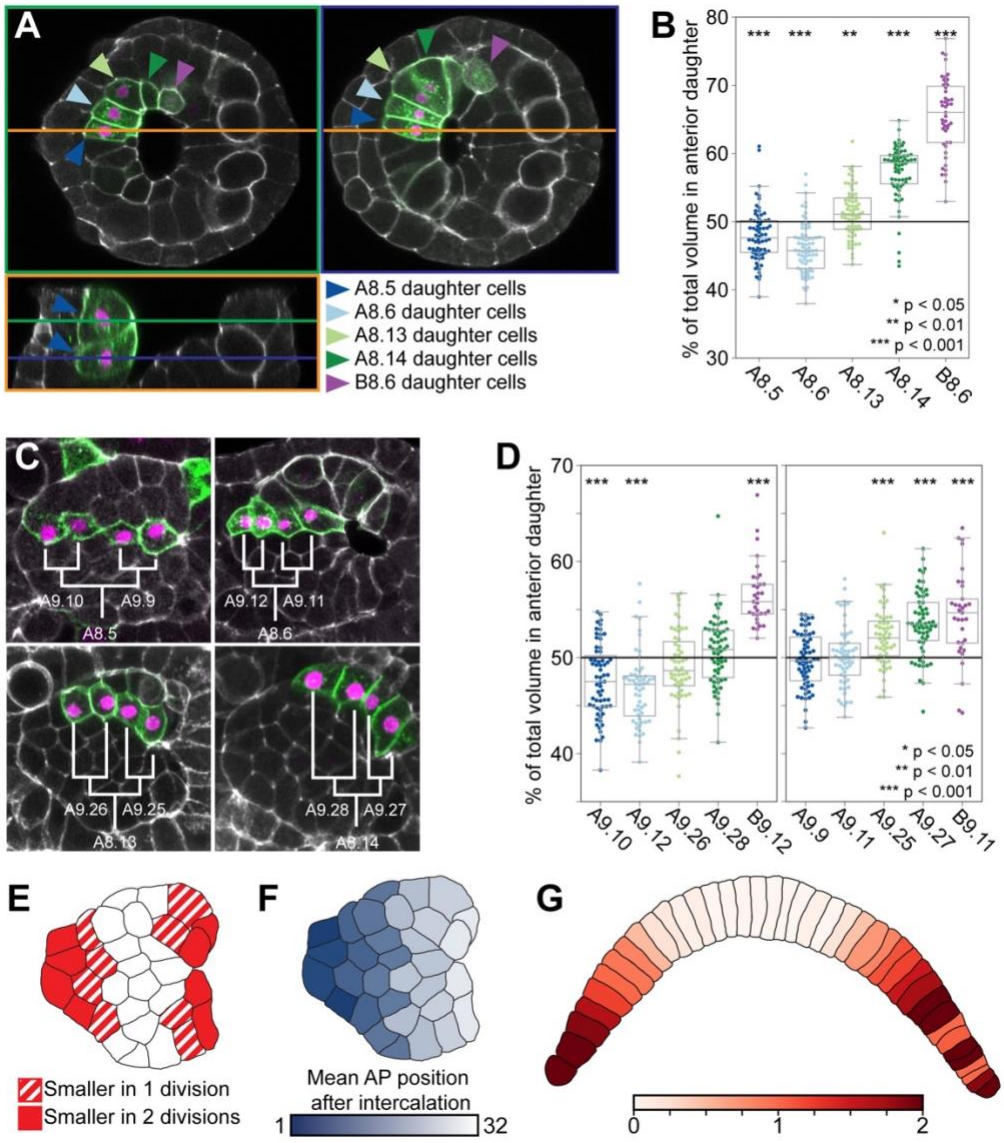

Figure 4.2 Iterative Unequal Cleavages Control Notochord Cell Volume Differences

(A) Selected z slices and orthogonal slices immediately after the second-last notochord cell division. Colored arrowheads show sibling cells derived from each of the 5 founder lineages. Colored lines and image outlines show corresponding orthogonal planes. (B) Sibling cell volume ratios showing the percent of total sibling pair volume that is in the anterior cell after the second-last division. Asterisks indicate a significant difference from 50% (equal cleavage) (C) 4-cell clones arising from each of the 4 primary founder lineages after the final division. Green is Bra >membrane-GFP, magenta is Bra > H2B-HA, and white is phalloidin. (D) Sibling cell volume ratios showing the percent of total sibling pair volume that is in the anterior cell after the final division. Asterisks indicate a significant difference from 50% (equal cleavage) (E and F) Primary notochord primordium overlaid with asymmetric division patterns (E) and AP position after intercalation (F). See Methods for full details on intercalation position. (G) Average number of times each cell in the intercalated notochord is the smaller daughter of an asymmetric division.

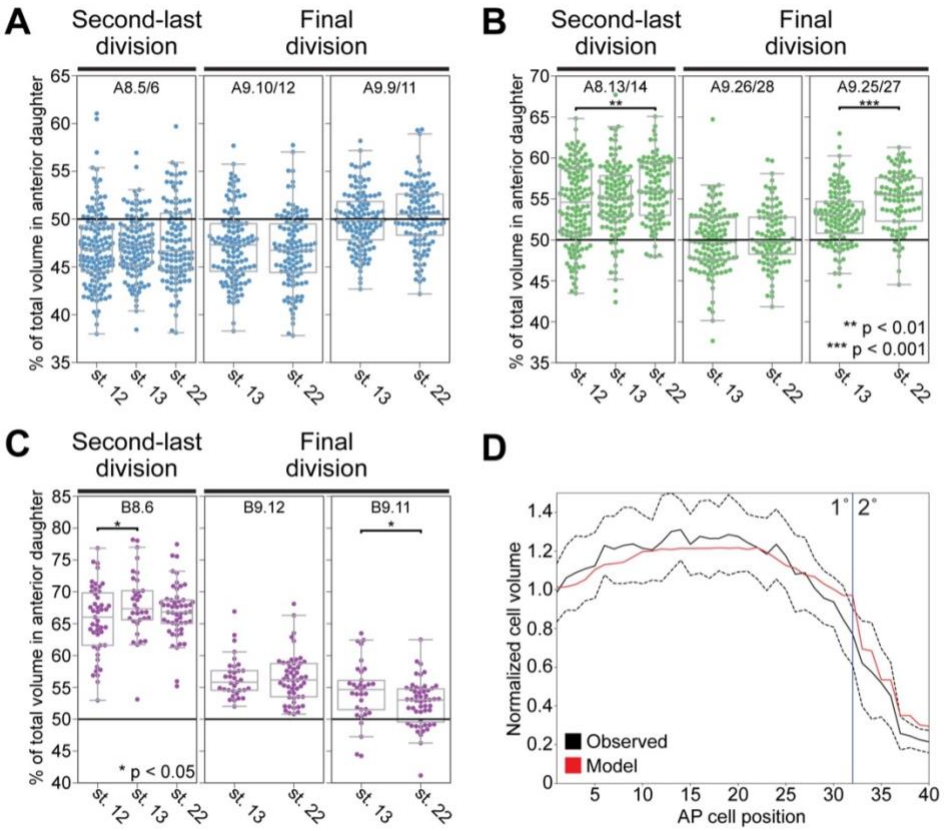

Figure 4.3 Sibling Cell Volume Ratios Are Stable Over Time

(A–C) Sibling cell volume ratios for the second-last and final division at the indicated stages for primary anterior clones (A), primary posterior clones (B), and the secondary notochord (C). Stage (St.) 12 is immediately after the second-last division, St. 13 is immediately after the final division, and St. 22 is after intercalation is complete. The plot labels correspond to the mother cell(s) for the sibling volume ratio shown. See STAR Methods for more details. (D) Statistical model of mean cell volume as a function of AP position as predicted by founder cell volumes and observed patterns of unequal cleavage and cell intercalation (red line; see STAR Methods for full details). Black line indicates mean observed volumes ± 1 SD (dashed lines).

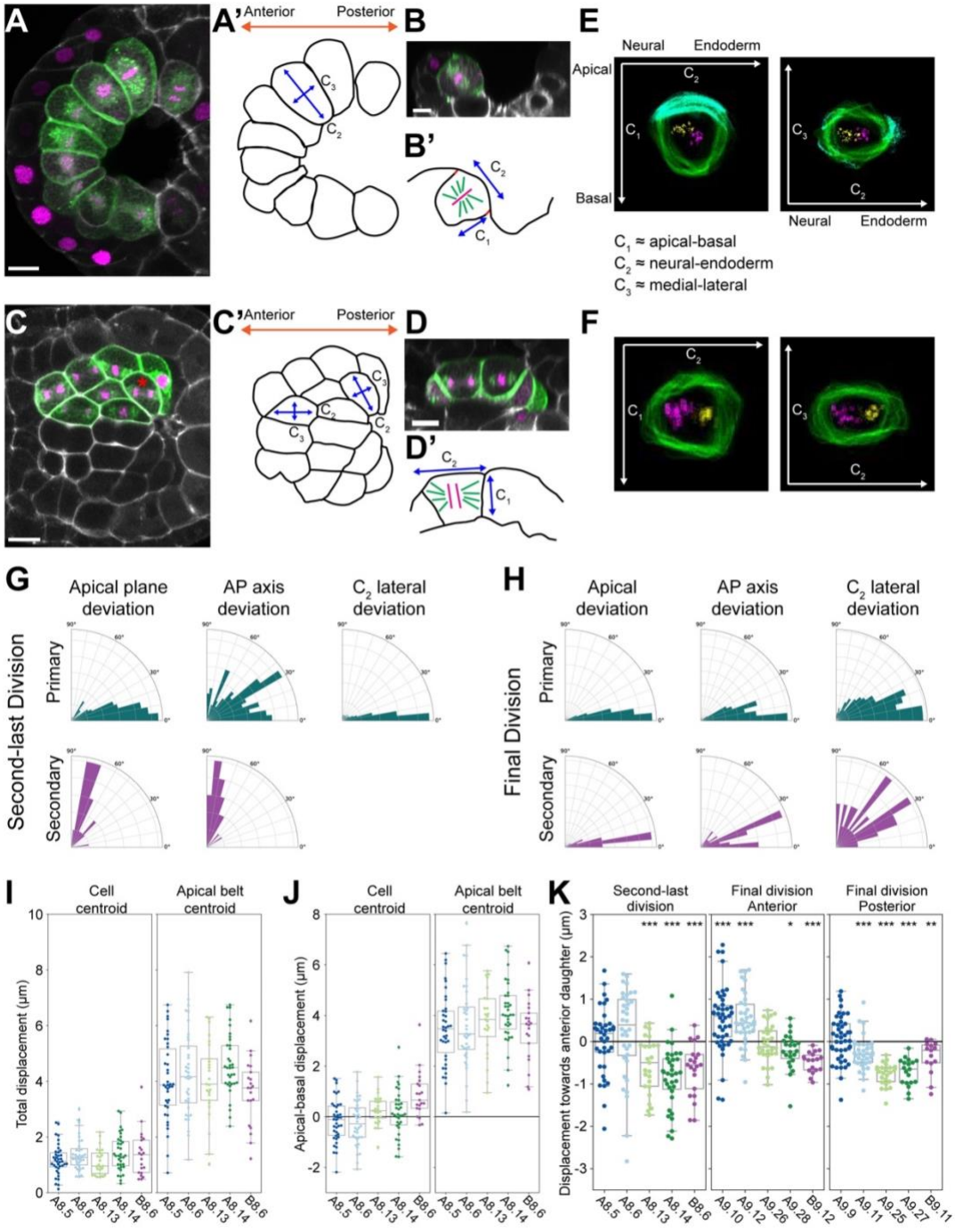

Figure 4.4 Spindle Orientation and Displacement Varies between Lineages and Cell Cycles

(A–D) Selected z slices and corresponding cell outlines along with coordinate system vectors overlaid for the second-last (A and A') and final divisions (C and C') along with orthogonal views for the second-last (B and B') and final divisions (D and D'). Scale bar, 10 µm. (E and F) Eigen-cell representation of stereotyped blastomere shapes made by registering segmented cell outlines and spindle pole coordinates to the C1–C3 coordinates system with cell centroids aligned to the center of the image. Each image is a summed intensity projection through the

depth of the spindle for dozens of segmented and overlaid cells. Basolateral cell surfaces are shown in green and apical surfaces in cyan for the second-last division A8.13 blastomere shown in (E). All cell surfaces are shown in green for the final division A9.10 blastomere in (F), as we did not define distinct apical surfaces at this stage. Spindle poles are marked in yellow (future posterior daughter) and magenta (future anterior daughter). Because the notochord inverts between the second-last and final division, the anterior and posterior daughter poles are reversed between (E) and (F). See also Figure S3. (G and H) Angle of deviation between the mitotic spindle and the apical plane, the mitotic spindle and the anterior posterior axis, and the mitotic spindle and C2 (lateral component only) for the second-last division (G) and the final division (H). (I) Total distance between the spindle midpoint and the cell centroid or apical belt centroid in the second-last division. (J) Apical-basal displacement away from the apical surface of the spindle midpoint from the cell centroid or apical belt centroid in the second-last division. (K) Distance that the spindle midpoint is displaced from the cell centroid specifically in the direction of the future anterior daughter. Asterisks show a significant difference from 0 mm. *$p < 0.05$; **$p < 0.01$; ***$p < 0.001$

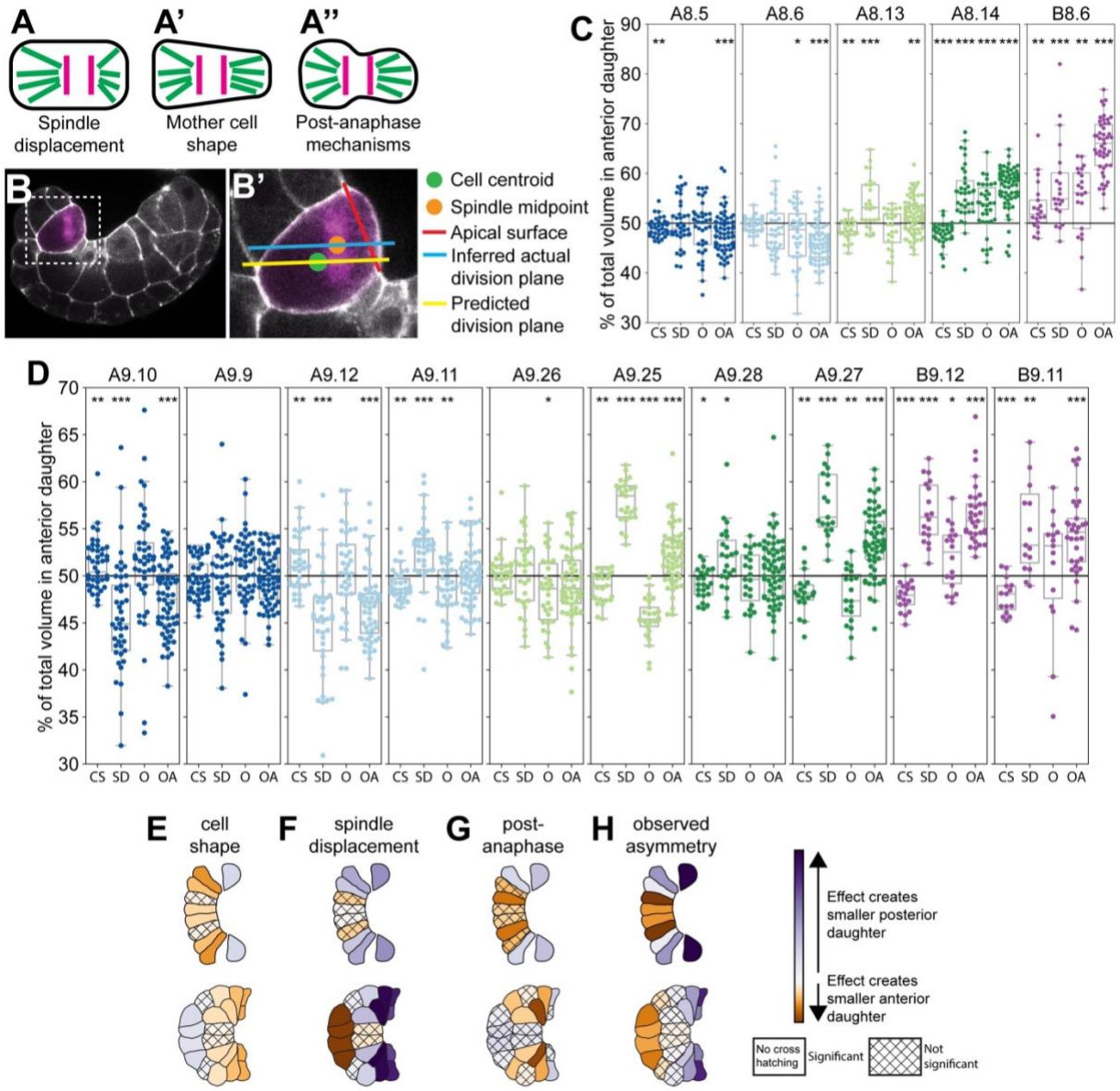

Figure 4.5 Multiple Mechanisms of Unequal Cleavage

(A–A'') Three mechanisms that could contribute to sibling cell volume asymmetries. Magenta indicates segregating chromosomes, and green represents astral microtubules. (B) Transverse view during the second-last notochord division. H2B-HA is in magenta, and phalloidin is in white. Anterior is to the left, and vegetal is up. (B') Expanded view of the indicated area in (B) shows cell landmarks and two potential cleavage planes: one defined by the actual position and orientation of the spindle (blue) and another defined by the cell centroid and actual spindle orientation (yellow). (C and D) Separate effects inferred for mother cell shape (CS), spindle displacement (SD), and other post-anaphase mechanisms (O) together with the resulting observed asymmetry (OA) seen after cytokinesis for the second-last division (C) and the final division (D). *$p < 0.05$; **$p < 0.01$; ***$p < 0.001$. (E–H) Graphical representation of the distinct effects inferred for (E) mother cell shape, (F) spindle displacement, and (G) late post-anaphase effects as well as the observed asymmetries (H) mapped onto the embryo. The color scales are normalized to the largest effects inferred toward a smaller versus larger anterior daughter, and

white represents an effect size of 0. All cells are colored to the mean magnitude of the effect for that particular blastomere pair. All effects are statistically significant at $p < 0.05$ unless indicated with cross hatching.

Chapter 5 - Single cell analysis of MAPK-dependent cell fate specification

Abstract

Inductive signaling interactions between different cell types are a major mechanism for the further diversification of cell fates. Most blastomeres in the model chordate *Ciona* become restricted to a single fate during a narrow window between the 64-cell and mid-gastrula stages. Vegetal FGF signaling through the MAPK pathway plays a major role in directly or indirectly establishing many of these cell types. We performed single cell RNAseq at the 64-cell, 110-cell and mid-gastrula stages using both control embryos and embryos treated with the MAPK pathway inhibitor U0126. We identified 53 distinct cell states in wildtype embryos, 25 of which are dependent on MAPK signaling. These transcriptomic states included novel cell types and novel MAPK dependencies along with many identified in diverse previous studies. Unexpectedly, we find that posterior endoderm does not become transfated to sibling cell types upon MAPK pathway inhibition, but instead adopts a novel pattern of gene expression not seen in unperturbed embryos. We find that differential Ets motif enrichment provides a robust indicator of which bifurcations are directly transcriptionally dependent on FGF signaling. The Ets family transcription factor Elk1 becomes upregulated in almost all the putatively direct inductions, supporting a new hypothesis that it may act in a feedback loop. We examine the bifurcation between primary notochord and A-line neural cells in detail and find support for the hypothesis that most early notochord genes are initially induced directly downstream of FGF, in parallel to and not downstream of the key notochord regulator Brachyury. These results support a 'broad-hourglass' model of cell fate specification in which many other genes are induced in parallel to key tissue-specific regulators via the same set of transcriptional inputs.

Introduction

Waddington used his famous epigenetic landscape (Figure 5.1A) to propose the now well-established concept that the journey from the totipotent fertilized egg to the myriad distinct cell types found in mature animals involves a series of bifurcations in which cells can follow different trajectories of differentiation (Waddington, 1957). We now know that these cell fate bifurcations sometimes involve the asymmetric inheritance of cytoplasmic cell fate determinants between sibling cells, but more often involve inductive interactions between different cell types. Decades of work in various model organisms have mapped out inductive interactions between many different cell types, identified specific signal transduction pathways used to induce specific cell fates, and identified important transcription factors controlling cell type-specific gene expression. Until recently, however, the global transcriptomic changes underlying bifurcations in cell fate have been elusive. RNAseq can be used to transcriptionally profile cell populations purified by FACS (W. M. Reeves et al., 2017), but it is hard to scale this strategy to profile the full complexity of cell types in even simple developing embryos. Also, the maturation times for fluorescent markers of cell fates make it hard to purify distinct cell types until well after they are first specified. With new single-cell technologies, however, it is now possible to quantify how inductive signals cause genome-wide transcriptomic changes in newly-specified cell types, allowing us to understand cell fate bifurcation events in an unprecedentedly comprehensive manner.

Single-cell RNA sequencing overview

There are different technologies for single-cell RNA sequencing (scRNAseq), but almost all involve the dissociation of whole embryos or tissues into a suspension of individual cells, the partitioning of single cells from that suspension into individual compartments, and some form of

RNA capture in each compartment that leads to the molecular barcoding of transcripts from each cell with a unique oligo sequence. After deep sequencing, these barcodes can then be used to identify which reads come from which cell.

The most widely-used scRNAseq approaches use microfluidic devices to encapsulate single cells and oligonucleotide coated RNA capture beads inside nanoliter sized aqueous droplets in an oil emulsion (Macosko et al., 2015). Inside of these droplets, the cells are lysed and the RNA is captured with barcoded oligonucleotides. Depending on the technology, reverse transcription may take place before or after the emulsion is broken, and then the cDNA is amplified and sequenced. Post-sequencing analysis typically involves statistical correction for technical and biological biases, followed by linear and non-linear dimensional reduction and clustering to identify cells with shared transcriptional profiles. The resulting clusters can be mapped to known cell types based on the expression of known marker genes and predicted markers of novel cell types can be validated and mapped onto the embryo by *in situ* hybridization. scRNAseq is an emerging technology with many different competing approaches at each of these steps, from cell isolation all the way through post-sequencing analysis. These different methodologies all have distinct advantages and disadvantages. For example, droplet-based technologies are commercially available and analysis pipelines are well established. However, they are often limited by the number of cells which they are able to encapsulate at a time, often in the scale of thousands to tens of thousands (Macosko et al., 2015). On the other hand, approaches such as single-cell combinatorial indexing are able to capture millions of cells (J. Cao et al., 2019), orders of magnitudes more than droplet based approaches, but are still in their infancy of development as a technology and are not yet widely commercially available.

Early development in *Ciona*

In order to quantify the transcriptomic changes associated with cell fate bifurcation events, it is necessary to identify mother-daughter-sibling relationships between scRNAseq clusters. Here I use the mother-daughter-sibling terminology to refer to relationships between transcriptional states. This will vary in different contexts in how congruent it is with the actual lineages of cell divisions. Identifying these relationships de novo presents a complicated technical and conceptual challenge and has been the primary focus of many scRNAseq studies. This is especially true in systems where differentiation is not synchronized and pseudotime inference strategies are needed to reconstruct developmental trajectories. In the invertebrate chordate *Ciona*, however, the simple, synchronous and exceptionally stereotyped cell lineages largely bypass this issue and allow one to move on to more interesting mechanistic questions.

Ciona has several other advantages that make it an excellent model for quantitative analysis of cell fate bifurcations using scRNAseq at the scale of the entire embryo. *Ciona* embryos are small and simple, yet stereotypically chordate. This makes relatively deep coverage on a per-cell-type basis of an entire chordate embryo easily achievable in single-cell experiments. Additionally, most *Ciona* blastomeres become restricted to a single fate during a narrow window between the 64-cell and mid-gastrula stages (Nishida, 1987; Nishida & Satoh, 1983, 1985), allowing the analysis of many cell fate specification events with a relatively short time course of sequenced stages. These characteristics are accompanied by a rich literature base establishing many cell type-specific markers, specific inductive interactions and extensive dissection of gene regulatory networks (Brozovic et al., 2018).

The early patterning of the *Ciona* embryo up to the 32-cell stage relies primarily on two intersecting patterning systems. The first involves cortical rearrangements of the ooplasm and

polarity breaking events in response to sperm entry, which culminate in the formation of a structure known as the centrosome attracting body (CAB) in the posterior vegetal blastomeres at the 8-cell stage. The CAB is then continuously partitioned into the posterior-most vegetal cells during the proceeding cell cycles and is thought to be responsible for directly or indirectly driving most of the anterior-posterior patterning of the early embryo [reviewed in (Sardet et al., 2007)]. The second system involves reciprocal interactions between maternally deposited Gata.a factors and nuclear β-catenin. In subsequent rounds of division at the 16-cell and 32-cell stages, these two pathways lead to the establishment of the three germs layers through antagonistic gene expression and restricted domains of nuclear localization (Hudson et al., 2013; K. Imai et al., 2000; Kaoru S. Imai et al., 2016; Rothbächer et al., 2007). A more detailed explanation of these mechanisms is presented in Chapter 2.

At the 32-cell stage only a subset of the endodermal blastomeres are restricted to a single fate, however nearly all the remaining blastomeres will become fate restricted in the next two cell cycles (Nishida, 1987; Nishida & Satoh, 1983, 1985). The majority of the fate bifurcation events that take place in this time window are dependent on MAPK signaling (Hudson & Lemaire, 2001; Kim et al., 2007; Pasini et al., 2006; Picco et al., 2007; Shi & Levine, 2008; Yasuo & Hudson, 2007). MAPK activity at these stages is controlled by FGF agonists which are expressed at the vegetal pole downstream of β-catenin (Hudson et al., 2016; Kaoru S. Imai, 2003), and by the FGF antagonist, ephrinAd, which is expressed in the animal hemisphere downstream of Gata (Picco et al., 2007). As development continues through the 110-cell and mid-gastrula phases, other FGF agonists and antagonists become expressed in other lineages, such as the trunk lateral cells, and in complex patterns in the neural plate (Hudson et al., 2007).

MAPK signaling induces expression of a Nodal ligand in a lateral animal cell population (Hudson & Yasuo, 2005). The Nodal signal activates downstream expression of Notch pathway ligands in neighboring cells and this Nodal/Delta relay further refines several tissue types at the 110-cell and mid-gastrula stages. This is particularly evident in the mediolateral patterning of the neural plate (Hudson & Yasuo, 2005).

MAPK activity and repression are thought to be either directly or indirectly responsible for nearly all the fate bifurcations occurring after the 32-cell stage in the *Ciona* embryo. Therefore, we performed whole embryo scRNAseq at three key stages during cell fate specification both with and without the MEK inhibitor U0126. Using this data, we set out to characterize the repertoire of transcriptomic states in the early *Ciona* embryo, and also define the transcriptomic responses of different precursor cells in response to FGF/MAPK signaling. We exploited the fixed lineages of *Ciona* to ask broad, systems-level questions about the gene regulatory networks (GRN) that control cell fate specification events, with an emphasis on inferring new features of the GRN controlling notochord specification and differentiation.

Results and Discussion

Single-cell RNAseq of *Ciona* embryos recapitulates known expression patterns and reveals new transcriptional states

We performed single-cell RNA sequencing of *Ciona* embryos using a modified dropSeq (Macosko et al., 2015) approach at the 64-cell, the 110-cell, and mid-gastrula stages (stages 8, 10, and 12 in Hotta's *Ciona* staging series (Hotta et al., 2007)) (Figure 5.1B). These stages are spaced only ~45-60 minutes apart each at 18˚C and span a period in which most *Ciona* blastomeres become restricted to a single major fate. *Ciona* are hermaphroditic, and in order to obtain enough cells for each timepoint to ensure adequate coverage of each left-right blastomere pair, we pooled gametes from multiple adults for collection and analysis. Upon initial post-sequencing analysis and clustering, we generated first-pass UMAP plots. Each point on the UMAP plots represents a single set of 3' RNAs associated with a unique cell barcode (also known as a "single-cell transcriptome attached to microparticle" (STAMP)), and the distances between points represent similarities and differences in gene expression across the entire transcriptome. The distinct clusters evident on the UMAP plots represent different cell types with their own distinct transcriptional states. We compared the gene expression profiles of the STAMPs contained within each cluster to those already known from extensive *in situ* hybridization screens in *Ciona* (Brozovic et al., 2018; K. S. Imai, 2004, 2006). We identified several duplicate clusters for many cell types (Figure 5.2 A-C). These duplicate clusters were unexpected based on previous *Ciona* literature, and upon further inspection, we found that the number of duplicate clusters typically matched the number of *Ciona* adults used in each experiment.

A recently published *Ciona* single-cell RNAseq profiling study of a much earlier stage near the time of zygotic genome activation found that single-cell transcriptome profiles tended to cluster not by cell type, but by embryo-of-origin (Ilsley et al., 2020). As that study only profiled 4 hand-dissected embryos, each of which was from a different mother, they were unable to determine if these effects were due to differences between mothers of origin or individual embryos. To determine if differential deposition of RNA between the different adults used in each experiment could be driving our observed duplication of cell type clusters, we took advantage of *Ciona's* relatively high rate of polymorphism and called SNPs across the entire genome for each STAMP in our data. We calculated a metric of relatedness between all pairwise comparisons of STAMPs at each stage and hierarchically clustered the resulting relatedness matrix. The dendrograms obtained from clustering at each stage contained several long branches, which matched the number of adults used in each experiment (Figure 5.2 D-F). We then mapped the putative maternal identity back on the UMAP plots and found that the STAMPs tended to be clustering primarily by their mother at early stages, with this effect diminishing at later stages (Figure 5.2 G-I). This trend is consistent with our expectations if maternally deposited RNAs are contributing the majority of the variance between STAMPs early on and if this effect is "washed out" over time as zygotic transcription products accumulate in the cells. We then used the variable regression capability of the ScaleData function in Seurat, which creates a linear model for each gene expression feature in the data based on the effects of a given variable, to regress out the mother-of-origin effects and allow cells to cluster based strictly on cell type-specific gene expression.

Following post-sequencing SNP analysis and computational clustering, we again generated UMAP plots for each stage (Figure 5.3 A-C). This time we were able to assign cell

identities to the scRNAseq clusters at all three stages, and the number of clusters was now in line with expectations based on extensive prior gene expression profiling (Figure 5.3 E-G). Some of these clusters represented broad territories of the early embryo such as the presumptive epidermis, but others had single-blastomere resolution such as the lateral columns of the posterior neural plate at the mid-gastrula stage. Expression patterns of the most highly variable transcription factors in our STAMPs at the 110-cell stage are generally similar to their previously characterized expression patterns by *in situ* hybridization but revealed important quantitative dynamics to expression patterns that had previously been appreciated only in a binary ON/OFF framework. (Figure 5.4)

In addition to recapitulating almost all of the cell types expected at these stages based on the *Ciona* fate map and gene expression databases, we also identified three previously unappreciated transcriptional states in the mid-gastrula embryo: a cluster of putative posterior ventral midline epidermal precursors; and two distinct cell states within the b-line neural lineage. The fate of all blastomeres in the 110-cell embryo have been previously analyzed (Nishida & Satoh, 1985), and it is known how the posterior animal blastomeres contribute to distinct dorsal-ventral and anterior-posterior locations in the tail epidermis at tailbud stages (Pasini et al., 2006). The ventral midline is known to be functionally and transcriptionally distinct from more lateral tail epidermis at later stages, but the ventral midline patterning mechanisms are not well understood. Here we identify a distinct cluster of posterior epidermal cells that we tentatively identify based on Nkx-A, Hox12, and Wnt5 expression as the posterior-most cells contributing to the ventral midline tail epidermis at tailbud stages (descendants of b8.27 cell pair) (Figure 5.3 C). Additionally, we are able to identify two distinct clusters of b-line neural cells at the mid-gastrula stage that express distinct markers that have yet to be analyzed by *in situ* hybridization.

Patterning of b-line neural cells is not well understood, so these new clusters may be quite informative.

scRNAseq captures temporal patterns of gene expression

Ciona embryos have stereotyped cell lineages, so the parent and/or daughter STAMP clusters of any STAMP clusters at a given stage can be determined *de facto* based on previously published literature and knowledge of the cell lineages. We first assigned cell types to each STAMP cluster separately at each stage. To confirm the consistency of these assignments between stages, we clustered the STAMPs from all three of our stages in the same reduction of high-dimensional gene expression space. The UMAP plot from this reduction represented the known lineages in *Ciona* embryos relatively well (Figure 5.5 A-B). The STAMPs from a given lineage across stages tended to cluster close together in a pattern that radiated outwards from the center of the UMAP plot with STAMPs that were later in developmental time being further from the center (Figure 5.2 A). This generally confirmed that our cell type assignments were consistent between lineages and showed an overarching trend that cell types established at the 64-cell stage or earlier tended to become far more transcriptionally divergent over time.

Some FGF dependent cell types are not transfated to sibling cell types upon MAPK inhibition

To understand the transcriptional responses to FGF/MAPK signaling, we treated embryos with the MEK inhibitor U0126 from the 16-cell stage. Treatment with U0126 at this timepoint is known to inhibit fate acquisition of mesenchyme, endoderm, and notochord (Kim et al., 2007; Shi & Levine, 2008; Yasuo & Hudson, 2007). It also prevents neural induction in two subsets of animal blastomeres (C. Hudson, 2002) and disrupts the mediolateral patterning of the A-line neural plate, which secondarily prevents the establishment of A-line secondary muscle fate. The

effects on A-line neural plate mediolateral patterning are mediated through a Nodal/Delta signaling relay downstream of FGF/MAPK signaling (Hudson & Yasuo, 2005). This Nodal/Delta relay is also required for the fate bifurcation event involving secondary notochord (Hudson & Yasuo, 2006). We found that many of the expected cell lineages are missing from the drug treated embryos (Figure 5.6 A-B). In order to define a metric of FGF dependence for each bifurcation, we predicted cell types in the U0126 STAMPs using the cell type label transfer function from Seurat. These predictions occasionally had to be manually curated, and are not a definitive cell type assignment, but seemed to largely align with our expectations from previously published literature. We performed a chi-square test for whether drug treatment influences the proportion of cells in sibling clusters (using the STAMPs for all descendant lineages of a STAMP cluster at mid-gastrula as a proxy) and took the negative log of the p-value as our metric. We were not able to compute this metric for all bifurcations in the instance that the parental cluster of a bifurcation was itself FGF-dependent at an earlier stage. We find that, as expected, most of the bifurcations in these stages were FGF dependent with one of the sibling cell types lost after U0126 treatment (Figure 5.6 B) and a corresponding increase in number of STAMPs for the sibling cell type. The only bifurcation that was not significant was the B7.5/B7.6 bifurcation which is believed to be FGF independent at this stage (Figure 5.6 B). For the U0126 sensitive bifurcations, there was substantial variability in the FGF sensitivity metric (Figure 5.6 C). This may reflect a lack of sensitivity of the label transferring function we used to assign fates to the U0126 treated cells when the divergence distance in gene expression space of the FGF dependent cluster from their FGF independent siblings is small.

One exception to the trend of FGF-dependent cell types being transfated to the sibling cell type is the B-line posterior endoderm. No STAMPs from U0126 treated embryos match the

transcriptional profile of control treated endodermal STAMPs. (Figure 5.7 A-C) Additionally, we see an increase in U0126 treated cells that have an overlapping transcriptional profile with control treated A7.6 TLC precursor STAMPs, and also a novel cell cluster that is not detected in control embryos (Figure 5.7 A-C). This novel cluster expresses both some markers of endodermal fate, as well as some markers of muscle fate at the 64-cell stage (Figure 5.7 D), along with some genes that are not strongly expressed in either endodermal or muscle cells in control conditions.

Previous studies in *Ciona* have demonstrated that the A-line anterior endoderm expresses markers of its partial sibling fate TLC precursor (Figure 5.7 E) when FGF signals are repressed (Shi & Levine, 2008). In a different tunicate, *Halocynthia rotezi,* FGF inhibition has been reported to cause the posterior B-line endoderm to adopt a cousin-cell muscle fate (Figure 5.7 F) in explants, but not in whole embryos (Kondoh et al., 2003). This implies that there are overlapping pathways that promote endodermal fate over muscle fate in the B-line posterior endoderm. Maternal β-catenin is a well-established endoderm determinant in ascidians and is involved in germ layer segregation early in development. One interpretation is that vegetal FGF signaling acting downstream of maternal β-catenin is required for the normal posterior endoderm transcriptional regime, but that β-catenin alone is sufficient to make the B6.1 posterior endoderm lineage distinct from the B6.2 muscle/mesenchyme/2˚ notochord lineage. In *Halocynthia*, it has been also been proposed that BMP factors expressed in the adjacent A-line anterior endoderm blastomeres are important for posterior endoderm fate, however this expression pattern of BMP factors is not conserved in *Ciona*.

Elk1 as a putative autoregulatory TF in an FGF dependent feedback loop

After establishing which lineages are FGF dependent at these stages in the *Ciona* embryo by scRNAseq, we wondered to what extent these diverse lineages exhibit a universal FGF transcriptional response versus lineage specific responses. To address this, we clustered the Log_2 fold-change in expression between FGF dependent lineages and their FGF independent siblings for the top 35 most variably expressed TFs. Most lineages exhibit their own characteristic responses, but we noticed a striking and unexpected pattern that the Ets family transcription factor Elk1 was consistently upregulated in the FGF dependent cell type compared to its sibling cell type (Figure 5.8 A). Published *in situ* expression patterns of Elk1 at these stages are quite messy and unclear, so it is possible that this relationship may have previously been missed without the quantitative data provided by scRNAseq. Additionally, Elk1 expression is MAPK dependent as demonstrated by its drastically reduced expression level in U0126 treated embryos (Figure 5.8 B), and the putative enhancer region of Elk1 upstream of its transcription start site contains multiple Ets motifs (Figure 5.8 C). This led us to hypothesize that Elk1 expression is at least a proxy for Ets family transcriptional activity and given that Elk1 is itself an Ets family TF, it may have an autoregulatory feedback role in FGF/MAPK transcriptional activity.

Inferring the transcriptional role of FGF signaling in MAPK dependent cell fate bifurcations

For the cell fate bifurcations that occur in the time window that we analyzed here, the genome-wide transcriptional responses to FGF/MAPK mediated through Ets family transcription factors have never been measured. We sought to measure aspects of this response to make inferences about the directness of the transcriptional dependence of FGF/MAPK signaling in FGF/MAPK dependent lineage decisions. The FGF/RAS/MAPK/MEK signaling pathway

culminates in *Ciona* and other animals in a transcriptional response largely mediated through Ets family transcription factors, of which the *Ciona* genome contains 11 putative members (Bertrand et al., 2003; Gainous et al., 2015). To quantify the contribution of Ets family and other transcription factors to these FGF-induced cell states, we performed transcription factor binding site (TFBS) enrichment analysis. TFBS enrichment analysis uses statistical models to determine if the binding site sequence for a particular transcription factor (TF) is overrepresented in a set of "target" DNA sequences compared to a set of control DNA sequences. TFs bind to DNA in cis-regulatory modules known as enhancer regions. In *Ciona*, it is understood that most enhancers for genes lie in the few thousand base pairs upstream of the transcription start site. We are most interested in how different transcription factors contribute to making one cell type different from its sibling cell type. Therefore we used the 1.5 kB of DNA upstream of the transcription start site for sets of genes upregulated in a cell type compared to its sibling cell type as the target sequences, and the 1.5 kB of DNA upstream of the transcription start site for sets of genes downregulated in a cell type compared to its sibling cell type as the control sequences. Previous literature has established a list of putative open chromatin regions at these stages using whole embryo ATACseq (Madgwick et al., 2019). We sought to incorporate this data to improve the power of our methods and performed the TFBS analysis in parallel to the method above using the open chromatin regions determined from ATACseq that overlapped our 1.5 kB regions as our sets of control and target DNA sequences. Following these two analysis methods, we averaged the enrichment metric z-scores for each TFBS from each method to get a combined z-score of binding site enrichment in target sequences compared to control sequences.

Z-scores for the Ets family TFBS vary widely across the sibling-cell types, indicating that some bifurcations have large transcriptional responses down-stream of Ets signaling, while

others have relatively small responses. This likely reflects some of these cell fate bifurcations depending on the Nodal/Notch signaling relay downstream of FGF signaling, while others depend more directly on a large FGF dependent transcriptional response that is mediated by Ets family TFs. While using the genes differentially expressed between sibling cell fates as the control and target sets for TFBS enrichment informs the way we think about the transcriptional differences driving the divergence between cell types, it doesn't give us clear insight into the mechanism at play. For example, if a TFBS is enriched in one cell type vs another using this method, it may be due to increased expression in one sibling, or increased repression in the other sibling. To address this, we again performed TFBS enrichment analysis, this time using the genes that are up- and downregulated in a cell type compared to all other cell types at a given stage to form our target and control DNA sequence sets.

To identify distinct trends of Ets transcriptional responses downstream of FGF/MAPK signaling, we performed hierarchical clustering of the enrichment z-scores for the Ets family TFBS calculated in the three different ways discussed above. Differential expression of Elk1 between sibling cell types also seems to be an appropriate proxy for Ets family TF activity, so we included it in the clustering. The cell fate bifurcations clustered into 3 distinct classes. The first class represents bifurcation events that do not show enrichment for Elk1 and show little enrichment for Ets family TFBS in the set of genes that differentiate the two sibling cell types. The remaining bifurcations all have strong upregulation of Elk1 expression in one of the sibling cell types, and are enriched for Ets family TFBS in the set of genes that differentiate the two sibling cell types. These bifurcations can be divided into one class that has strong Ets site enrichment in the induced cell itself when comparing genes that are enriched vs depleted in that

specific cell type, and another class where there is little or no such enrichment. Many of this third class instead show Ets site depletion in the uninduced sibling. (Figure 5.9).

Prior studies have examined the role of FGF and other signaling pathways in some but not all of these lineage decisions. For example, all three bifurcations involving the posterior most rows of cells in the neural plate neural plate are thought to directly rely on FGF signaling to promote row I (posterior most row) fate and repress row II (second posterior-most row) fate (Clare Hudson et al., 2007). In our data all these bifurcations show Ets site enrichment in the row I cell types compared to the row two cell types, but only mild Ets site enrichment in the row I cell types comparing upregulated and downregulated genes. We interpret this to mean that Ets mediated transcription plays a role in differentiating the row I and row II cell types but plays less of a role in shaping the overall transcriptional state of the row I cell types. These results are in line with the previous understanding of A-line neural gene regulatory networks, where FGF activity in row I is known to control differences in transcription between rows I and II but is not thought to play a critical role in defining the A-line neural lineage overall.

The bifurcations that differentiate the mesenchyme from muscle at the 64-cell stage are known to be FGF dependent, but how this FGF signal contributes to mesenchymal gene expression is largely unknown (Kim et al., 2007). Using our TFBS enrichment analysis, we show that there is little Ets site enrichment in the genes that are differentially expressed in the mesenchyme/muscle bifurcations at the 64-cell stage, and that Ets sites are not enriched in the genes that are upregulated in each lineage overall. This indicates that the FGF signal necessary for mesenchymal fate in these mesenchyme/muscle bifurcations could either operate indirectly of canonical Ets family TF transcription, or else it could lead to changes in the expression of only a few key genes downstream of Ets.

TFBS enrichment analysis of the transcriptome-wide changes in sibling cell lineages after fate bifurcation implies that the majority of fate bifurcations at these stages rely at least in part on direct input of Ets family TFs, presumably downstream of FGF signals. This includes the bifurcation that establishes the previously undescribed, putative-ventral midline tail epidermis at the mid-gastrula stage. This analysis also implies that the transcriptome-wide changes that occur in several bifurcations rely relatively little on inputs of Ets family TFs. Some of these bifurcations have previously been described to be controlled by the Nodal/Notch relay mechanisms, however the lack of a major Ets enrichment signature in the mesenchyme/muscle bifurcations is unexpected.

SMAD mediated repression of Ets site transcriptional targets may function in medio-lateral patterning of the neural plate

Nodal signaling is transcriptionally mediated through SMAD family TFs. Previous research shows that Nodal signals are responsible for the mediolateral patterning of the *Ciona* neural plate (Clare Hudson & Yasuo, 2005). Interestingly however, one of the strongest TFBS enrichment signatures in the bifurcation between medial and lateral A-line neural siblings is not an enrichment of SMAD family TF sites in the lateral A-line neural plate siblings, but rather a repression of Ets family TF sites in the lateral neural plate siblings (Figure 5.9). There is precedent in other *Ciona* lineages that SMADs acting downstream of TGF-β superfamily signaling molecules can act to repress transcription of Ets family TF targets (Ohta & Satou, 2013). This implies that the Nodal signal that serves to pattern the medial-lateral axis of the A-line neural plate may function at least in part to repress Ets site enriched target genes in lateral cells and not strictly through the induction of directly SMAD-dependent targets.

Analyzing the genome-scale dynamics of cell fate induction

Moving forward, we decided to take advantage of our dataset's wide coverage of cell types and stages to more broadly understand the transcriptional changes underlying cell fate bifurcations. If a gene is transcriptionally upregulated in cell type A compared to its sibling cell type B, there are several possible underlying mechanisms (Figure 5.10 A). It could either be (1) upregulated in daughter A vs the mother cell and unchanged in daughter B vs the mother cell, (2) upregulated in daughter A vs the mother cell and upregulated in daughter B vs the mother cell, but upregulated more in A than in B, (3) upregulated in daughter A vs the mother cell and downregulated in daughter B vs the mother cell (4) unchanged in daughter A vs the mother cell and downregulated in B vs the mother cell, or (5) downregulated in both daughter cells vs the mother cell, but downregulated more in daughter B than in daughter A. To quantify the relative usage of these five mechanisms for divergent gene expression, we explored the expression level changes in "trios" of STAMP clusters involving a mother cell type and its two daughter/sibling cell types.

We found that 37% of TFs that are differentially expressed between sibling cell types in a trio fall into the first category, 35% fall into the second, 16% into the third, 10% into the fourth, and the remaining 2% in the fifth category. (Figure 5.10 B) The largest driver of differential expression between sibling lineages is upregulation in one sibling and not the other, but a surprising fraction of genes were upregulated in both siblings but more so in one than the other. Knowing that the majority of upregulation between daughter clusters is driven by induction of gene expression in one specific daughter, we tested the hypothesis that one could *de novo* determine which daughter cluster in a cell fate bifurcation was the induced cluster. We did this by measuring what percent of total upregulation of differentially expressed (DE) TFs was in each

daughter and found that for the FGF dependent bifurcations measured earlier, this simple metric was able to robustly predict the induced cluster (Figure 5.9). The only exception to this trend is the B7.4 and B7.8 muscle lineages, which had more upregulated TFs than their FGF-dependent mesenchyme and mesenchyme/2˚notochord precursor sibling cell types. Muscle cell fates are known to be driven, however, by asymmetric segregation of a cell-fate determinant (macho-1/Zic-r.a), and these cells could be considered "intrinsically induced".

Newly born cell fates diverge from their sibling fates more quickly at later stages

The distances in gene expression space between sibling cell fates after a bifurcation is widely variable across developmental time and anatomical regions. Some sibling cell types remain fairly close, indicating that gene expression profiles are not drastically changed between siblings. Other bifurcations, such as between the relatively transcriptionally silent B7.6 cell and its sibling blastomere B7.5 are orders of magnitude more distant from each other than other sibling cell pairs at the same stage. This likely reflects maternal cell fate determinants known to segregate as RNA molecules into the B7.6 germ cell precursor downstream of patterning by the CAB. We do however find a consistent trend that at the mid-gastrula stage, the distance between sibling STAMP clusters which have just bifurcated is much larger than the distance between sibling STAMP clusters immediately after bifurcation that split at the 64-cell or 110-cell stage (Figure 5.10 C). This trend is also readily visible by looking at the distance between newly born sibling cluster in UMAPs space at each of the three stages (Figure 5.3 A-C). This indicates that the rate of divergence between sibling clusters in gene expression space is increasing with developmental time, and potentially reflects the establishment of new chromatin states and/or the zygotic expression of a broader set of transcription factors.

The “broad hourglass” model of cell fate specification

The gene regulatory networks surrounding cell fate specification events can be thought of as hourglasses with narrow waists (Figure 5.11 A-B). Upstream of the cell fate specification event, diverse regulatory interactions give rise to some unique combination of lineage-specific transcription factors and signaling states that induces the expression of either a single master regulatory transcription factor unique to that cell type or a small number of tissue-specific transcription factors that define a combinatorial code. Transcriptional cascades acting downstream of that single factor or small set of factors then lead directly or indirectly to changes in the expression of large numbers of downstream genes. There are major questions, however, about how narrow the pinch point of the GRN hourglass actually is as sibling cell states diverge (Figure 5.11 A-B). To address this, we used our scRNAseq dataset to identify all of the transcription factors upregulated in the earliest stages of muscle, mesenchyme and endoderm differentiation as compared to their sibling cell types. We selected these cell types because they formed entire tissues at later stages of development without the dramatic increase in tissue subtypes exhibited in the neural lineages. Notochord is discussed in more detail in a later section but shows similar trends. We observed that in each of these bifurcations, there was not a single master TF differentially expressed in each tissue type, but rather an entire suite of TFs that were differentially expressed at the earliest stages of tissue specification (Figure 5.12 A-C), indicating that the pinch point of the hourglass model may be wider than previously appreciated.

To infer patterns of transient versus stable expression, and to explore more of the temporal expression dynamics of these earliest diverging TFs, we also integrated our scRNAseq dataset of early *Ciona* development with another single-cell RNAseq dataset focused on later *Ciona* stages (C. Cao et al., 2019). We measured the expression level from 64-cell through

hatching larva of the TFs which were upregulated in muscle, mesenchyme and endoderm compared to their sibling cell types at their initial bifurcation. We find that these TFs generally fall into one of two categories: some are expressed for only a short time window whereas others show persistent and/or increasing expression (Figure 5.12 A-C). Functional experiments are needed to determine which transcription factors diverging between sibling cell types have important roles in cell fate specification, but all of the bifurcations we have examined show several transcription factors becoming differentially expressed and not a single putative master regulator.

Many genes besides Brachyury are differentially expressed in the notochord immediately after fate bifurcation

This is the first single-cell RNA seq study to generate a list of DE genes in the *Ciona robusta* notochord compared to its sibling cell fate immediately after cell fate induction at the 64-cell stage. To analyze if these genes were in fact notochord specific, we extracted the average expression value of each of these genes in all of the other cell type STAMP clusters at the 64-cell stage. We found that nearly all of the genes are expressed most strongly in the notochord, but many are also expressed elsewhere in the embryo to varying extents, indicating that they are notochord enriched, but not notochord specific (Figure 5.13 A). An important point from this list of differentially expressed genes is that there are many other non-TF genes that diverge between the 1˚ notochord and their A-neural siblings at the earliest stages. Many of these genes have never been established as notochord enriched at the 64-cell stage and may be effector genes of the earliest stages of the notochord GRN. Further examination of this gene list will be necessary to try and identify genes with important roles in notochord fate induction.

We then measured the expression level over time of the TFs that are upregulated in the primary notochord at the 64-cell stage compared to their A-line neural siblings (Figure 5.13 B). As expected, the key notochord transcription factor Brachyury is upregulated in the notochord. We also found that several other transcription factors were upregulated in the notochord compared to their A-line neural siblings at the 64-cell stage. Some of these such as Mnx and FoxAa are expected, while other such as Zic, Elk, and Hes have not been previously appreciated by *in situ*. Much like in the endoderm, muscle, and mesenchyme, we find that the DE TFs are either expressed strongly in a short time frame around fate induction or are stably expressed and increase their expression over time (Figure 5.13 B).

The notochord exhibits distinct waves of transcription

To further characterize the temporal dynamics of the *Ciona* notochord GRN, we created a list of all the genes which are enriched in the notochord compared to other non-notochord tissues at a given developmental stage and measured the expression level of these genes over time. We found that the temporal expression patterns of these notochord enriched genes show distinct waves of transcription (Figure 5.14 A-B). Distinct temporal expression profiles have previously been identified by in situ hybridization for select notochord genes, but until now we have not been able to identify distinct suites of genes that co-vary in expression in the notochord over time. We hypothesized that these transcriptional waves are likely to be controlled by distinct TFs, or combinations of TFs acting in a differentiation cascade. To begin testing this hypothesis, we examined the temporal expression patterns of notochord enriched TFs over time and found that, similar to the entire set of notochord enriched genes, there are distinct temporal waves of expression of notochord enriched TFs. Intriguingly, we observe that the waves of TF expression in the notochord involve suites of multiple co-varying TFs and not single genes. This raises the

possibility that the *Ciona* notochord GRN is much more complicated than previously expected as not only is the pinch point of notochord induction wider than previously understood, but the TFs which control subsequent transcriptional transitions may also act in complex sets and not as single regulators. Much more future work will be needed to dissect this new GRN structure and attempt to understand if these waves of transcription coincide with, and possibly contribute to the control of distinct morphogenetic events such as mediolateral intercalation and notochord elongation.

The earliest *Ciona* notochord GRN is wider than previously proposed

As there are multiple TFs other than Brachyury enriched in the 1˚ notochord compared to its sibling cell type at the time of notochord induction, we hypothesized that TFBS enrichment might provide useful information about their roles in notochord gene expression. Using our scRNAseq dataset integrated with the overlapping Cao et al dataset, we again performed TFBS enrichment analysis to identify which TF family binding sites are most enriched in the notochord compared to other cell types at each stage. Our assumption from the current understanding of the notochord GRN is that the earliest expression should be enriched for binding sites of the notochord-specific TF Brachyury. Interestingly, we find that the earliest targets are not enriched for Brachyury sites, but are actually enriched for sites of Zic and Ets family TFs (Figure 5.15 A), which are known to be direct upstream activators of Brachyury expression in the notochord. Brachyury sites do not become enriched in notochord-enriched genes until considerably later in development, suggesting that there is a significant lag time between when it is first detectable at the RNA level by in situ at the 64-cell stage and when it becomes a major driver of notochord gene expression. This supports the hypothesis that most early notochord genes are initially induced directly downstream of FGF, in parallel to and not downstream of the key notochord

regulator Brachyury. In further support of this, we see very little overlap between the genes differentially expressed in the notochord at the 64-cell stage and those induced by ectopic expression of Brachyury in other studies (Figure 5.14 5). We also see that FoxAa has a U-shaped TFBS enrichment profile over time, consistent with a role in a recently described feedforward network as both both an upstream regulator of Bra expression and a major regulator of notochord-specific gene expression at later stages (Figure 5.14 5) (Reeves et al 2020).

The fact that there are multiple TFs in the notochord as well as nearly 100 putative effector genes that are differentially upregulated in the notochord immediately after fate bifurcation, and that targets of the earliest notochord GRN are enriched for Ets/Zic, but not Brachyury sites indicates that the notochord also exhibits a wide hourglass GRN at the time of fate restriction. This is opposed to previous views that Brachyury would be the only differentially upregulated gene at the pinch point. This supports other work showing that Brachyury is likely not a unitary "master regulator" of notochord fate in *Ciona* (W. M. Reeves et al., 2020) as had previously been believed (Hotta et al., 1999; Takahashi et al., 1999; Yasuo & Satoh, 1998).

Conclusions

New findings from experimental approach

Here I have presented our results from whole embryo scRNAseq of the invertebrate chordate *Ciona* including a targeted perturbation of FGF/MAPK signaling. We found that a modest number of whole-embryo scRNAseq experiments has the power to recapitulate many, but not all, of the findings from years of classical developmental biology experiments. Furthermore, the quantitative nature of scRNAseq allowed us to uncover previously undescribed transcriptional states during early *Ciona* development. These new transcriptional states may be important for understanding patterning of the b-line neural lineages as well as understanding the transcriptional cascades necessary for mediolateral pattering of the future tail epidermis.

scRNAseq is a powerful technology, but also has its shortcomings. The sensitivity of scRNAseq to lowly-expressed genes is a known issue, and there were instances in our data where we were not able to recapitulate gene-expression patterns that have been demonstrate by *in situ* hybridization. This issue is partially addressed by increasing the sequencing coverage on a per-cell-type basis. In order to obtain enough cells to achieve increased coverage, especially at the early stages of *Ciona* development, multiple *Ciona* adults can be used. However, as we demonstrate this introduces a new source of mother-of-origin variability. In this study we introduced a method for removing these effects post hoc by identifying the mother-of-origin for each STAMP using SNPs. This method will increase the feasibility of scRNAseq in other stages of *Ciona* development and may possibly be extended to other non-traditional models. However, this method relies on large cell numbers from each adult for accurately clustering. We propose that this method could also be improved by genomic sequencing of the adults used in an experiment to directly link STAMP profiles with an adult and verify relationships between

STAMPs. It is also possible that with deep enough sequencing on a per-stamp basis, this method could be extended to identify unique embryo clusters and dissect variability on a per embryo basis.

An entirely unexplored area of this dataset is the functional role of the observed SNPs. There are interesting relationships to be explored, both between and within cell types, between transcript levels and natural genetic variation in this highly polymorphic species. The scRNAseq technology we used results in sequences of ~100 bp at the 3' end of the transcript molecule. Therefore, our observed SNPs tend to fall in the 3' UTR of most transcripts. While this makes inferences about the functional role of SNPs in protein structure difficult, it does allow us to investigate possible roles for 3' UTR regulation of gene expression including regulation by miRNAs. On a more practical level, one of the current limiting factors for the number of cells one is able to encapsulate and profile using droplet-based technologies is doublet formation resulting from encapsulation of two cells with a single RNA capture bead. Profiling the SNPs in each STAMP holds the possibility to *post hoc* identify cell doublets. This would allow for greater cell numbers to be loaded into droplet-based scRNAseq instruments, which results in a dramatic increase in profiled singlets, but only a modest increase in profiled doublets which could be removed computationally.

Broad hourglass model of cell-type GRNs

Here we demonstrate how the GRNs that control multiple tissue lineages in *Ciona* are more complex that previously appreciated. A commonly held view is that much of cell fate induction is controlled by upstream factors driving expression of tissue specific master regulator or lineage selector TFs which then induce downstream effector genes. In opposition to this view, we show that at the earliest stages of cell type restriction there are entire suites of transcription

factors along with multiple putative effector genes that are differentially expressed between diverging cell types. In the primary notochord, we show that some of the putative effectors of the notochord GRN are likely not downstream of the tissue-specific TF Brachyury, but rather are targets of the upstream factors Zic and Ets and are expressed in parallel with Brachyury.

It remains to be seen how common this trend is among other tissue types and in other organisms. It implies that GRNs in general are much more complicated than previously described. Because of this, it may be insufficient to use a reductionist approach to dissect the regulatory mechanisms of GRNs by inhibiting or reducing the activity of a single transcription factor and measuring the resulting changes levels of effector genes. Instead, more integrative approaches may be required. This wide hourglass model may also provide a framework to think about the evolvability of GRNs. Cell fate bifurcations that involve the simultaneous induction of multiple TFs and many effector genes are potentially more robust to environmental perturbations and stochastic transcriptional noise than those involving a single putative master regulator, but it is not clear if they would be more or less evolvable. Arguably, they might buffer against major phenotypic changes while providing more scope for mutations of small effect.

Brachyury expression outside of the notochord

Brachyury is an essential regulator of notochord fate in all chordates, including *Ciona*. As expected, we found that Brachyury was one of the most enriched transcription factors in primary notochord cells compared to their A-neural siblings. Unexpectedly, however, we also saw Brachyury expression in other lineages. The secondary notochord lineage first becomes fate-restricted to notochord in B8.6, but we saw considerable Bra expression in its parent, B7.3, and also to a smaller degree in its sibling B8.5. Bra expression in B7.3 is seen in some but not all published *in situ* patterns, so this was not entirely unexpected. It may represent an example of

mixed lineage transcriptional priming. Much more unexpectedly, however, we detected modest but statistically significant Brachyury upregulation in the row I column 3 A-line neural plate cells at the mid-gastrula stage compared to their row II sibling cell fate. These cells are similar to notochord in that they express FoxA, Zic and have have high MAPK activity. In vertebrate embryos, Brachyury has complex roles in posterior neuromesodermal precursors distinct from its role in the notochord. Brachyury mutant and knockdown embryos do not show an obvious neural tube defect, but we speculate that this expression domain might represent a vestigial remnant of an ancestral role in tail neuromesodermal lineages. This group of cells is fate-restricted to lateral tail nerve cord, but the A6.2/A6.4 lineage overall gives rise to a complex mixture of neural and mesodermal fates.

Cryptic transcriptional subtypes of notochord

My earlier project identifying distinct patterns and mechanisms of unequal cleavage in the notochord lineage identified unexpectedly distinct cell behaviors between the four primary notochord founder cell pairs (Winkley et al., 2019). One of the motivations for our scRNAseq project was to test whether these 4 different founder cells established transcriptionally distinct subtypes of notochord cell. We have not detected evidence of that in our current dataset. The primary notochord cells form a single cluster at all three stages examined. It is possible, however, that cryptic transcriptional differences between them might exist that could be detected with a larger dataset of sequenced notochord cells and/or greater sequencing depth.

There is evidence that several genes in the notochord of *Ciona* exhibit graded expression patterns at various stages (Harder et al., 2018; W. Reeves et al., 2014), and it is unknown if these gradients are derived from differences in expression level between sub-lineages of notochord cells. It is not entirely clear how the algorithms that underlie the non-linear dimensional

reduction and clustering functions in Seurat would handle genes expressed in gradients, and different analysis methods may provide insight into a possible sub-lineage transcriptional structure of the notochord without requiring additional data.

Role of FGF in mesenchyme/muscle bifurcations

Using our TFBS enrichment analysis, we found that the lineage bifurcations between mesenchyme and muscle at the 64-cell stage do not show a major signature of Ets mediated transcription. This leaves open the question about what mechanisms may be necessary to promote mesenchyme fate over muscle fate in the B7.3 and B7.7 blastomeres. Transcription of muscle related genes in the B7.4 and B7.8 blastomeres is known to be downstream of the cell fate determinant macho-1/zic-r.a, and studies in *Halocynthia* demonstrate that transplantation of the FGF expressing cells that typically contact the mesenchyme precursors to instead contact the muscle precursors leads to expression of some mesenchymal genes in B7.4 and B7.8. This suggests that signals from these FGF expressing cells are not solely repressing macho-1 directed transcription but are actively promoting expression of mesenchyme markers. This is consistent with multiple hypotheses about the mechanisms of action of FGF. One possibility is that FGF largely acts to repress macho-1 mediated transcription, but there is a secondary, unknown signal emanating from these B-line endodermal blastomeres which promotes expression of mesenchymal genes. An alternative hypothesis is that FGF functions to both repress macho-1 mediated transcription and promote expression of mesenchymal genes, but not through large-scale canonical Ets mediated transcription.

Transcriptional waves in the notochord

Here we observed that the temporal dynamics of expression of notochord enriched genes show signs of distinct waves of co-varying genes. Throughout development, the notochord

undergoes several large-scale morphogenetic events including patterned rounds of asymmetric division, mediolateral intercalation, notochord cell elongation, notochord sheath development, and notochord lumen formation. For some of these processes, previous studies have provided insight about necessary expression of key genes such as Planar Cell Polarity pathway components for mediolateral intercalation and notochord lumen formation. These transcriptional waves could provide a much-needed comprehensive insight into the GRN controlling the differentiation and morphogenesis of this organ. Network analyses of co-varying gene expression profiles along with TF expression and TFBS enrichment provide an entry point to building temporally dynamic GRN models. Gene Ontology enrichment analysis might provide links between the suites of genes in the different waves of expression and specific morphogenetic processes. These types of analyses combined with functional genomic perturbations and single-cell resolution analysis of cellular behaviors are feasible in an organ comprised of only 40 cells and would lay the groundwork for understanding how GRNs might direct morphogenesis in more complex systems.

Materials & Methods

Ciona

Wild caught *Ciona robusta* (formerly *Ciona intestinalis* type A) were purchased from Marine Research and Educational Products (MREP, San Diego). Animals were housed in a recirculating artificial seawater aquarium at 18˚C under constant light until experimental use.

Experimental setup

An independent fertilization, dechorionation, drug treatment, dissociation, encapsulation, and library prep was performed to obtained data for each of the 64-cell, 110-cell, and mid-gastrula stages.

Fertilization, dechorionation and embryo culture

Fertilization and dechorionation was performed according to standard protocols (Veeman et al., 2011). Eggs and sperm were collected from adults, eggs were washed and inseminated, and then left to fertilized for 5 minutes. Follow the fertilization period, the fertilized eggs were placed into dechorionation solution and gently pipetted to remove the follicle cells and chorion. Once dechorionation was complete, the eggs were washed 4 times in ASW with 0.1% BSA. Embryos were placed in an incubator at ~18˚C and development was tracked using timelapse microscopy. Embryos were staged according to (Hotta et al., 2007).

Drug treatment

Embryos were with the MEK inhibitor U0126 from the 16-cell stage onward at a concentration of 4µM. At the desired stage, a 1000X stock of 4mM U0126 in DMSO was added to the culture dishes to give a final concentration of 4µM. Control embryos were treated with 0.1% DMSO at the same time as drug treated embryos.

Dissociation

Embryos were harvested at the desired stage in a 1.5 mL microcentrifuge tube that had been treated with 1% BSA in ASW. Embryos were spun at 700X g for 30 seconds and the supernatant was removed. They were then washed twice with room temp Calcium-Magnesium Free AWS (CMF-ASW). Dissociation was performed by gentile pipetting of embryos in a cold 0.1% BSA/CMF-ASW with 1% trypsin for 2 minutes. Following dissociation, the embryos were washed twice using cold 0.1% BSA/CMF-ASW, filtered through a 40 µm strainer and washed once more. Embryos were then resuspended in cold 0.1% BSA/CMF-ASW, counted on a Neubauer-Improved hemocytometer, and diluted to a concentration of 250,000 cells/mL. A small subsample of embryos from each collection was fixed in 2% paraformaldehyde to confirm staging and embryo quality by confocal microscopy.

Encapsulation and RNA capture

Microfluidic encapsulation of single cells with barcoded beads was performed on the Dolomite Nadia instrument (Dolomite Bio, Royston UK) with a 2-lane encapsulation chip. One lane on each chip was used for the DMSO control and one for the U0126-treated sample. We used the standard Nadia protocol (v1.8) and their filter-based emulsion breaking protocol. The capture beads and chemistry used in this protocol are essentially the same as in (Macosko et al., 2015) and use a stringent lysis buffer and reverse transcription after emulsion breaking. The beads are coated with oligos that incorporate a poly(T) sequence to capture mRNA 3’ ends and also two barcode sequences. One is a cell barcode that is shared between every oligo on a given bead. The other is a short Unique Molecular Identifier (UMI) barcode that differs between oligos on each bead and is used to correct for PCR duplicates in each sequenced library.

Library Preparation and sequencing

After RNA captured on barcoded beads and the emulsion broken, reverse transcription, exonuclease treatment, and PCR were performed according to the dolomite protocols. Sequencing libraries were generated using the Illumina Nextera XT kit and library quality was assessed using the Agilent Bioanalyzer. Sequencing was performed on an Illumina NextSeq 500 at the KSU Integrated Genomics Facility. For all sequencing runs, an Illumina High-output 150 cycle kit was used with read lengths of: 26 bp for the Cell barcode/UMI read, 8 bp for the i7 index read, and 116 bp for the transcript read. The DMSO and U0126 libraries from each timepoint were sequenced together as a separate sequencing run. The 64-cell DMSO and U0126 libraries composed 95% of the pooled sequencing library, the 110-cell DMSO and U0126 libraries composed 100% of the pooled sequencing library, and the mid-gastrula DMSO and U0126 libraries composed 75% of the pooled sequencing library.

Sequence alignment and demultiplexing

Following sequencing, the dropSeqPipe pipeline was used to align reads to the genome, count individual UMIs and assign them to STAMPs.

SNP analysis

The GATK best-practices pipeline for variant calling in single-cell RNAseq data was used to call SNPs across the entire genome for all STAMPs. The VCFtools package was used to calculate a relatedness statistic (unadjusted Ajk statistic based on (Yang et al., 2010)) between all pairwise STAMP comparisons in controls and drug treated embryos at each stage. The resulting distance matrix was clustered using the cluster module of the python Scipy package.

Dimensional reduction, clustering, and cluster analysis

Dimensionality reduction, clustering and further downstream analysis were performed using Seurat.v3. For all timepoints, the default parameters for data normalization and variable feature selection were used. Each timepoint was then scaled and centered and the effects due to different mothers-of-origin were regressed out. Linear dimensional reduction was preformed using PCA, and the number of PCs to keep for downstream clustering and non-linear dimensional reduction was determined by the modified Jackstraw Procedure. Specific PC's for analysis are as follows: DMSO 64-cell – 25 pcs, U0126 64-cell – 20 pcs, DMSO & U0126 64-cell - 30 pcs, DMSO 110-cell – 30 pcs, U0126 110-cell – 25 pcs, DMSO & U0126 110-cell - 35 pcs, DMSO mid-gastrula – 35 pcs, U0126 mid-gastrula – 25 pcs, DMSO & U0126 mid-gastrula - 40 pcs, DMSO & U0126 all stages – 50 pcs.

TFBS analysis

TFBS analysis was performed similar to (W. M. Reeves et al., 2020). Control and target sequence sites were determined using the FindMarkers function implemented in Seurat to find statically significantly up and downregulated genes as desired. To extract putative enhancer regions from these gene models, we extracted the 1,500 bp of sequence upstream of the transcription start site. Additionally, we intersected these upstream regions with whole-embryo ATACseq peaks from previous experiments and kept the entire sequence of any peak that was overlapping the 1,500 bp upstream for a gene model. These sets of sequences were then saved as fasta files and used as the input for TFBS site calling and enrichment testing using the oPOSSUM3 command line-tools with default settings and the JASPAR2020 vertebrate core PWMs.

References – Chapter 5

Bertrand, V., Hudson, C., Caillol, D., Popovici, C., & Lemaire, P. (2003). Neural Tissue in Ascidian Embryos Is Induced by FGF9/16/20, Acting via a Combination of Maternal GATA and Ets Transcription Factors. *Cell*, *115*(5), 615–627. https://doi.org/10.1016/S0092-8674(03)00928-0

Brozovic, M., Dantec, C., Dardaillon, J., Dauga, D., Faure, E., Gineste, M., Louis, A., Naville, M., Nitta, K. R., Piette, J., Reeves, W., Scornavacca, C., Simion, P., Vincentelli, R., Bellec, M., Aicha, S. Ben, Fagotto, M., Guéroult-Bellone, M., Haeussler, M., Jacox, E., Lowe, E. K., Mendez, M., Roberge, A., Stolfi, A., Yokomori, R., Brown, C. T., Cambillau, C., Christiaen, L., Delsuc, F., Douzery, E., Dumollard, R., Kusakabe, T., Nakai, K., Nishida, H., Satou, Y., Swalla, B., Veeman, M., Volff, J.-N., & Lemaire, P. (2018). ANISEED 2017: extending the integrated ascidian database to the exploration and evolutionary comparison of genome-scale datasets. *Nucleic Acids Research*, *46*(D1), D718–D725. https://doi.org/10.1093/nar/gkx1108

Cao, C., Lemaire, L. A., Wang, W., Yoon, P. H., Choi, Y. A., Parsons, L. R., Matese, J. C., Wang, W., Levine, M., & Chen, K. (2019). Comprehensive single-cell transcriptome lineages of a proto-vertebrate. *Nature*, *571*(7765), 349–354. https://doi.org/10.1038/s41586-019-1385-y

Cao, J., Spielmann, M., Qiu, X., Huang, X., Ibrahim, D. M., Hill, A. J., Zhang, F., Mundlos, S., Christiansen, L., Steemers, F. J., Trapnell, C., & Shendure, J. (2019). The single-cell transcriptional landscape of mammalian organogenesis. *Nature*, *566*(7745), 496–502. https://doi.org/10.1038/s41586-019-0969-x

Gainous, T. B., Wagner, E., & Levine, M. (2015). Diverse ETS transcription factors mediate FGF signaling in the Ciona anterior neural plate. *Developmental Biology*, *399*(2), 218–225. https://doi.org/10.1016/j.ydbio.2014.12.032

Harder, M., Reeves, W., Byers, C., Santiago, M., & Veeman, M. (2018). Multiple inputs into a posterior-specific regulatory network in the Ciona notochord. *Developmental Biology*, *448*(2), 136–146. https://doi.org/10.1016/j.ydbio.2018.09.021

Hotta, K., Mitsuhara, K., Takahashi, H., Inaba, K., Oka, K., Gojobori, T., & Ikeo, K. (2007). A web-based interactive developmental table for the ascidian Ciona intestinalis, including 3D real-image embryo reconstructions: I. From fertilized egg to hatching larva. *Developmental Dynamics : An Official Publication of the American Association of Anatomists*, *236*(7), 1790–1805. https://doi.org/10.1002/dvdy.21188

Hotta, K., Takahashi, H., Erives, A., Levine, M., & Satoh, N. (1999). Temporal expression patterns of 39 Brachyury-downstream genes associated with notochord formation in the Ciona intestinalis embryo. *Development Growth and Differentiation*, *41*(6), 657–664. https://doi.org/10.1046/j.1440-169X.1999.00467.x

Hudson, C. (2002). A conserved role for the MEK signalling pathway in neural tissue

specification and posteriorisation in the invertebrate chordate, the ascidian Ciona intestinalis. *Development*, *130*(1), 147–159. https://doi.org/10.1242/dev.00200

Hudson, Clare, Kawai, N., Negishi, T., & Yasuo, H. (2013). β-Catenin-driven binary fate specification segregates germ layers in ascidian embryos. *Current Biology : CB*, *23*(6), 491–495. https://doi.org/10.1016/j.cub.2013.02.005

Hudson, Clare, & Lemaire, P. (2001). Induction of anterior neural fates in the ascidian Ciona intestinalis. *Mechanisms of Development*, *100*(2), 189–203. https://doi.org/10.1016/S0925-4773(00)00528-1

Hudson, Clare, Lotito, S., & Yasuo, H. (2007). Sequential and combinatorial inputs from Nodal, Delta2/Notch and FGF/MEK/ERK signalling pathways establish a grid-like organisation of distinct cell identities in the ascidian neural plate. *Development (Cambridge, England)*, *134*(19), 3527–3537. https://doi.org/10.1242/dev.002352

Hudson, Clare, Sirour, C., & Yasuo, H. (2016). Co-expression of Foxa.a, Foxd and Fgf9/16/20 defines a transient mesendoderm regulatory state in ascidian embryos. *ELife*, *5*, 1–17. https://doi.org/10.7554/eLife.14692

Hudson, Clare, & Yasuo, H. (2005). Patterning across the ascidian neural plate by lateral Nodal signalling sources. *Development (Cambridge, England)*, *132*(6), 1199–1210. https://doi.org/10.1242/dev.01688

Hudson, Clare, & Yasuo, H. (2006). A signalling relay involving Nodal and Delta ligands acts during secondary notochord induction in Ciona embryos. *Development (Cambridge, England)*, *133*(15), 2855–2864. https://doi.org/10.1242/dev.02466

Ilsley, G. R., Suyama, R., Noda, T., Satoh, N., & Luscombe, N. M. (2020). Finding cell-specific expression patterns in the early Ciona embryo with single-cell RNA-seq. *Scientific Reports*, *10*(1), 1–10. https://doi.org/10.1038/s41598-020-61591-1

Imai, K. S. (2004). Gene expression profiles of transcription factors and signaling molecules in the ascidian embryo: towards a comprehensive understanding of gene networks. *Development*, *131*(16), 4047–4058. https://doi.org/10.1242/dev.01270

Imai, K. S. (2006). Regulatory Blueprint for a Chordate Embryo. *Science*, *312*(5777), 1183–1187. https://doi.org/10.1126/science.1123404

Imai, K., Takada, N., Satoh, N., & Satou, Y. (2000). (Beta)-Catenin Mediates the Specification of Endoderm Cells in Ascidian Embryos. *Development (Cambridge, England)*, *127*(14), 3009–3020. http://www.ncbi.nlm.nih.gov/pubmed/10862739

Imai, Kaoru S. (2003). Isolation and characterization of beta-catenin downstream genes in early embryos of the ascidian Ciona savignyi. *Differentiation; Research in Biological Diversity*, *71*(6), 346–360. https://doi.org/10.1046/j.1432-0436.2003.7106001.x

Imai, Kaoru S., Hudson, C., Oda-Ishii, I., Yasuo, H., & Satou, Y. (2016). Antagonism between

β-catenin and Gata.a sequentially segregates the germ layers of ascidian embryos. *Development (Cambridge, England)*, *143*(22), 4167–4172. https://doi.org/10.1242/dev.141481

Kim, G. J., Kumano, G., & Nishida, H. (2007). Cell fate polarization in ascidian mesenchyme/muscle precursors by directed FGF signaling and role for an additional ectodermal FGF antagonizing signal in notochord/nerve cord precursors. *Development*, *134*(8), 1509–1518. https://doi.org/10.1242/dev.02825

Kondoh, K., Kobayashi, K., & Nishida, H. (2003). Suppression of macho-1-directed muscle fate by FGF and BMP is required for formation of posterior endoderm in ascidian embryos. *Development*, *130*(14), 3205–3216. https://doi.org/10.1242/dev.00521

Macosko, E. Z., Basu, A., Satija, R., Nemesh, J., Shekhar, K., Goldman, M., Tirosh, I., Bialas, A. R., Kamitaki, N., Martersteck, E. M., Trombetta, J. J., Weitz, D. A., Sanes, J. R., Shalek, A. K., Regev, A., & McCarroll, S. A. (2015). Highly Parallel Genome-wide Expression Profiling of Individual Cells Using Nanoliter Droplets. *Cell*, *161*(5), 1202–1214. https://doi.org/10.1016/j.cell.2015.05.002

Madgwick, A., Magri, M. S., Dantec, C., Gailly, D., Fiuza, U. M., Guignard, L., Hettinger, S., Gomez-Skarmeta, J. L., & Lemaire, P. (2019). Evolution of embryonic cis-regulatory landscapes between divergent Phallusia and Ciona ascidians. *Developmental Biology*, *448*(2), 71–87. https://doi.org/10.1016/j.ydbio.2019.01.003

Nishida, H. (1987). Cell lineage analysis in ascidian embryos by intracellular injection of a tracer enzyme. III. Up to the tissue restricted stage. *Developmental Biology*, *121*(2), 526–541. https://doi.org/10.1126/science.725606

Nishida, H., & Satoh, N. (1983). Cell lineage analysis in ascidian embryos by intracellular injection of a tracer enzyme. I. Up to the eight-cell stage. *Developmental Biology*, *99*(2), 382–394. https://doi.org/10.1016/0012-1606(87)90188-6

Nishida, H., & Satoh, N. (1985). Cell lineage analysis in ascidian embryos by intracellular injection of a tracer enzyme. II. The 16- and 32-cell stages. *Developmental Biology*, *110*(2), 440–454. https://doi.org/10.1016/0012-1606(87)90188-6

Ohta, N., & Satou, Y. (2013). Multiple Signaling Pathways Coordinate to Induce a Threshold Response in a Chordate Embryo. *PLoS Genetics*, *9*(10). https://doi.org/10.1371/journal.pgen.1003818

Pasini, A., Amiel, A., Rothbächer, U., Roure, A., Lemaire, P., & Darras, S. (2006). Formation of the ascidian epidermal sensory neurons: Insights into the origin of the chordate peripheral nervous system. *PLoS Biology*, *4*(7), 1173–1186. https://doi.org/10.1371/journal.pbio.0040225

Picco, V., Hudson, C., & Yasuo, H. (2007). Ephrin-Eph signalling drives the asymmetric division of notochord/neural precursors in Ciona embryos. *Development*, *134*(8), 1491–1497. https://doi.org/10.1242/dev.003939

Reeves, W. M., Shimai, K., Winkley, K. M., & Veeman, M. T. (2020). Brachyury controls Ciona notochord fate as part of a feedforward network and not as a unitary master regulator. *BioRxiv* , 1–42. https://doi.org/10.1101/2020.05.29.124024

Reeves, W. M., Wu, Y., Harder, M. J., & Veeman, M. T. (2017). Functional and evolutionary insights from the Ciona notochord transcriptome. *Development*, *144*(18), 3375–3387. https://doi.org/10.1242/dev.156174

Reeves, W., Thayer, R., & Veeman, M. (2014). Anterior-posterior regionalized gene expression in the Ciona notochord. *Developmental Dynamics*, *243*(4), 612–620. https://doi.org/10.1002/dvdy.24101

Rothbächer, U., Bertrand, V., Lamy, C., & Lemaire, P. (2007). A combinatorial code of maternal GATA, Ets and beta-catenin-TCF transcription factors specifies and patterns the early ascidian ectoderm. *Development (Cambridge, England)*, *134*(22), 4023–4032. https://doi.org/10.1242/dev.010850

Sardet, C., Paix, A., Prodon, F., Dru, P., & Chenevert, J. (2007). From oocyte to 16-cell stage: Cytoplasmic and cortical reorganizations that pattern the ascidian embryo. *Developmental Dynamics*, *236*(7), 1716–1731. https://doi.org/10.1002/dvdy.21136

Shi, W., & Levine, M. (2008). Ephrin signaling establishes asymmetric cell fates in an endomesoderm lineage of the Ciona embryo. *Development (Cambridge, England)*, *135*(5), 931–940. https://doi.org/10.1242/dev.011940

Takahashi, H., Hotta, K., Erives, A., Di Gregorio, A., Zeller, R. W., Levine, M., & Satoh, N. (1999). Brachyury downstream notochord differentiation in the ascidian embryo. *Genes and Development*, *13*(12), 1519–1523. https://doi.org/10.1101/gad.13.12.1519

Veeman, M. T., Chiba, S., & Smith, W. C. (2011). Ciona Genetics. In F. J. Pelegri (Ed.), *Methods in molecular biology (Clifton, N.J.)* (Vol. 770, pp. 401–422). Humana Press. https://doi.org/10.1007/978-1-61779-210-6_15

Waddington, C. H. (1957). The strategy of the genes; a discussion of some aspects of theoretical biology. In *London: Allen & Unwin*. Allen & Unwin.

Winkley, K., Ward, S., Reeves, W., & Veeman, M. (2019). Iterative and Complex Asymmetric Divisions Control Cell Volume Differences in Ciona Notochord Tapering. *Current Biology : CB*, *29*(20), 3466-3477.e4. https://doi.org/10.1016/j.cub.2019.08.056

Yang, J., Benyamin, B., McEvoy, B. P., Gordon, S., Henders, A. K., Nyholt, D. R., Madden, P. A., Heath, A. C., Martin, N. G., Montgomery, G. W., Goddard, M. E., & Visscher, P. M. (2010). Common SNPs explain a large proportion of the heritability for human height. *Nature Genetics*, *42*(7), 565–569. https://doi.org/10.1038/ng.608

Yasuo, H., & Hudson, C. (2007). FGF8/17/18 functions together with FGF9/16/20 during formation of the notochord in Ciona embryos. *Developmental Biology*, *302*(1), 92–103. https://doi.org/10.1016/j.ydbio.2006.08.075

Yasuo, H., & Satoh, N. (1998). Conservation of the developmental role of Brachyury in notochord formation in a Urochordate, the ascidian Halocynthia roretzi. *Developmental Biology, 200*(2), 158–170. https://doi.org/10.1006/dbio.1998.8958

Figures – Chapter 5

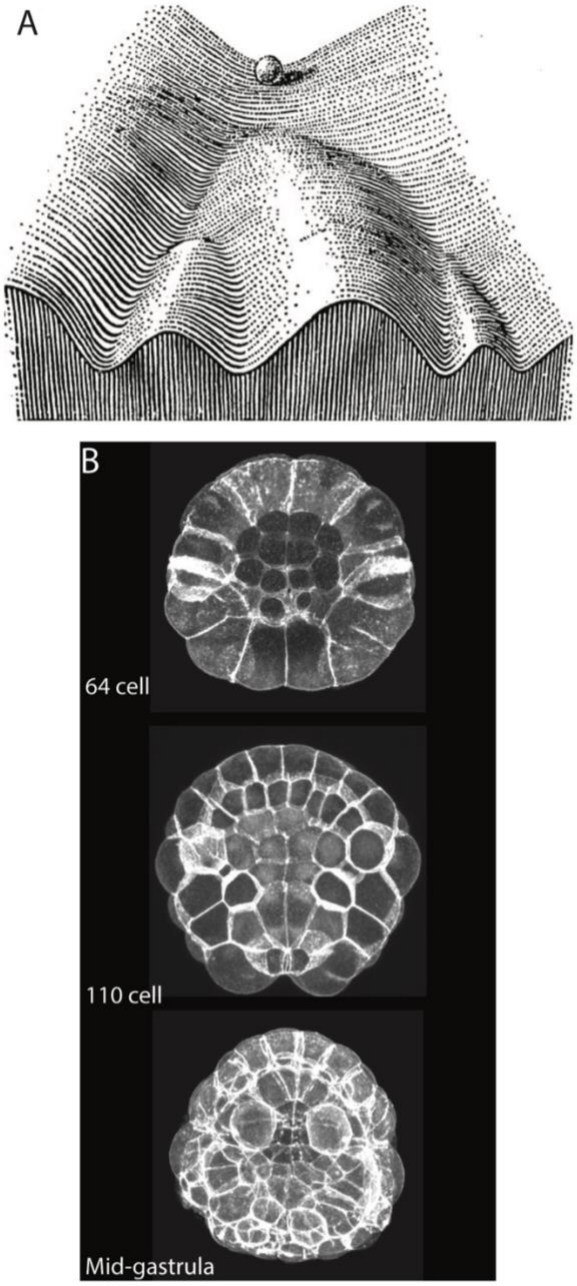

Figure 5.1 Cell fate bifurcations and *Ciona* staging.

(A) Waddington's epigenetic developmental landscape depicts the cell fate bifurcation events that occur during development as a ball rolling down a hill that repeatedly makes choices of one trajectory instead of another (Waddington, 1957). (B) Max intensity projections through selected confocal z-planes of phalloidin stained embryos collected at the time of harvest for each developmental stage analyzed by scRNAseq.

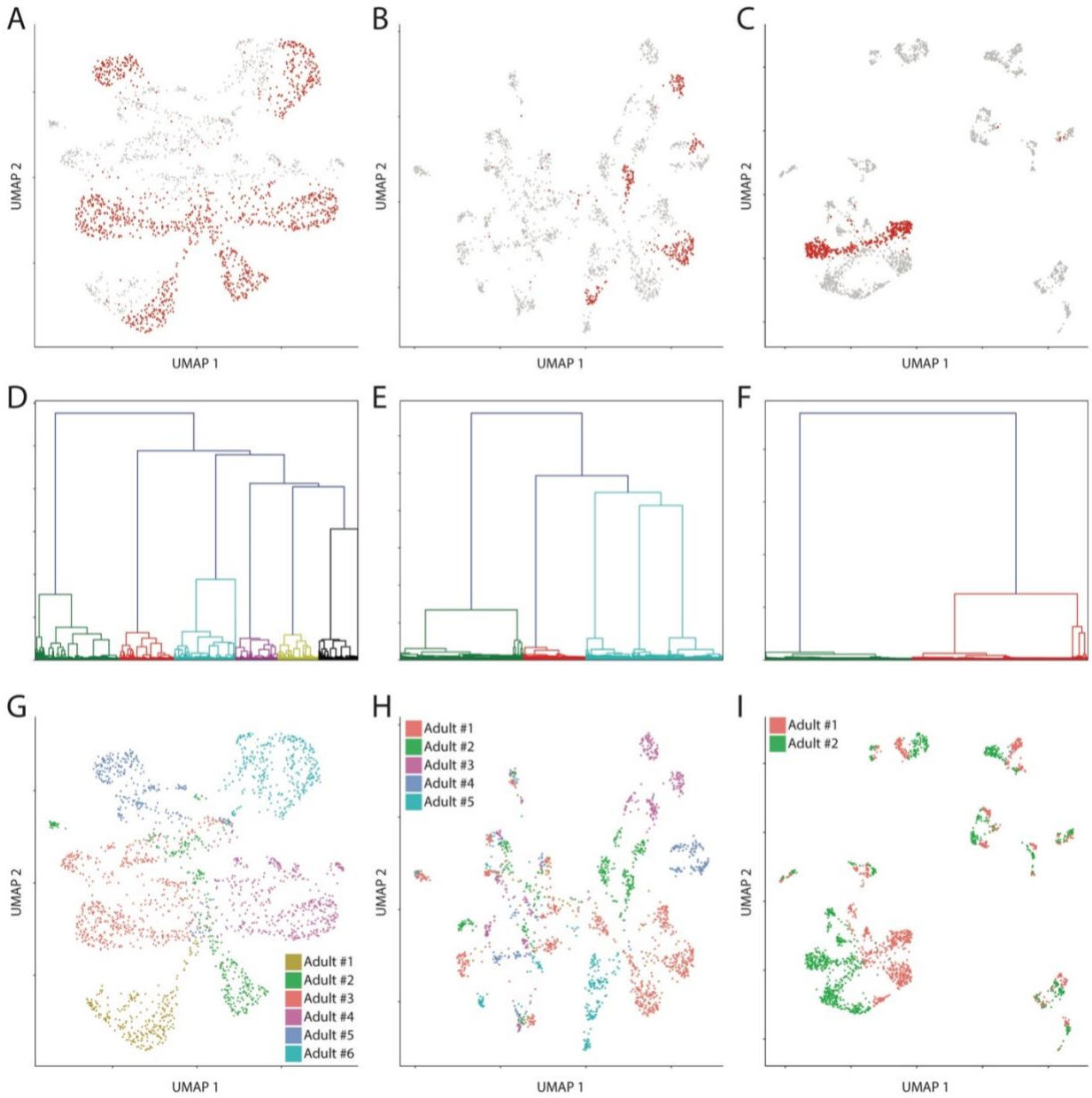

Figure 5.2 Mother-of-origin effect drives single-cell transcriptome variability at early stages.

(A-C) First-pass UMAP plots of STAMPs from the (A) 64-cell, (B) 110-cell, and (C) mid-gastrula stages highlighting the animals cells in A, and the anterior epidermis in B and C. Based on previous literature, these cell types should form a single cluster at each stage. (D-F) Dendrograms of relatedness between STAMPs as determined by SNP variants for the (D) 64-cell, (E) 110-cell, and (F) mid-gastrula stages. (G-I) UMAP plots of STAMPs from the (G) 64-cell, (H)110-cell, and (I) mid-gastrula stages showing the predicted mother-of-origin for each STAMP.

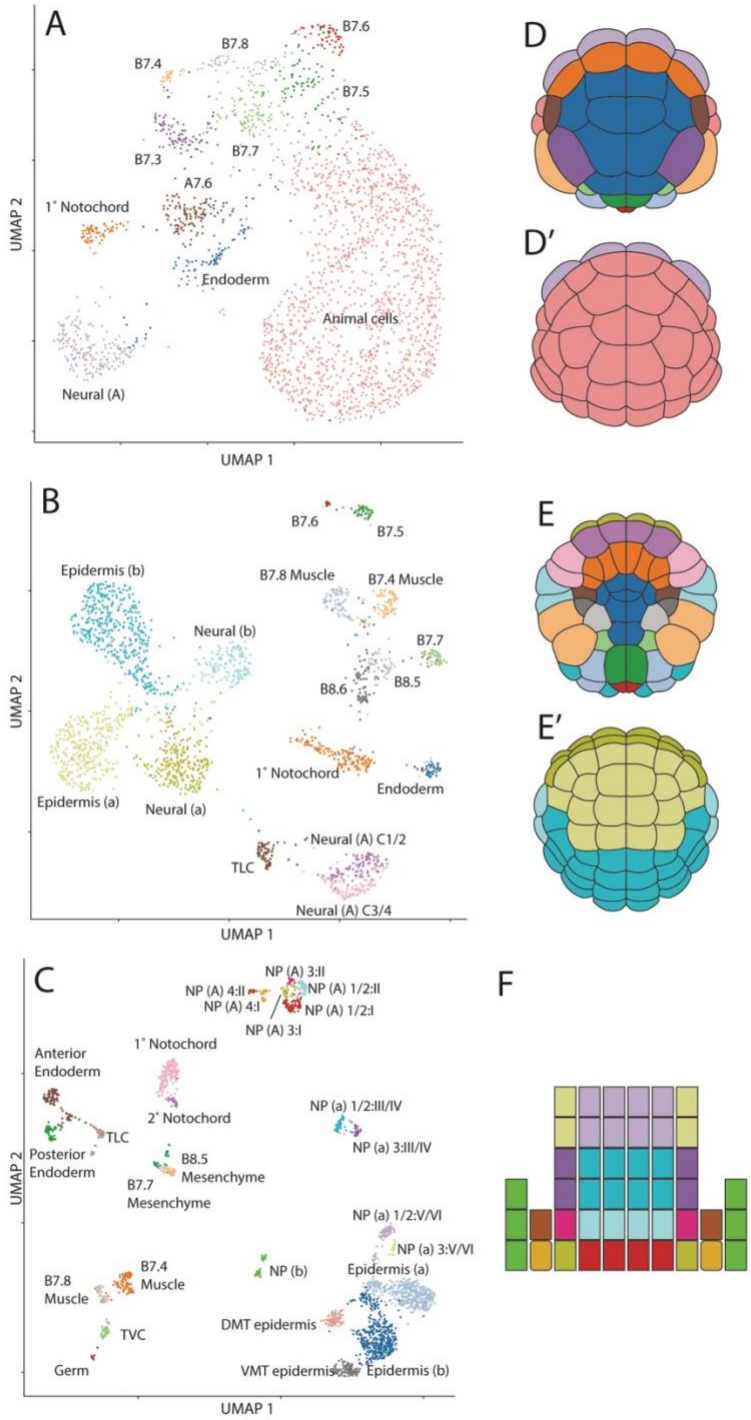

Figure 5.3 Mother-of-origin corrected UMAP plots for the early *Ciona* embryo.

(A-C) UMAP plots of STAMPs from the (A) 64-cell, (B) 110-cell, and (C) mid-gastrula stages showing the assigned cell identities after mother-of-origin effects have been scaled out. (D-D') (D) Vegetal and (D') Animal views of the 64-cell embryo where the cells have been colored to match the scRNAseq clusters from (A). (E-E') (E) Vegetal and (E') Animal views of the 110-cell embryo where the cells have been colored to match the scRNAseq clusters from (B). (F)

Schematic representation of the neural plate at the mid-gastrula stage. Colors correspond to the colors in (C)

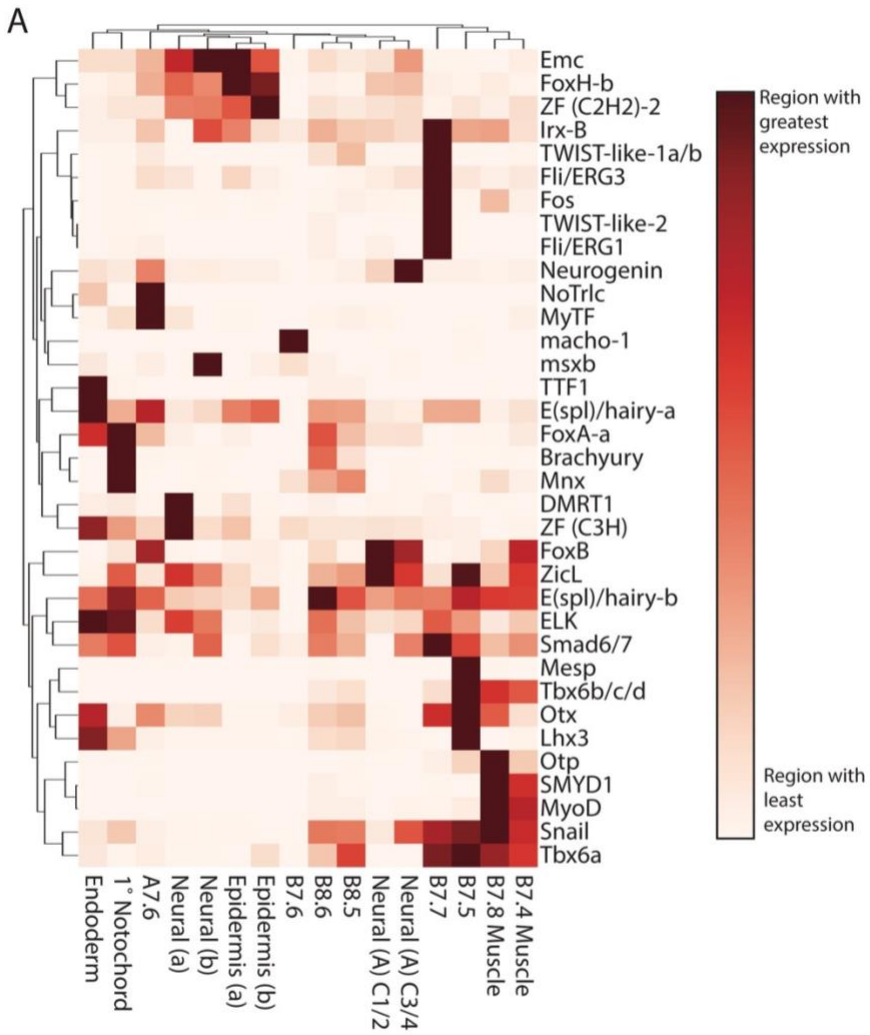

Figure 5.4 scRNAseq adds quantitative context to transcription factor expression profiles at the fate restricted 110-cell stage.

(A) Heatmap showing the average expression value in each scRNAseq cluster for the top 35 most variably expressed TFs at the 110-cell stage. Expression values shown are the average of the count values for all STAMPs in a cluster. These values have been standardized across the embryonic regions to a maximum value of 1 and a minimum value of 0 for each gene.

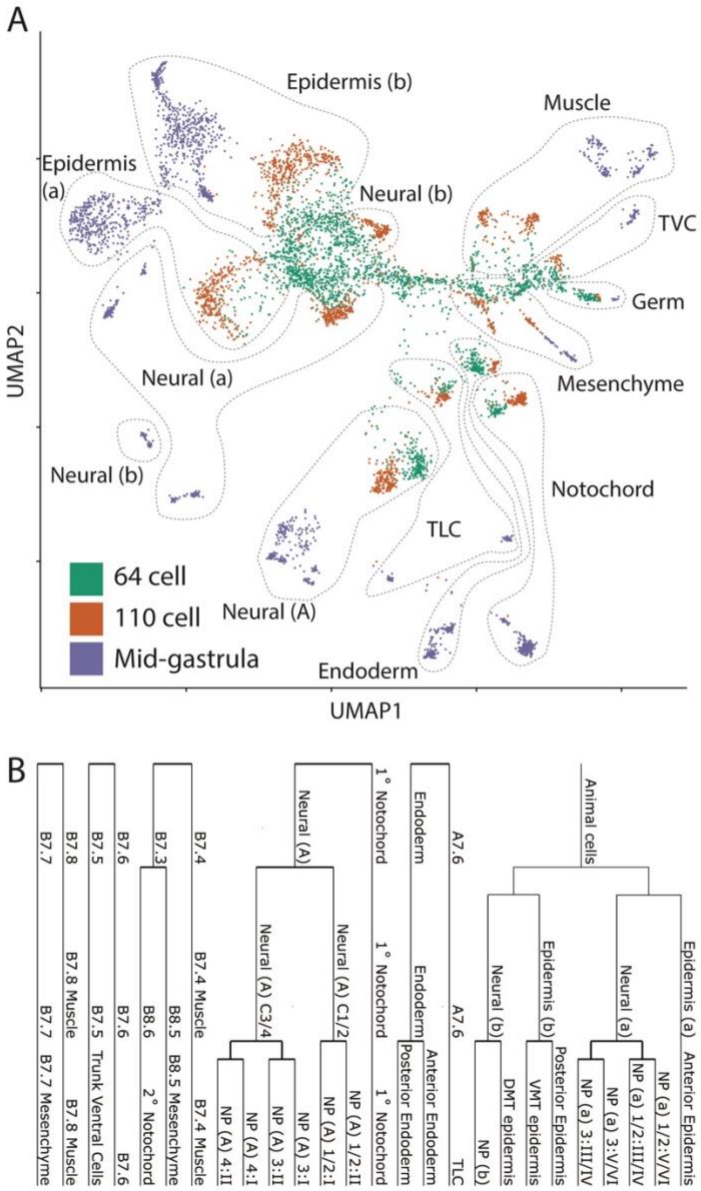

Figure 5.5 scRNAseq captures temporal patterns of gene expression.

(A) UMAP plot of all STAMPs from all stages colored by developmental stage. Outlines delineate broad embryonic territories. (B) Lineage diagram of all detected STAMP clusters at each stage.

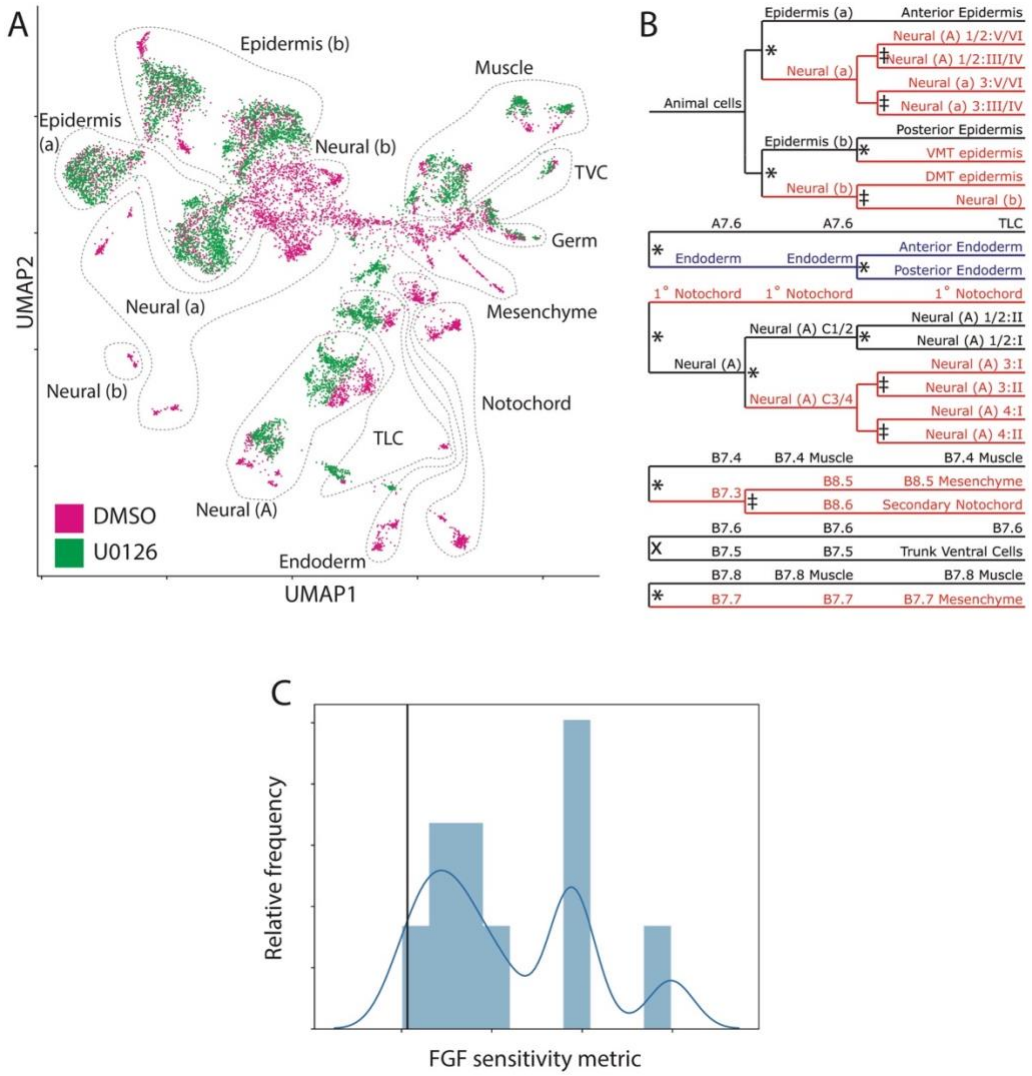

Figure 5.6 MAPK inhibition with U0126 leads to changes in developmental trajectories of some lineages.

(A) UMAP plot of all STAMPs from U0126 and control treated embryos at all stages analyzed colored by treatment. Outlines delineate broad embryonic territories and are identical to those from Figure 5.5 A. (B) Lineage diagram of all detected STAMP clusters at each stage colored by their response to FGF inhibition. Red lineages are lost upon U0126 treatment, blue lineages are transfated to a novel transcriptional state, and black lineages are unaffected. * = p-value < 0.05 by chi-square test, X = p-value > 0.05 by chi-square test, ‡ = not testable because the parent cell type is itself U0126-sensitive. (C) Distribution of FGF sensitivity metric in FGF sensitive lineages. Black line denotes a p-value of 0.05.

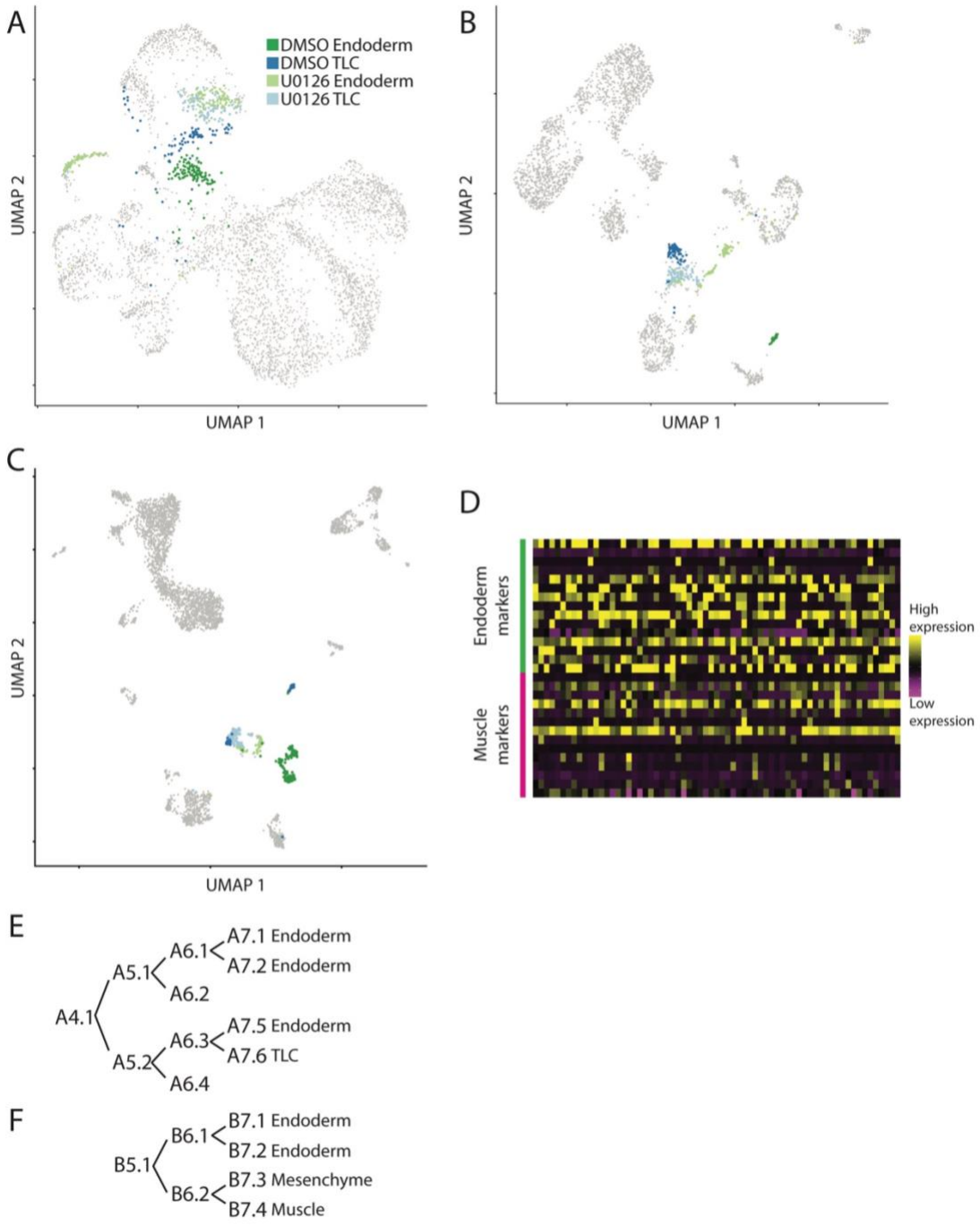

Figure 5.7 The posterior endoderm is not transfated to a sibling lineage upon MAPK inhibition.

(A-C) UMAPs showing Endoderm and TLC cells in DMSO and U0126 conditions at the (A) 64-cell stage, the (B) 110-cell stage, and the (C) mid-gastrula stage. (D) Scaled expression level in putative transfated posterior endoderm STAMPs at 64-cell of the top 15 markers of wildtype endoderm and the top 15 markers of wildtype muscle. (E) Cell lineage of anterior endoderm from 8-cell through 64-cell stage. (F) Cell lineage of posterior endoderm cells from 16-cell through 64-cell stage.

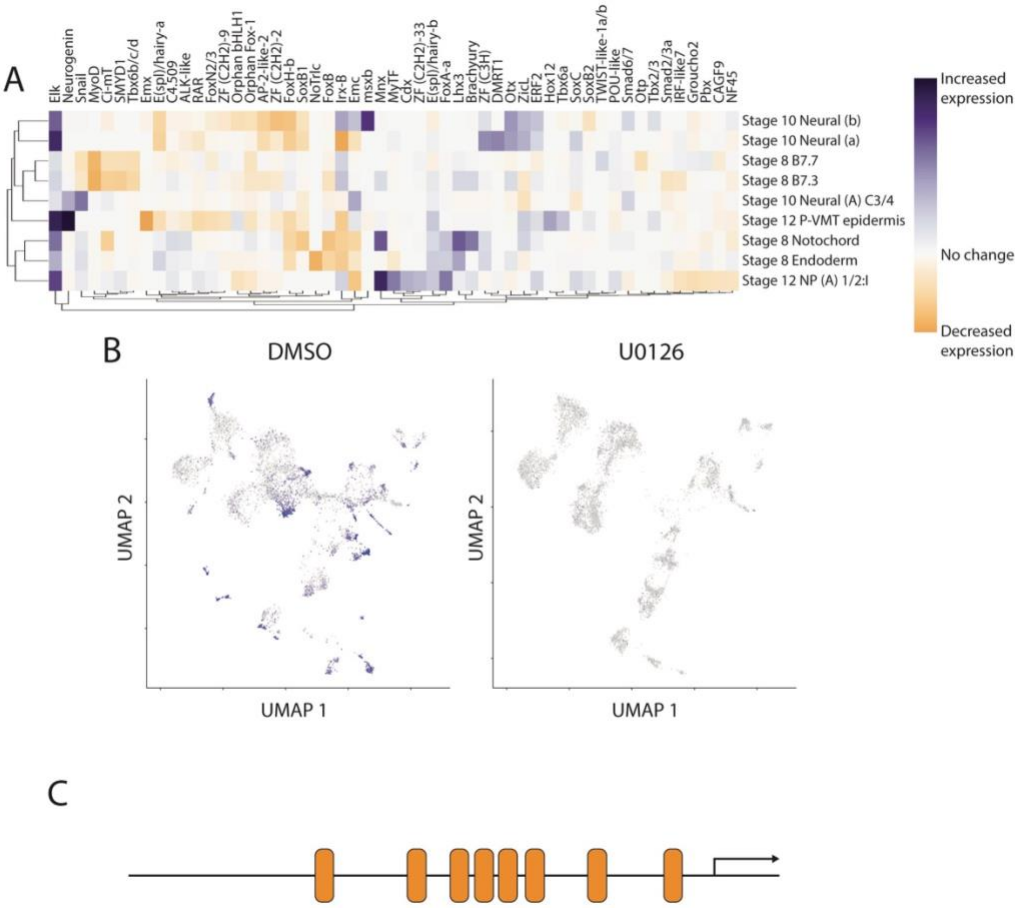

Figure 5.8 Elk1 as a putative autoregulatory TF in an FGF dependent feedback loop.

(A) Log_2 fold-change of the most highly variable TFs between FGF dependent lineages and their FGF independent sibling lineages. (B) Scaled expression level of ELK1 in all STAMPs in control treated versus U0126 treated embryos. The UMAP space is identical to Figure 5.5 A. (C) Elk1 binding sites in the putative Elk1 enhancer as determined by the FIMO webtool are shown as orange rectangles.

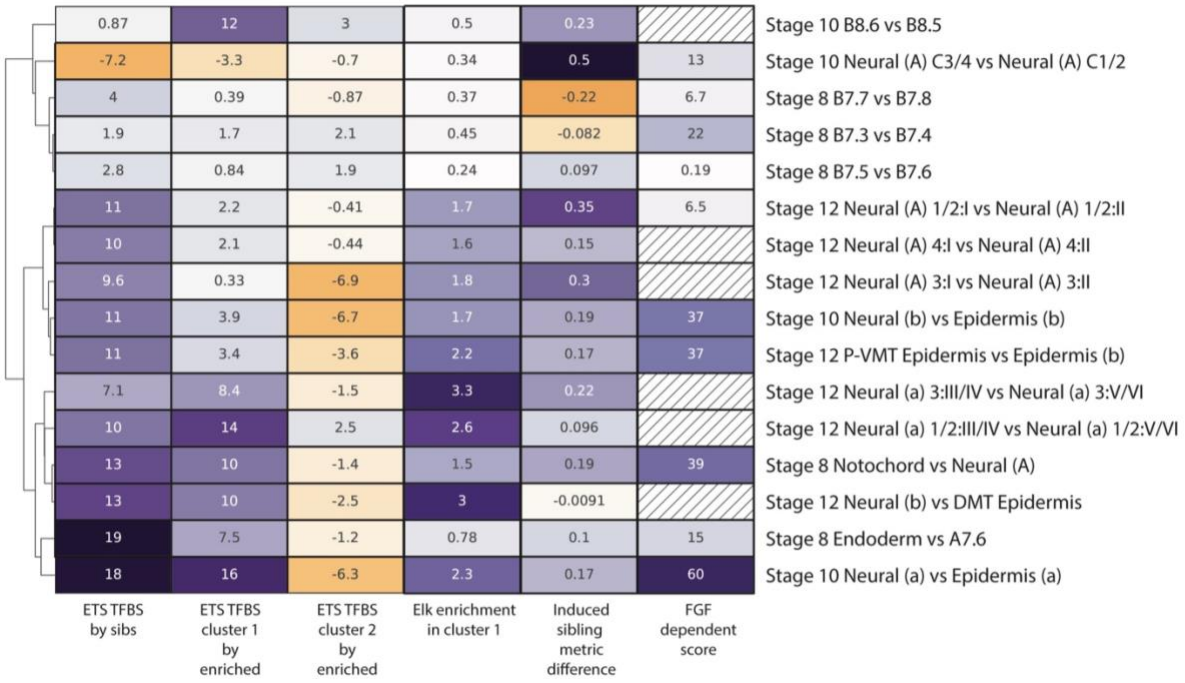

Figure 5.9 TFBS enrichment analysis of cell fate bifurcations reveals distinct FGF response classes.

Heatmap of TFBS enrichment (enrichment z-scores), TF expression level differences (differences in average scaled counts for all STAMPs within a cluster), and various metrics of FGF sensitivity and response for lineage bifurcations analyzed at all three stages. For comparisons of siblings, the scores represent the value in the first sibling listed compared to the second sibling listed. Hatched cells in the FGF dependent score column represent bifurcations where this metric could not be directly calculated

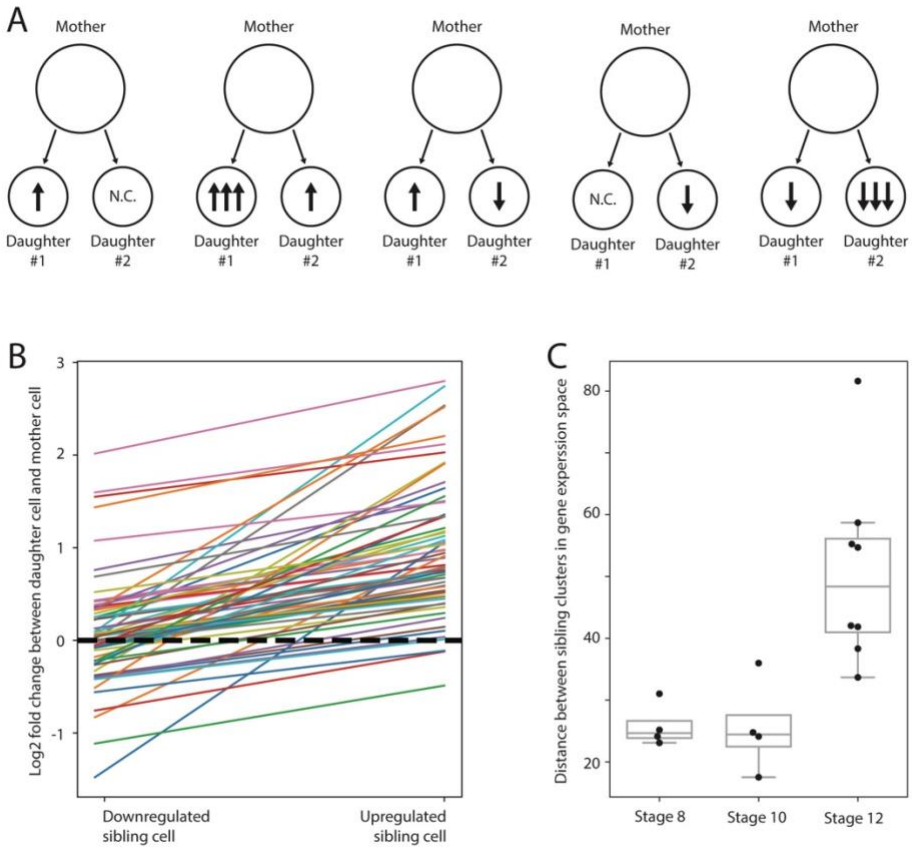

Figure 5.10 Using mother-daughter-sibling "trios" to infer regulatory dynamics of cell fate induction.

(A) The five different scenarios that could result in a gene being more highly expressed in daughter cell number one than daughter cell number two. Arrows represent the change in expression with respect to the level of expression in the mother cell. N.C. = No change. (B) Lines show the difference in expression level between each sibling cluster and the parent cluster in our STAMP cluster "trios". Each line represents a TF that is differentially expressed between two sibling clusters. For all lines, the upregulated sibling cluster value is on the right and the downregulated sibling cluster value is on the left. Slope of the line represents the difference in expression level between the siblings. (C) Euclidian distance between newly born sibling clusters immediately after a bifurcation event in full gene expression space.

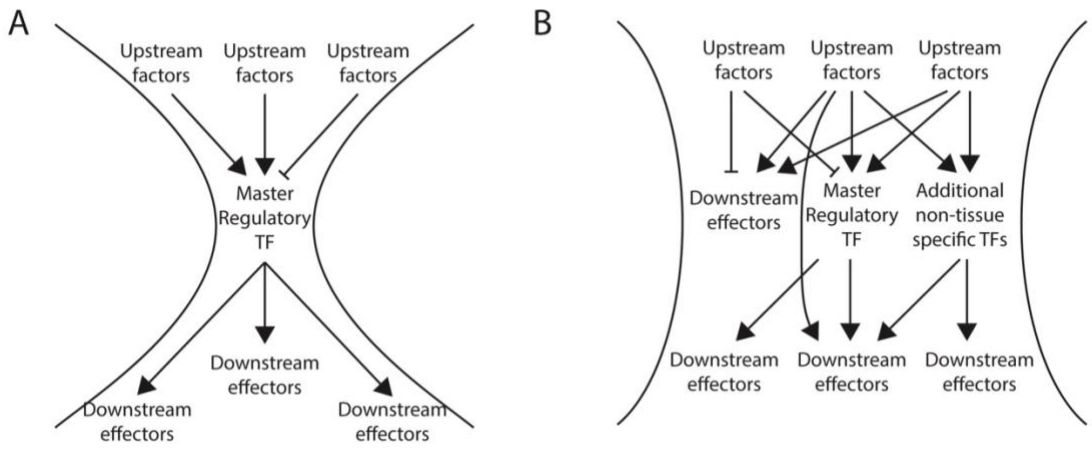

Figure 5.11 The "wide-hourglass" GRN model of cell-fate specification.

(A) Representation of a narrow hourglass model of cell fate induction involving a single master regulator. (B) Representation of a wide-hourglass model of fate induction involving multiple transcription factors and effector genes all induced by the same combination of upstream factors.

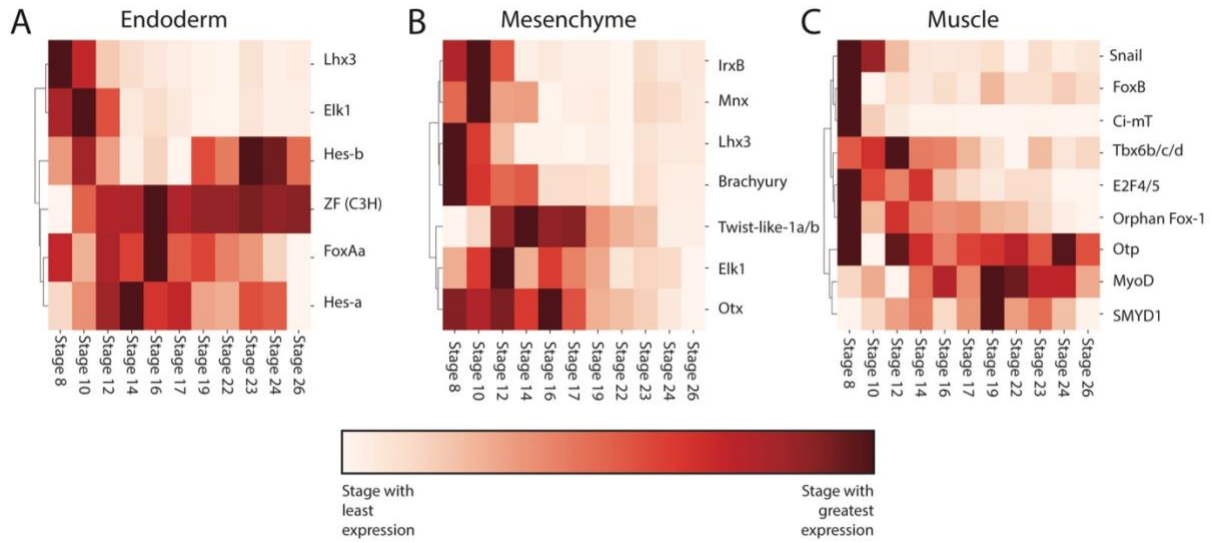

Figure 5.12 The earliest diverging TFs in lineage bifurcations exhibit consistent patterns of transient versus stable induction.

(A-C) Mean scaled read counts for each STAMP cluster standardized across developmental stage to a minimum of zero and a maximum of one. This standardized value is shown over time in the (A) Endoderm, (B) Mesenchyme, and (C) Muscle lineages for the TFs that were identified as being upregulated in these cell types versus their sibling cell types at their initial bifurcation.

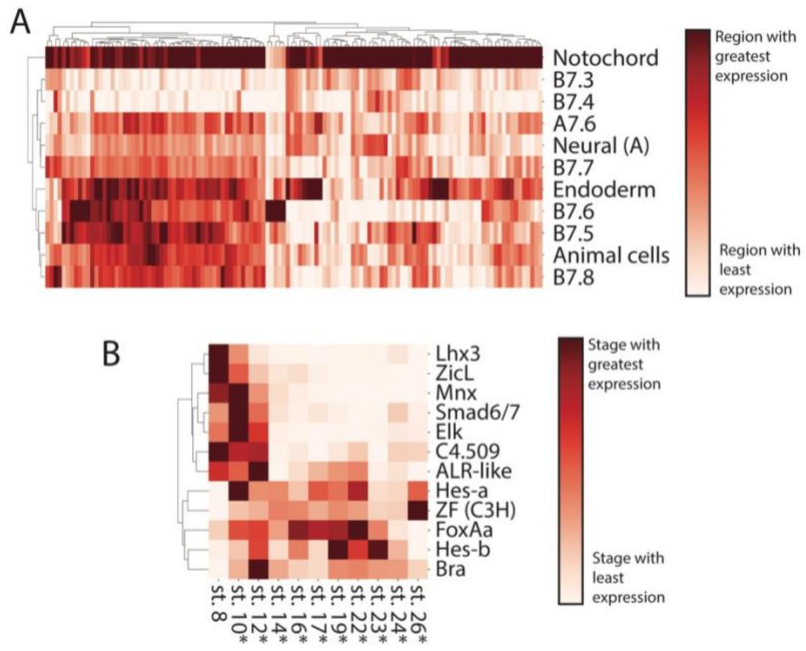

Figure 5.13 Many genes are upregulated in the notochord blastomeres at their earliest stages.

(A) Mean expression within each cluster (scaled read counts standardized across embryonic regions to a minimum of zero and a maximum of one). This average expression value is shown for each gene in each that is differentially expressed in the notochord versus its sibling A-line neural lineage at the 64-cell stage. (B) Mean expression within each cluster (scaled read counts standardized across embryonic regions to a minimum of zero and a maximum of one). This average expression value is shown over time for each TF that is upregulated in the notochord versus its A-line neural sibling lineage at the 64-cell stage.

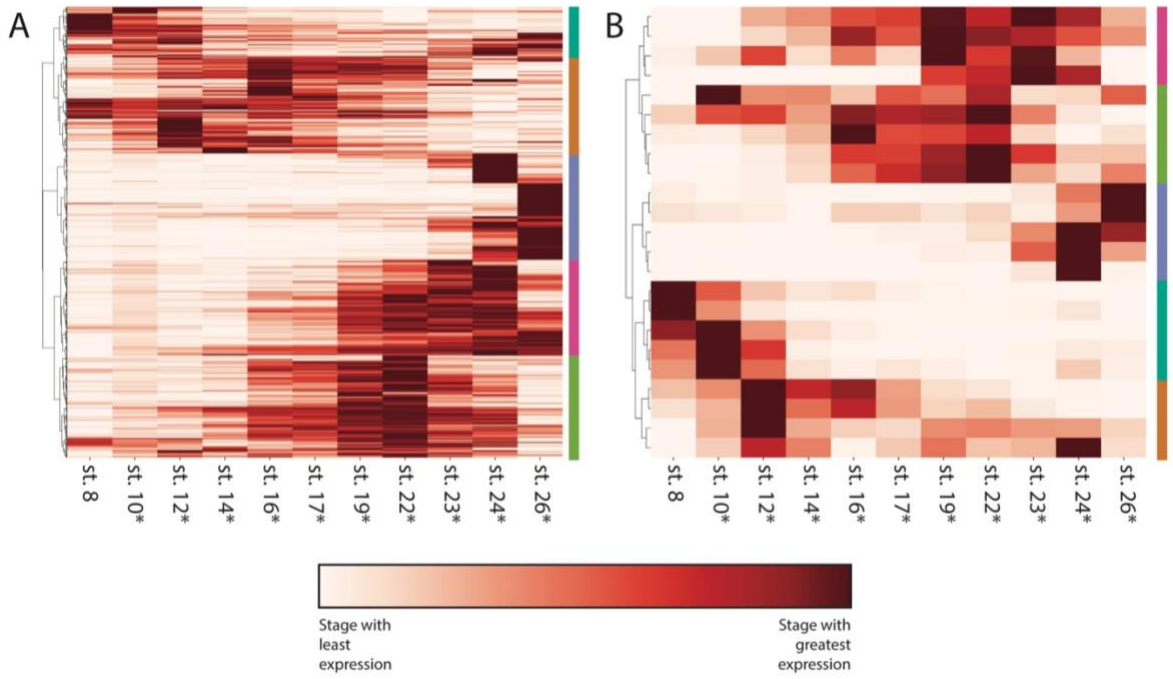

Figure 5.14 The notochord exhibits distinct waves of transcription.

(A) Mean notochord expression over time (scaled read counts standardized across developmental stages to a minimum of zero and a maximum of one). This average expression value is shown over time for each gene that is enriched in the notochord across all stages analyzed. (B) Mean notochord expression over time (scaled read counts standardized across developmental stages to a minimum of zero and a maximum of one). This average expression value is shown over time for each TF that is enriched in the notochord across all stages analyzed. Colored bars in correspond to matching transcription waves.

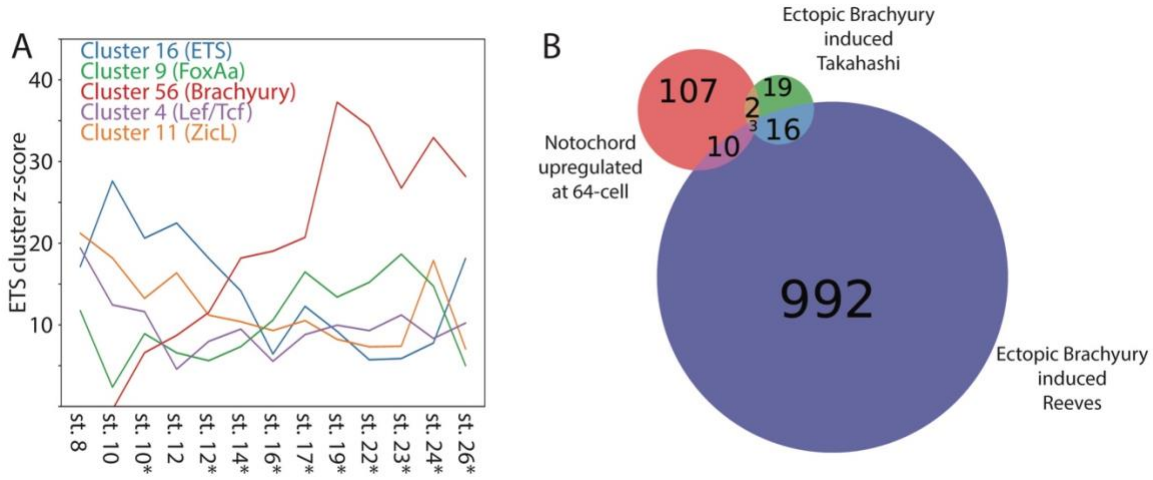

Figure 5.15 Temporal profiles of TFBS enrichment in notochord genes.

(A) TFBS enrichment score for the indicated JASPAR TFBS motif clusters over time. (B) Overlap between genes that are upregulated in the notochord versus their A-line neural sibs at the 64-cell stage, and two different studies that identified genes that were upregulated by ectopic Brachyury expression (W. M. Reeves et al., 2020; Takahashi et al., 1999).

Chapter 6 - Conclusions

Introduction

In this final chapter I will outline the major conclusions from this dissertation which used the notochord of the invertebrate chordate *Ciona* as a model to understand both morphogenetic and transcriptional mechanisms of cellular differentiation. I will present these conclusions in the light of the current understanding of the field and propose open questions that will need to be addressed with future work.

Morphological Differentiation

Understanding the cellular processes that give rise to organ shape has deep importance in fields ranging from fundamental developmental biology through to tissue engineering and regenerative medicine. Understanding the mechanisms of organogenesis is complicated by the complex morphology and large cell numbers of typical vertebrate organs. The notochord of *Ciona* has a simple shape in the form of a tapered rod, and it is comprised of only 40 cells. Many biological structures are shaped in some way like a tapered rod, and very little is known about the cellular processes that give rise to tapering. Previous work demonstrated that both the volume and aspect ratio of *Ciona* notochord cells contribute to the overall tapered shape of the organ (Veeman & Smith, 2013).

The work presented in chapter 4 grew out of the hypothesis that the differences in notochord cell volumes which contribute to the organ's overall tapered shape arise early in development through asymmetric divisions of notochord cells. We tested this hypothesis, as well as an alternative but not necessarily mutually exclusive hypothesis that differences in notochord cell volume could arise through patterned shrinking and swelling of cells after they become post-mitotic. My results in this chapter demonstrate that asymmetric division alone has the power to

shape an entire chordate organ. To the best of our knowledge, this is the first demonstration of such a mechanism. The cumulative power of these relatively subtle asymmetries only became apparent to us after detailed quantitation of every cell in the notochord with a large sample size. This mechanism might very well be important in other systems where the large-scale quantitation of sibling-cell volume asymmetries would be far more challenging.

In chapter 4 we also exploited the experimental tractability of the *Ciona* notochord to perform a fully 3-dimensional analysis of spindle positioning in the context of mother cell shape to infer specific cellular mechanisms of unequal cleavage. Previous studies in this area have typically studied cultured cell monolayers (O'Connell & Wang, 2000) or used two-dimensional analyses of inherently three-dimensional processes in embryos and tissues (Dumollard et al., 2017). Previous work on asymmetric division has focused primarily on a role for spindle displacement, with some attention also given to a potential role for unequal contractility in the mother cell (Ou et al., 2010; Pham et al., 2019). We addressed both of these mechanisms while also in investigating a previously unexplored mechanism involving the shape of the mother cell. We found that all three of these mechanisms are involved in the *Ciona* notochord divisions, with surprisingly complex differences between different notochord founder blastomeres.

There are many questions raised by the work in chapter 4. We identified major differences between different notochord founder blastomeres in terms of the cellular behaviors driving unequal cleavage, but what controls these differences is unknown. One hypothesis would be that the different notochord sub-lineages are experiencing unique signals from the surrounding tissues, which could potentially be addressed by quantifying and experimentally perturbing specific contacts made with the surrounding cell types. Another question is whether other examples of asymmetric division are similar or different in their relative use of spindle

displacement, mother cell shape and post-anaphase mechanisms. An obvious place to test this with comparable single-cell resolution would be in the earlier cleavages of the *Ciona* embryo, which have stereotyped patterns of asymmetry in certain blastomeres (Dumollard et al., 2017). Lastly, we were not able to directly confirm if the post-anaphase mechanisms we observed were due to unequal cortical contractility or some other cellular mechanism. This and other questions about the interplay between these different drivers of asymmetry would be best addressed by live imaging, which would be more feasible in an ascidian such as *Phallusia* with particularly transparent embryos.

Transcriptional differentiation

Inductive signaling events lead to bifurcations of cell fate and transcriptional differentiation of sibling cell types. Embryo-wide mapping of the genome-wide transcriptional changes involved in cell fate bifurcations has only recently become technically feasible. In chapter 5, we took advantage of the small cell numbers and defined cell lineages in the *Ciona* embryo together with droplet microfluidic scRNAseq to quantify cell type-specific genome-wide transcriptional changes in response to FGF/MAPK-dependent inductive cues.

My results in chapter 5 demonstrate that inhibition of FGF signaling in the *Ciona* embryo usually transfates FGF-dependent cell types to their FGF-independent sibling cell type, but there are certain lineages where it results in completely novel patterns of gene expression. That implies that FGF signaling operates either in parallel to, or downstream of, another patterning mechanism in those lineages. Additionally, we identified several FGF dependent lineages that lack enrichment for binding sites of the ETS family transcription factors in their upregulated genes. This could indicate that these lineages either have an ETS mediated FGF transcriptional response of only a small number of possibly key genes, or that they have an FGF response that is

less directly dependent on canonical ETS family TF regulated transcription. Thirdly, we identified a putative autoregulatory feedback role for the *Ciona* ETS family transcription factor Elk1. These three results have important implications for the way that we understand the global transcriptional responses to the FGF signal that patterns the *Ciona* embryo.

In addition to these new insights into the details of *Ciona* cell fate specification, we also made observations with broad relevance to understanding cell fate specification more generally. Cell fate induction events can be thought of as an hourglass where various upstream regulators feed into the expression of one or more key transcriptional regulators of the newly induced cell type that then induce numerous tissue-specific effector genes. Here we find that the "pinch point" at the waist of this hourglass is wider than previously appreciated. We see that these "pinch points" include not just one or a few "master regulatory" transcription factor(s) becoming differentially expressed compared to sibling cell types immediately after cell types diverge, but rather entire suites of transcription factors as well as many putative effector genes. We demonstrate that this trend holds across several lineages. These results together demonstrate that previous representations of tissue-specific GRNs being entirely downstream of just one or a few master regulatory TFs may be overly simplistic.

Embryo-wide scRNAseq experiments generate enormous amounts of data and we have only begun to scratch the surface of what can be learned from this dataset. There are many open questions, two of which I will discuss here. We identified distinct transcriptional waves of expression during *Ciona* notochord development. One obvious question is whether these distinct waves have a direct relationship to distinct phases of notochord morphogenesis such as mediolateral intercalation, notochord elongation and notochord lumen formation. A starting point would be to examine the precise temporal correlation between these suites of effector genes and

the onset of specific cell behaviors, and also to test for relevant enriched Gene Ontology codes. Another obvious topic would be to follow up on the observation that the earliest diverging TFs between sibling cell types tend to fall into two temporal expression patterns. They are either expressed for only a short period of time following cell type differentiation, or their expression level is sustained and continues to increase throughout development. One straightforward hypothesis is that the TFs with a short pulse of expression are required for cell type induction only, while those with sustained expression patterns might be necessary for maintaining tissue-type specific expression of target genes. Alternatively, some TFs might become divergently expressed between sibling cell types without playing any major functional role in that cell fate bifurcation. Testing these hypotheses would require reverse genetic approaches and is beyond the scope of the analyses presented in chapter 5, but would be valuable in developing a robust understanding of how to infer key features of developmental GRNs from scRNAseq datasets.

Final conclusions

Using a model system that is extremely amenable to quantitative analyses of development allowed us to lay a groundwork that changes the way we think about the processes of morphological and transcriptional cellular differentiation. Through the work in this dissertation, we have generally found that quantitative analyses of these processes reveal more elaborate mechanisms of regulation than previously appreciated. Unequal cleavages involve more than just spindle displacement. Cell lineage bifurcations involve large suites of genes that diverge in expression and not just single master regulatory TFs. It is possible that this general trend will continue to hold as other morphological and transcriptional cellular differentiation events are analyzed with today's highly quantitative methods. If this is the case, the reductionist understanding which we have long held about many cellular differentiation events being controlled by a simple Boolean logic network may reflect the dynamic range of our methods more than the integrative and deeply graded nature of these events. Continued analysis with systems-level approaches will be necessary to decipher the inner workings of these complex regulatory mechanisms.

References – Chapter 6

Dumollard, R., Minc, N., Salez, G., Aicha, S. Ben, Bekkouche, F., Hebras, C., Besnardeau, L., & McDougall, A. (2017). The invariant cleavage pattern displayed by ascidian embryos depends on spindle positioning along the cell's longest axis in the apical plane and relies on asynchronous cell divisions. *ELife*, *6*, 1–23. https://doi.org/10.7554/eLife.19290

O'Connell, C. B., & Wang, Y. L. (2000). Mammalian spindle orientation and position respond to changes in cell shape in a dynein-dependent fashion. *Molecular Biology of the Cell*, *11*(5), 1765–1774. https://doi.org/10.1091/mbc.11.5.1765

Ou, G., Stuurman, N., D'Ambrosio, M., & Vale, R. D. (2010). Polarized myosin produces unequal-size daughters during asymmetric cell division. *Science (New York, N.Y.)*, *330*(6004), 677–680. https://doi.org/10.1126/science.1196112

Pham, T. T., Monnard, A., Helenius, J., Lund, E., Lee, N., Müller, D. J., & Cabernard, C. (2019). Spatiotemporally Controlled Myosin Relocalization and Internal Pressure Generate Sibling Cell Size Asymmetry. *IScience*, *13*, 9–19. https://doi.org/10.1016/j.isci.2019.02.002

Veeman, M. T., & Smith, W. C. (2013). Whole-organ cell shape analysis reveals the developmental basis of ascidian notochord taper. *Developmental Biology*, *373*(2), 281–289. https://doi.org/10.1016/j.ydbio.2012.11.009

Appendix A - Supplemental Information for Chapter 4

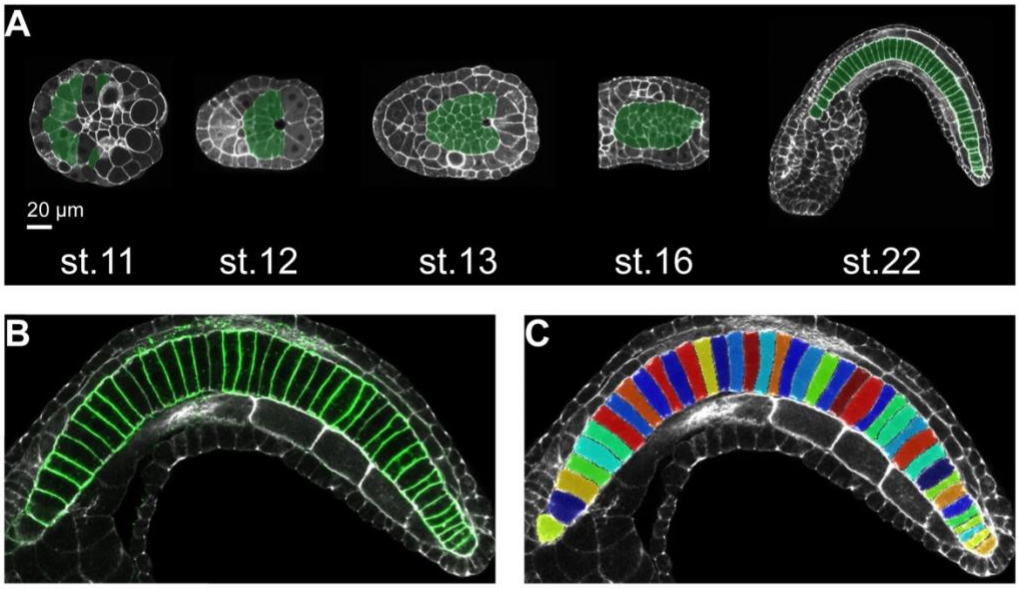

Figure A.1 Notochord development and segmentation details, Related to Figure 4.1.

A) Selected z-slices of confocal stacks for embryos at stages listed in Figure 1A. Notochord cells have been pseudocolored in green by hand. B-C) Selected z-slice through a notochord where all 40 cells are expressing a membrane-GFP transgene, along with pseudocolored overlaid segmentation.

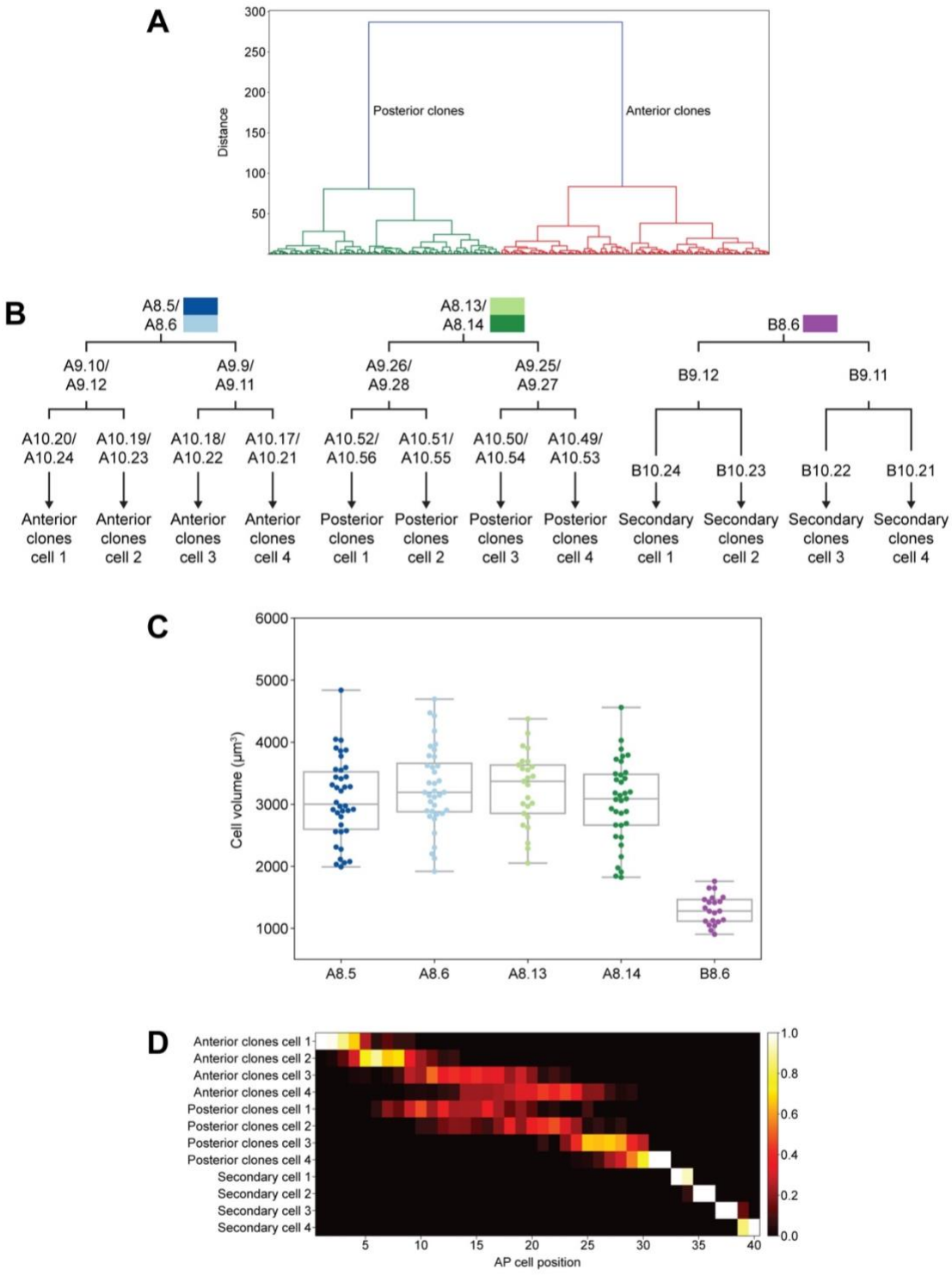

Figure A.2 Sibling cell volume ratios are stable over time, Related to Figure 4.3.

A) Hierarchical clustering of primary 4-cell clones by their intercalation positions. Distance metric is Ward's Variance Minimization. Clusters corresponding to anterior and posterior clones are marked. B) Lineage tree of primary anterior clones (Left), primary posterior clones (Middle) and secondary notochord (Right). C) Volumes of the notochord founder cells from the analysis

of spindle position in the second-last division. D) Heatmap showing the probability that a given AP cell position after intercalation is occupied by the different blastomeres indicated. This used the genetic fate mapping data from Carlson et al (2015) extended here to a larger sample size (more details in STAR methods).

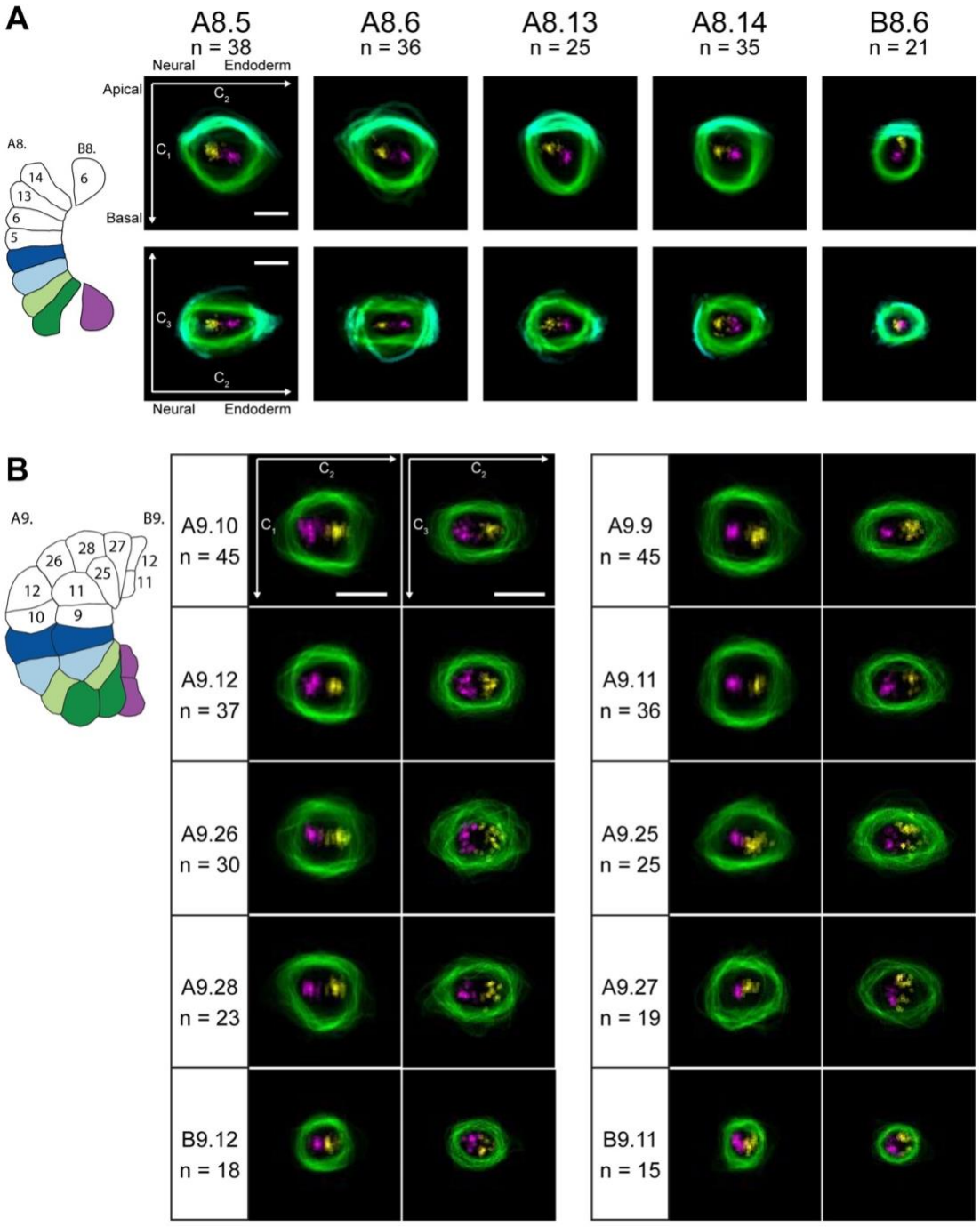

Figure A.3 Overlaid eigen-cell projections, Related to Figure 4.4.

A) All cells of a given lineage that were part of our overall analysis for the second-last division were rotated so that their C1, C2, and C3 vectors aligned, and were translated so that their cell centroids overlapped. The resulting 3-dimensional overlaid volumes were then projected using a summed intensity projection onto the C1 and C2 plane (top) or the C2 and C3 plane (bottom). Summed intensity projections captured all the spindle poles. Cell membrane is in green, apical surface is in cyan, anterior spindle pole is in magenta, and posterior spindle pole is in yellow. B) All cells for each lineage in the final division were rotated so that their C1, C2, and C3 vectors

aligned, and were translated so that their cell centroids overlapped. Summed intensity projections through the spindle poles in the C1 and C2 plane (left) or the C2 and C3 plane (right) were performed for each overlaid eigen-cell. Cell membrane is in green, anterior spindle pole is in magenta, and posterior spindle pole is in yellow.

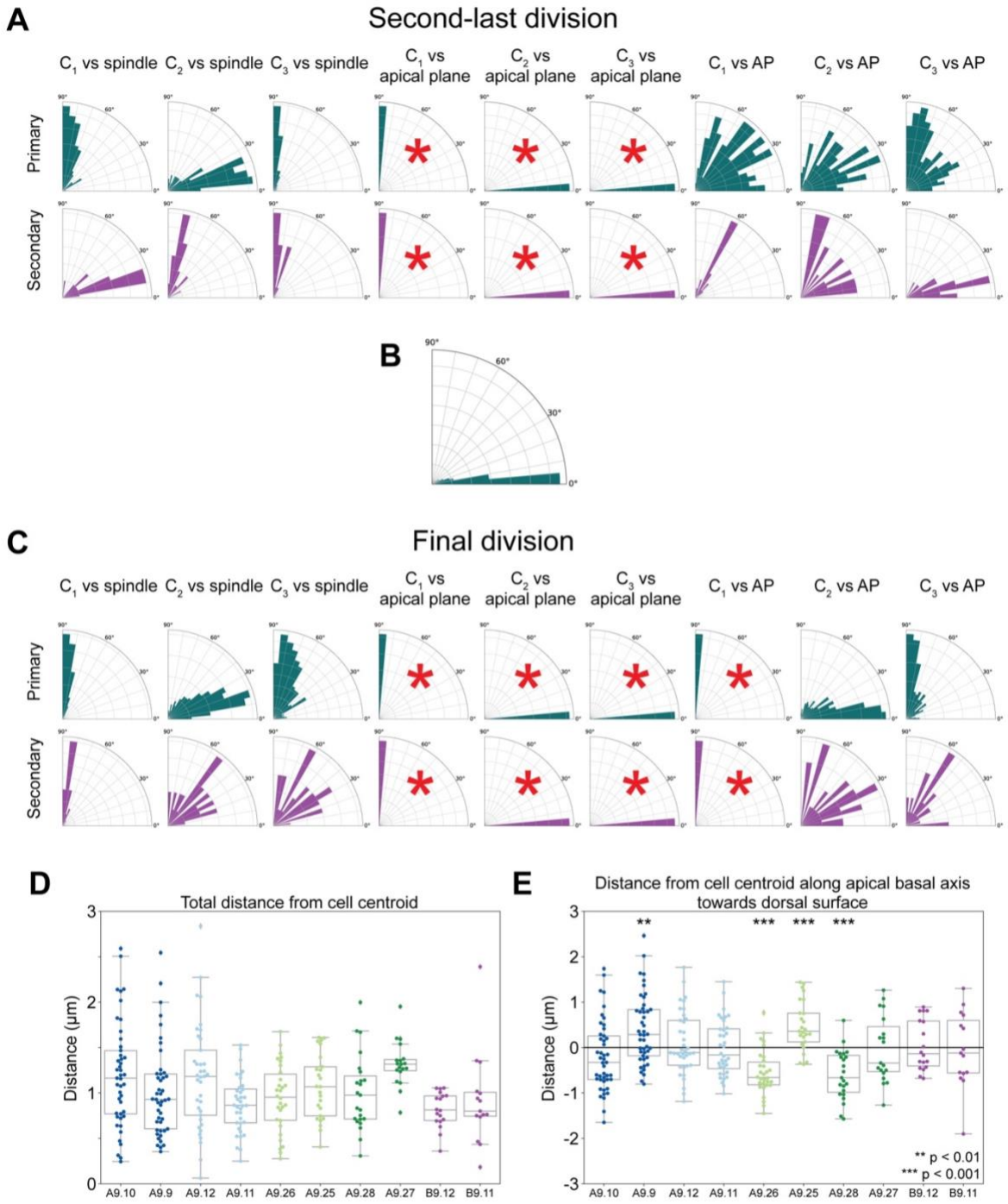

Figure A.4 Additional measurements of spindle orientation and displacement, Related to Figure 4.4.

A) Degrees of deviation from the listed reference for the primary and secondary cells in the second-last division. Red asterisks denote measurements that are either parallel or orthogonal by definition. B) Angle of deviation between the C2 vector and the longest axis of the apical surface for the primary cells in the second-last division. C) Degrees of deviation from the listed reference for the primary and secondary cells in the final division. Red asterisks denote measurements that are either parallel or orthogonal by definition. D) Total distance between the cell centroid and the

spindle midpoint in the final division. E) Apical-basal displacement of the spindle midpoint from cell centroid towards the dorsal surface of the cell in the second-last division. Asterisks designate statistically significantly displacements from 0 μm.

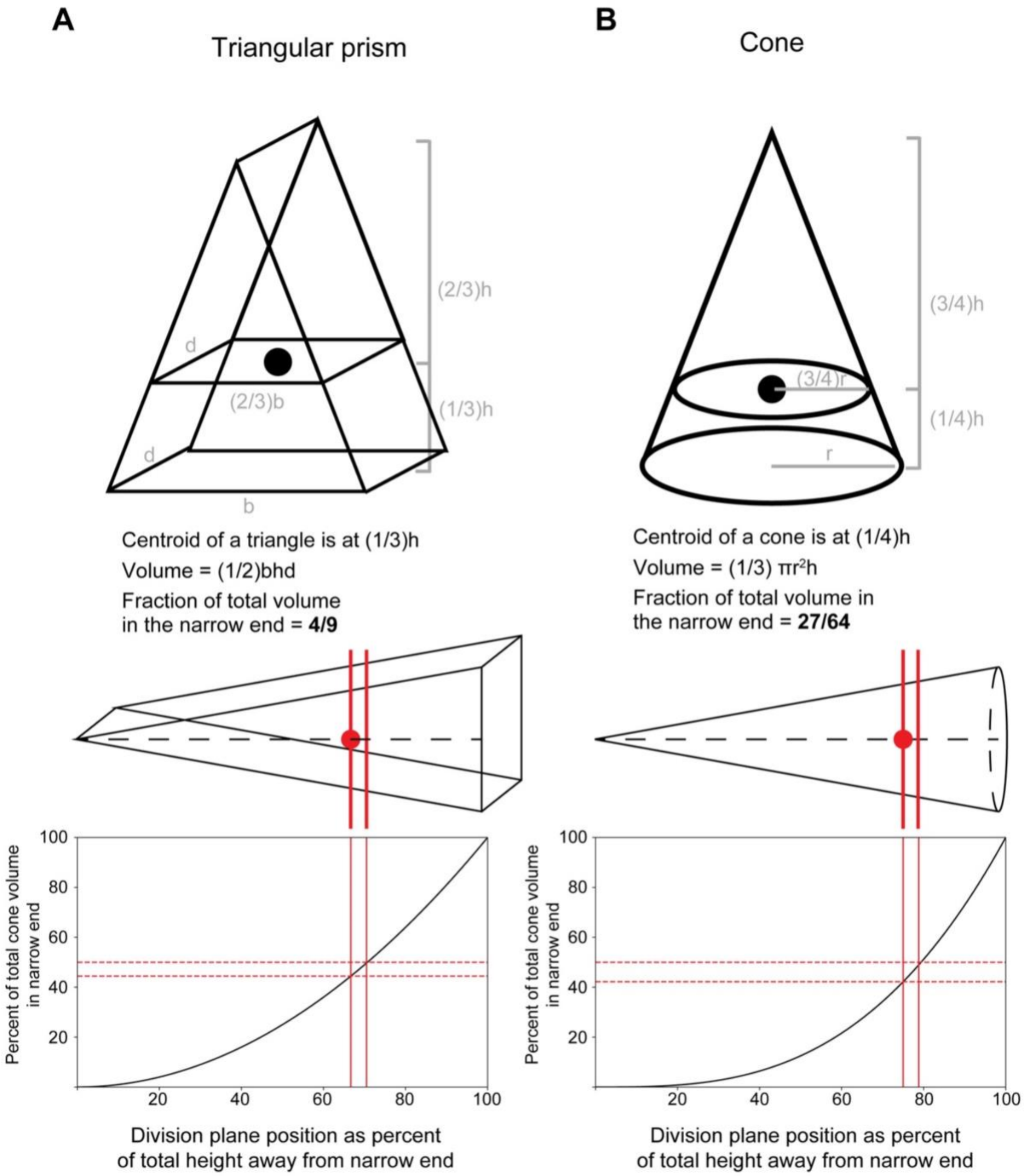

Figure A.5 Hypothetical role of mother cell shape in unequal cleavage, Related to Figure 4.5.

A) Cartoon diagram of a hypothetical cell shaped like a triangular prism. The cell centroid is marked, together with the cleavage plane that would be expected given the long axis shown. Note that a spindle centered at the centroid would not give daughters of equal volume, and that the 4:5 daughter cell volume ratio predicted is independent of aspect ratio as long as spindle orientation does not change. The chart at the bottom explores the effect of displacing the spindle

along the wedge-shaped axis and shows how the centroid and point of equal cleavage are not the same. B) shows the same analysis but for a cone- shaped cell.